JOURNAL OF PETROLOGY | VOLUME 51 | NUMBERS 1 & 2 | PAGES 255–294 | 2010 | doi:10.1093/petrology/egp087

Plagioclase Peridotites in Ocean–Continent Transitions: Refertilized Mantle Domains Generated by Melt Stagnation in the Shallow Mantle Lithosphere

OTHMAR MÜNTENER[1]*, GIANRETO MANATSCHAL[2], LAURENT DESMURS[3] AND THOMAS PETTKE[4]

[1]INSTITUTE OF MINERALOGY AND GEOCHEMISTRY, UNIVERSITY OF LAUSANNE, ANTHROPOLE, CH-1015 LAUSANNE, SWITZERLAND

[2]IPGP-EOST, UNIVERSITY OF STRASSBOURG, 1 RUE BLESSIG, 67084 STRASBOURG, FRANCE

[3]INSTITUTE OF GEOLOGY, ETH ZURICH, SWITZERLAND

[4]INSTITUTE OF GEOLOGICAL SCIENCES, UNIVERSITY OF BERN, BALTZERSTR. 1-3, 3012 BERN, SWITZERLAND

RECEIVED MARCH 31, 2009; ACCEPTED NOVEMBER 20, 2009
ADVANCE ACCESS PUBLICATION DECEMBER 30, 2009

The existence of different mantle domains exposed in ocean–continent transition zones provides a framework for understanding the generation of ultramafic seafloor along magma-poor rifted margins. In this study we present detailed petrological and geochemical data on peridotites from the Eastern Central Alps ophiolites in Switzerland and Italy to identify different mantle domains, to estimate the extent of refertilization, and to test whether refertilization is associated with a thermal signature that has important implications for geophysical interpretations of ocean–continent transitions. The compositions of clinopyroxene, orthopyroxene and spinel clearly reflect the different mantle domains. Relative to clinopyroxenes from spinel peridotites, clinopyroxenes from plagioclase peridotites have lower Na_2O and Sr contents, but higher middle to heavy rare earth element ratios and Zr concentrations, and different Sc–V relationships. Spinels in plagioclase peridotites have higher TiO_2 and lower Mg-numbers compared with those in spinel peridotites. Mineral–mineral trace element partitioning suggests that spinel peridotites equilibrated at substantially lower temperatures than plagioclase peridotites. The temperature difference between the spinel and plagioclase peridotites indicates an important thermal boundary between the two. The geochemical data show systematic spatial variations. A heterogeneous, 'subcontinental domain' with no syn-rift melt imprint is separated from a 'refertilized domain' that exhibits a complex history of regional-scale melt infiltration and melt–rock reaction, which has erased most of the ancient history. Simple calculations suggest that up to 12% of mid-ocean ridge basalt-type melt can be stored in plagioclase peridotite, relative to a depleted residue. Such a 'lithospheric sponge' provides an explanation for the fertile compositions of the peridotites and the rare occurrence of volcanic rocks in magma-poor rifted margins. We suggest that magma-poor vs magma-rich margins are largely determined by the efficiency of melt extraction and not so much by melt generation processes, given a similar initial composition of the upwelling mantle. It is proposed that refertilization increases textural diversity and chemical heterogeneity related to shallow crystallization in the mantle lithosphere.

KEY WORDS: *oceanic lithosphere; ophiolite; melt–rock reaction; refertilization; plagioclase peridotite; magma-poor margins; ocean–continent transition*

INTRODUCTION

Classic models for the generation of oceanic lithosphere call for a (spreading-rate dependent) 4–6 km thick igneous crust overlying a peridotite basement; the igneous crust is

*Corresponding author. E-mail: othmar.muntener@unil.ch

produced by decompression melting of ascending asthenospheric mantle. However, in recent years it has been shown that magma supply is limited along slow- and ultraslow-spreading ridges (Dick *et al.*, 1984; Cannat, 1993, 1996; Michael *et al.*, 2003), and that exposure of 'crust-free' mantle lithosphere is more common than previously recognized (Cannat, 1996; Cannat *et al.*, 1997; Bonatti *et al.*, 2001; Michael *et al.*, 2003). Along mid-ocean ridges, peridotite seafloor forms via denudation of the mantle in different environments such as fracture zones, magma-starved ridge segments, and oceanic core complexes (Blackman *et al.*, 1998; Tucholke *et al.*, 1998; Ildefonse *et al.*, 2007). Dick *et al.* (2003) estimated that nearly half of the global mid-ocean ridge system is made of serpentinized peridotite.

In contrast, the exposure of peridotite along 'continental edges' (Coleman, 1971; Coleman & Irwin, 1974) has been known for a long time and has become an integral part of studies that investigate oceanic lithosphere in ancient and present-day continental margins (Decandia & Elter, 1972; Boillot *et al.*, 1987; Piccardo *et al.*, 1990). Numerous geophysical surveys, combined with deep-sea drilling on the present-day Iberia margin (Boillot *et al.*, 1987; for a review, see Tucholke & Sibuet, 2007; Péron-Pinvidic & Manatschal, 2009), and field investigations on well-preserved fragments of the ancient Alpine Tethyan margins and ophiolites exposed in the Alps have allowed a detailed description of the architecture of the ocean–continent transition (OCT) in magma-poor rifted margins (Manatschal & Müntener, 2009). These studies have demonstrated the importance of mantle exhumation, punctuated magmatism and faulting in the OCT (Boillot *et al.*, 1987; Rampone & Piccardo, 2000; Manatschal *et al.*, 2001; Müntener & Hermann, 2001; Whitmarsh *et al.*, 2001; Desmurs *et al.*, 2002). These characteristics of the OCT are in some ways similar to those of ultraslow-spreading ridges (Ildefonse *et al.*, 2007), which are characterized by irregular and highly punctuated magmatism, widely spaced volcanic centers, isolated plutonic bodies emplaced within peridotite and melt stagnation at depth (Michael *et al.*, 2003; Müntener *et al.*, 2004). It follows that the thermal structure of the underlying lithosphere in both OCTs and ultraslow-spreading environments might be variably 'hot' or 'cold'. Conductive cooling of the lithosphere from above causes overall low extents of melting, cessation of decompression melting at greater depth and crystallization of magma at higher pressures.

A fundamental question is whether mantle peridotites and/or mafic rocks exhumed in OCTs and ultraslow-spreading ridges, in both ancient and modern ocean basins, can provide some systematic spatial information that could shed light on the enigmatic transition between the initiation of rifting and the formation of an ocean–continent transition. Michael *et al.* (2003) and Goldstein *et al.* (2008) have described the compositional variation of peridotites and mafic rocks along the axis of an ultraslow-spreading system. They explained the variations in terms of heterogeneity in the different mantle reservoirs and/or highly variable degrees of melting. In this study, we present results from an ancient ocean–continent transition zone, exposed in the Eastern Central Alps (SE Switzerland, Northern Italy), which is more or less perpendicular to the inferred (paleo-) spreading direction. We show that some peridotites close to the continental margin are predominantly subcontinental in origin, with little (magmatic) imprint of the opening process. These are juxtaposed along mylonite zones against peridotites that contain abundant evidence of melt stagnation and melt–rock reaction. We use the expression 'lithospheric sponge' to refer to the site at which porous melt flow ceases and melt stagnation occurs in the mantle, and where the mantle rocks are affected by melt–rock interaction and refertilization, thereby erasing much of the ancient history. Magma storage in the mantle during rifting is probably a major process at magma-poor (so-called non-volcanic) rifted margins. We evaluate the spatial chemical variations within these peridotites and examine their thermal history. We propose that the transition from subcontinental to suboceanic mantle is a 'melt impregnation front', a thermochemical boundary that plays a fundamental role in the evolution of the nascent oceanic crust, from both a thermal and rheological point of view.

THE OPHIOLITES EXPOSED IN SOUTHEASTERN SWITZERLAND AND NORTHERN ITALY

Ophiolites clarify important aspects of our understanding of how ocean–continent transitions and oceanic crust have formed. Numerous studies since the early 1970s have demonstrated that ophiolites in the Alps have little in common with the classic definition of the Penrose Conference in 1972 (for a historical perspective, see Bernoulli *et al.*, 2003; Bernoulli & Jenkyns, 2009). The existence of pre-rift intrusive contacts between subcontinental mantle and lower continental crust (Trommsdorff *et al.*, 1993; Müntener & Hermann, 1996; Desmurs *et al.*, 2001), the occurrence of continent-derived blocks (extensional allochthons) and tectono-sedimentary breccias overlying tectonically exhumed subcontinental mantle rocks (Müntener & Hermann, 1996; Manatschal & Nievergelt, 1997) indicate that some of the Alpine Tethys ophiolites may be interpreted as fragments of a former OCT. The type sequence through an OCT as described by Manatschal & Müntener (2009) can be observed in the Platta–Malenco, Tasna and Chenaillet ophiolite units (Fig. 1), the first two representing the OCT of the ancient Adriatic and European–Briançonnais conjugate rifted

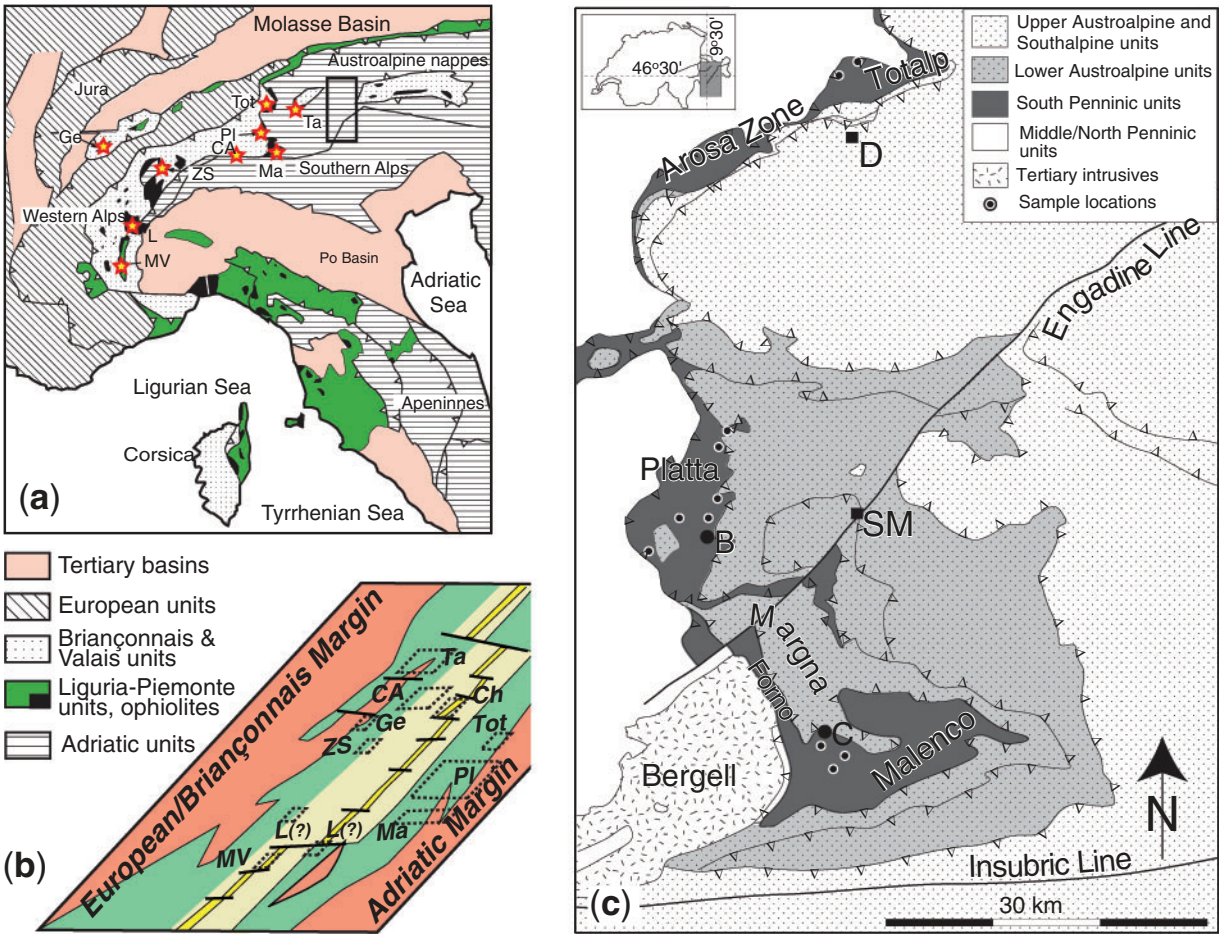

Fig. 1. (a) Overview of the distribution of ophiolites in the Western Alps, Apennines and Corsica. Stars indicate locations of ophiolites. (b) Schematic paleogeogeographical reconstruction of the Piemonte Ligurian ocean in the late Jurassic and distribution of ultramafic bodies, after Manatschal & Müntener (2009). It should be noted that many ophiolites represent sequences of the ocean–continent transition (e.g. Malenco, Platta, Totalp, Gets) and only a few bodies may represent analogues to ultraslow-spreading crust (e.g. Monviso, Chenaillet). CA, Central Alps; Ch, Chenaillet; Ge, Gets; L, Lanzo; Ma, Malenco; MV, Monviso; Pl, Platta; Ta, Tasna; Tot, Totalp; ZS, Zermatt–Saas. (c) Sample locations within the Totalp, Platta and Malenco ultramafic rocks in the Eastern Central Alps, modified from Schaltegger *et al.* (2002). D, Davos; B, Bivio; SM, St. Moritz; C, Chiareggio.

margins, the latter representing a more developed 'oceanic' domain, which may have many similarities to that observed at oceanic core complexes (Tucholke *et al.*, 1998; Ildefonse *et al.*, 2007). Geological maps and cross-sections illustrating the geology and the overall architecture of the ocean–continent transition in this part of the Alps have been presented previously (Florineth & Froitzheim, 1994; Manatschal & Nievergelt, 1997; Desmurs *et al.*, 2001; Müntener & Hermann, 2001; Manatschal *et al.*, 2007). The reconstructions showed that in the upper Platta, Totalp and Malenco units, peridotites were exhumed close to the continental margin, whereas the lower Platta unit was situated in a more distal position (e.g. Manatschal & Müntener, 2009). Here we focus on the petrology of samples from the Totalp, Platta and Malenco serpentinized peridotites (Fig. 1).

Field relations of the serpentinized peridotite basement

The mantle rocks are predominantly serpentinized peridotite and minor pyroxenites and dunites. Locally, the mantle rocks are intruded and/or covered by small to moderate volumes of basaltic rocks, whereas oceanic gabbros have been found only in the lower Platta unit. Serpentinized peridotites are commonly capped by ophicalcites, which represent tectono-sedimentary breccias related to mantle exhumation, or alternatively, replacement of serpentine by carbonates (Lemoine *et al.*, 1987; Desmurs *et al.*, 2001). The serpentinized mantle rocks are in places stratigraphically overlain by late Middle to early Late Jurassic radiolarian cherts, indicating that they must have been exhumed from mantle depths to the seafloor during Jurassic rifting. On the other hand, field evidence

shows that the mantle rocks in Val Malenco represent a fragment of subcontinental mantle, welded to the lower crust by a Permian tholeiitic gabbro (Müntener & Hermann, 1996; Hermann *et al.*, 1997). Radiometric age determinations (zircon U–Pb) showed that crystallization of the gabbro and partial melting of the lower crust were coeval and of Permian age (Hansmann *et al.*, 2001) demonstrating that some of the mantle exposed on the seafloor in Late Jurassic times has a subcontinental origin. Another piece of direct evidence for 'subcontinental' mantle is spectacularly exposed in the Tasna nappe, where serpentinized mantle rocks underlie a wedge of continental crust and are sealed by Lower Cretaceous sediments (Florineth & Froitzheim, 1994; Manatschal *et al.*, 2007). In this example, mantle rocks are by definition subcontinental because of their position beneath continental crust within a pre-Alpine OCT.

Plutonic rocks

Gabbroic rocks form small intrusive bodies and dikes in the peridotites. In the Platta nappe, gabbro bodies intruding serpentinized mantle occupy less than 5–10% of the total observed serpentinite volume. Smaller bodies, less than 100 m in diameter, differ from larger sill-like bodies in terms of their magmatic evolution (Desmurs *et al.*, 2002). The smaller bodies are of homogeneous gabbro whereas the larger bodies show a great diversity in composition from primitive olivine-gabbros to highly differentiated Fe–Ti oxide gabbros and plagiogranite (Desmurs *et al.*, 2002). Mg-numbers and Ni contents of equilibrium olivine calculated from primitive basalts and gabbros indicate that few of the mafic rocks are primary melts; most represent fractionated compositions ranging from transitional (T-) to normal mid-ocean ridge basalt (N-MORB). Most mafic rocks may be explained by low to moderate degrees of melting of a N-MORB source mantle, as indicated by initial Hf isotope compositions of zircons and Nd isotope compositions of basalts (Schaltegger *et al.*, 2002). Zircon U–Pb ages of Fe–Ti gabbros and plagiogranites exhibit a surprisingly narrow range of crystallization ages of 161 ± 1 Ma (Schaltegger *et al.*, 2002).

Extrusive rocks

Basaltic rocks occur as pillows, massive flows or pillow breccias, and as discrete dikes intruding deformed gabbros and mantle peridotites (Dietrich, 1970). Geochemical studies indicate an overall tholeiitic composition and MORB affinity, ranging from T-MORB to N-MORB (Frisch *et al.*, 1994; Ulrich & Borsien, 1996; Puschnig, 2000; Desmurs *et al.*, 2002). The most primitive basalts show either moderate light rare LREE fractionation ($Ce_N/Sm_N = 0{\cdot}6$) or almost flat to slightly LREE-enriched REE spectra, and heavy REE (HREE) abundances at about 10 times Cl-chondrite. They have fairly homogeneous Nd isotopic compositions, consistent with their MORB affinity, but variable Sr isotopic ratios (up to 0·7085), which are related to seawater alteration (Schaltegger *et al.*, 2002). Lead isotopes are also consistent with a MORB affinity (Peretti & Köppel, 1986). Geochemical modeling indicates that the most primitive T- and N-MORB-type basalts are consistent with melts generated by low to moderate degrees of near-fractional melting of a MORB-type asthenospheric mantle source (Desmurs *et al.*, 2002). Cretaceous basalts cutting serpentinites and Late Jurassic sediments have been described by Peters & Dietrich (2008).

SAMPLES STUDIED

All the peridotites examined in this study are partially serpentinized spinel or plagioclase lherzolites. Below we focus on the mantle textures and mineralogy.

The majority of the first group of peridotites (e.g. Totalp, Malenco, upper Platta unit, Fig. 1) are porphyroclastic, fertile to depleted spinel lherzolites with a well-developed high-temperature foliation (Fig. 2a). Most of the Malenco, Totalp and upper Platta peridotites are composed of amphibole-bearing spinel peridotite with locally abundant (garnet) pyroxenite layers (Fig. 3a), dunites and rare phlogopite-hornblendite veins (Peters, 1963, 1968; Müntener & Hermann, 1996; Desmurs, 2001). The modal variability of clinopyroxene is large, especially for the spinel peridotites, ranging from 5 to 15% (Table 1). The samples are variably serpentinized with estimated degrees of serpentinization between ~5% to >80%. However, in all samples selected for this study the primary textural features are largely preserved. The samples generally show porphyroclastic textures; however, peridotite mylonites with extremely stretched orthopyroxene porphyroclasts with aspect ratios exceeding 10:1 are also observed locally (Peters, 1963; Müntener & Hermann, 1996; Desmurs, 2001). Pyroxene porphyroclasts show exsolution lamellae of the complementary pyroxene, whereas small, recrystallized grains are usually devoid of such exsolutions. The latter are in equilibrium with titanian-pargasite, a common observation for many spinel peridotites (Vannucci *et al.*, 1995; Müntener, 1997). Metamorphic plagioclase recrystallization is restricted to garnet-pyroxenite layers. There, pyroxene–spinel symplectites, successively replaced by plagioclase–spinel–pyroxene symplectites form subsolidus intergrowths at the expense of garnet and olivine (Fig. 3). Similar garnet pyroxenites have been described from the northern Apennines (Montanini *et al.*, 2006).

The second group of peridotites (e.g. lower Platta unit) consists mainly of spinel–plagioclase lherzolites, and subordinate harzburgite or dunite; pyroxenite layers are rare. The serpentinized lherzolites of the lower Platta unit have a porphyroclastic texture consisting of large porphyroclastic Cr-diopside, orthopyroxene, Cr–Al spinel and olivine, the last always replaced by serpentine minerals (Fig. 2).

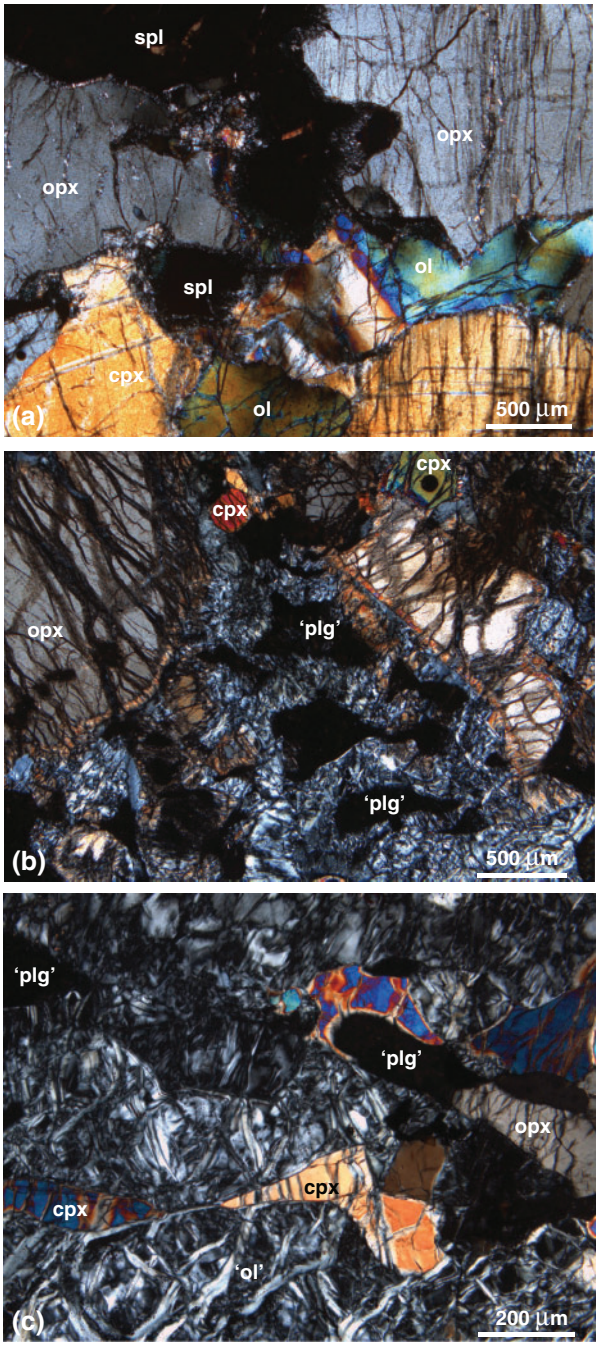

Fig. 2. Photomicrographs of the Eastern Central Alps peridotites. (a) Porphyroclastic spinel peridotite from Val Malenco (LUM-400). (b) Serpentinized plagioclase peridotite from the lower Platta unit. It should be noted that plagioclase is completely altered to chlorite. The grain size of the clinopyroxene is much smaller than the opx (Sup-2). (c) Interstitial clinopyroxene in a sample from the lower Platta unit (CRP-3). Olivine displays typical serpentine mesh texture, plagioclase is altered to chlorite. cpx, clinopyroxene; opx, orthopyroxene; ol, olivine; 'ol', serpentinized olivine; 'plg', chloritized plagioclase; spl, Cr-spinel. All images taken with crossed Nicols.

Rarely, disseminated grains of phlogopite and Ti-pargasite occur within the porphyroclastic assemblage, suggesting migration of small, volatile-rich melt fractions of unknown age. The porphyroclastic assemblage has partially been replaced by a second generation of clinopyroxene and plagioclase (±orthopyroxene) with interstitial cpx and plagioclase surrounding Cr-rich spinel (Fig. 2b and c). Although fresh plagioclase has not been found, the spinel chemistry and trace element studies on clinopyroxene strongly suggest the former presence of plagioclase. Locally, discordant contacts between serpentinized dunites or harzburgites and serpentinized plagioclase lherzolites are preserved.

Evidence for retrograde high-temperature hydration is the formation of Mg-hornblende and chlorite in coronae around pyroxene and along its cleavage planes. Locally, chlorite and Mg-hornblende form mylonites, indicating hydration of mantle rocks at relatively high temperatures, above the stability field of serpentine (Müntener *et al.*, 2000; Müntener & Hermann, 2001). This was followed by a more widespread hydration at lower temperature characterized by the crystallization of tremolite at the expense of clinopyroxene and of Mg-hornblende. Olivine was transformed into a serpentinite mesh with magnetite and locally brucite, whereas the spinel was partially altered to Cr-chlorite and magnetite (Desmurs *et al.*, 2001). Plagioclase, however, has been completely replaced by Cr-poor chlorite (Fig. 2b and c). Finally, the serpentine minerals were partially replaced by talc and calcite.

METHODS

Bulk-rock glasses were prepared by mixing appropriate proportions (1:5) of fine-grained rock powder with di-lithium tetraborate. Peridotites were analyzed by wavelength-dispersive X-ray fluorescence spectroscopy (XRF, Phillips PW 1404) at EMPA Dübendorf (Malenco samples) and at CNRG-Nancy (Platta samples). Measured intensities were corrected for instrumental drift, background and matrix effects. Trace elements were determined by XRF analysis of 10 g powder using the synthetic background method for which major element contents have to be known (Nisbet *et al.*, 1976). XRF trace element precision is generally better than 5%, except close to the limits of detections where counting statistics impose larger uncertainties. Peridotite bulk-rock trace element contents of the Malenco samples (REE, Cs, Rb, Th, U, Nb, Ta, Sr, Zr, Hf) were analyzed by inductively coupled plasma-mass spectrometry (ICP-MS) using a VG-PQ2 Turbo + system at Geosciences Montpellier (AETE Facility, Montpellier 2 University, France) and at EMPA Dübendorf, whereas the Platta samples were analysed at CNRG Nancy. For the samples analysed in Montpellier REE, Cs, Rb, Pb, Th, U, Sr, Zr, Hf, Nb and Ta concentrations were determined by external calibration

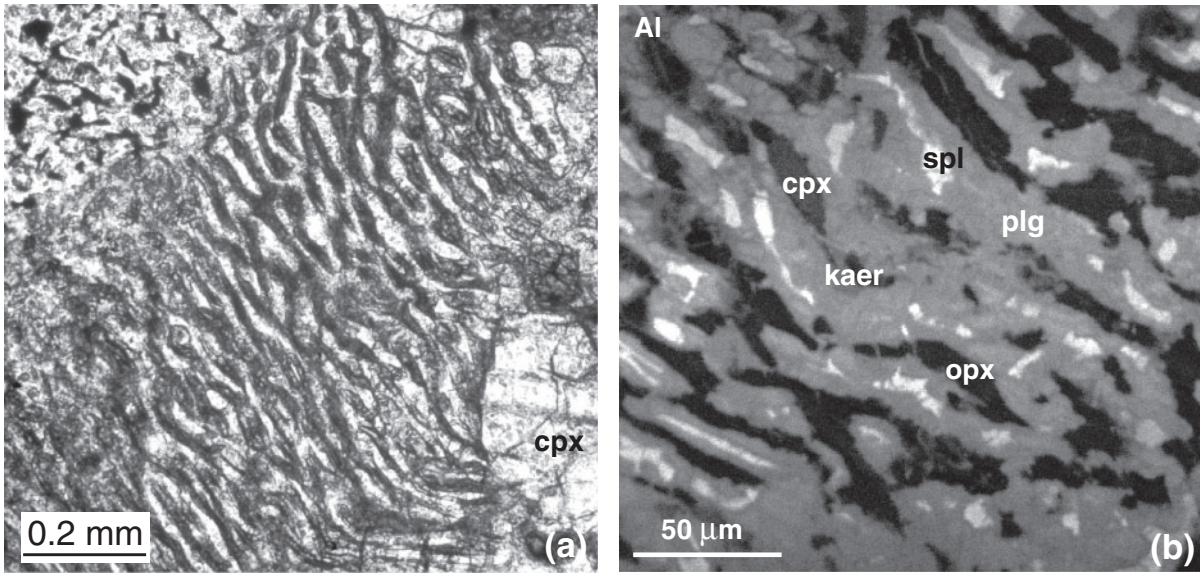

Fig. 3. Textural observations on the upper Platta peridotites. (a) Spinel pyroxene symplectite from a boudinaged pyroxenite layer from the upper Platta unit (Sample FAP-6). BSE image. (b) Al distribution map highlighting the intergrowth of pyroxenes, spinel, plagioclase and kaersutite, indicating replacement of former garnet assemblages. Abbreviations as in Fig. 2, and kaer, kaersutite.

following the HF–$HClO_4$ dissolution and analytical procedure described in detail by Ionov *et al.* (1992). Detection limits based on long-term analyses of chemical blanks at Geosciences Montpellier have been reported by Ionov *et al.* (1992) and Godard *et al.* (2008). REE, Rb, Th, U, Sr, Zr, Hf, Nb and Ta concentrations were determined by external calibration following the protocol established at EMPA Dübendorf and have been described in detail in Müntener (1997). A comparison of aliquots analyzed in both the Montpellier and Dübendorf laboratories shows generally less than 5% deviation, except for Ta, Th and U. The Dübendorf values for the latter elements were considered unreliable and are not reported.

The constituent minerals in polished thin sections of variably serpentinized peridotites were analysed by electron microprobe and laser-ablation (LA)-ICP-MS. Major elements were determined using a Cameca SX 50 at ETH Zürich and the University of Bern, using an acceleration voltage of 15 kV, a beam current of 20 nA and a spot size of 2–10μm. Natural and synthetic oxides and silicates were used as standards. The raw data were corrected using the PAP routine (Pouchou & Pichoir, 1984). Trace element concentrations of clinopyroxene, orthopyroxene, hornblende and spinel were determined by LA-ICP-MS at ETH Zürich. This system consists of a 193 nm ArF Excimer laser system [prototype to the Geolas system from Microlas, Germany; see Günther *et al.* (1997)] combined with an Elan 6100 DRC quadrupole ICP-MS system. This laser system allows optimization of the beam size for analysis (8–120 μm, adjusted via an aperture in the beam path) at constant energy density on the sample surface and perfect localization of analytical spots through a petrographic microscope using combined transmitted and reflected light. The ICP-MS system was operated at conditions similar to those reported by Pettke *et al.* (2004). Data quantification was based on SRM 610 and 612 from NIST, and data reduction employed the Lamtrace software (Jackson, 2008). Data are reported in Tables 2–11. For the ICP-MS mineral data (Tables 7–9), these include the shot-specific limits of detection for cases where no significant analyte signal was recorded.

MINERAL CHEMISTRY

Clinopyroxene

The clinopyroxenes analyzed are cores of porphyroclasts from fertile and depleted peridotites; interstitial crystals were also analyzed in some serpentinized peridotites from the lower Platta unit. Mg-numbers [= molar Mg/(Mg + Fe_{tot})] in clinopyroxene (Table 2) range from 0·92 to 0·89. Figure 4a illustrates that clinopyroxene from the Totalp, upper Platta unit and Malenco peridotite is significantly higher in Na_2O at comparable Cr_2O_3 than clinopyroxene from the lower Platta unit. Only clinopyroxene from the northern external Ligurides has Na_2O contents that are comparable with those from the Totalp, Malenco and upper Platta unit. For spinel peridotites, Fig. 4b illustrates that TiO_2 in clinopyroxene from the Malenco, upper Platta and Totalp samples systematically decreases with increasing Cr content, consistent with the host peridotites being residues of partial melting of a spinel peridotite source. Although there is significant overlap, clinopyroxene

Table 1: Locations and modes of studied peridotites from the Eastern Central Alps

Sample no.	Rock type	Unit	Location	ol	spl	cpx	opx	plg	other	% alteration
To 1	Spl. Per.	Totalp peridotite	46°50′18·6″N, 9°48′13·8″E	57	1	15	27	—	ti-hbl	40
To 7	Spl. Per.	Totalp peridotite	46°51′00·6″N, 9°49′48·9″E	57	1	15	27	—	ti-hbl	30
FAP-4*	Spl. Per.†	Upper Platta	46°32′57·4″N, 9°40′22·8″E	52·2	3·7	16·1	28·1	—	ti-hbl	70
VEP-8*	Spl. Per.	Upper Platta	46°34′18·4″N, 9°41′07·8″E	61·3	1·7	8·6	28·4	—	—	70
VEP-2*	Spl. Per.†	Upper Platta	46°34′18·4″N, 9°41′07·8″E	47·2	1·7	20·1	30·9	—	—	70
FAP-6	Spl. Per.†	Upper Platta	46°32′58·4″N, 9°40′23·0″E	49	1	22	28	trace	ti-hbl	70
MSP-1*	Spl. Plg. Per.	Lower Platta	46°27′30·7″N, 9°34′56·6″E	61·5	0·5	5·2	25·2	8·6	—	60
CRP-3/2*	Spl. Plg. Per.	Lower Platta	46°28′07·8″N, 9°37′40·6″E	51·0	1·0	16·0	25·0	7·0	—	80
NAP-7/2*	Spl. Plg. Per.	Lower Platta	46°30′28·2″N, 9°39′06·2″E	61·5	0·6	5·8	22·2	10·4	—	80
STP-5	Spl. Plg. Per.	Lower Platta	46°29′43·1″N, 9°37′18·6″E	60	1	7	26	7	—	70
STP-2*	Spl. Per.	Lower Platta	46°29′43·1″N, 9°37′18·6″E	65·0	1·4	7·0	24·4	1·0	—	70
STP-7	Spl. Plg. Per.	Lower Platta	46°29′25·6″N, 9°36′40·6″E	55	1	8	29	8	—	70
SUP-2*	Spl. Plg. Per.	Lower Platta	46°31′38·2″N, 9°37′44·6″E	59·7	0·5	3·2	27·2	9·4	—	60
NAP-6	Spl. Plg. Per.	Lower Platta	46°30′23·4″N, 9°39′13·7″E	60·0	trace	9·0	23·0	8·0	phl, ti-hbl	60
VSP-6	Spl. Plg. Per.	Lower Platta	46°30′33·8″N, 9°39′16·2″E	—	—	—	—	—	—	90
SUP-3*	Spl. Plg. Per.	Lower Platta	46°31′35·7″N, 9°37′37·8″E	61·7	0·4	1·4	28·0	8·9	—	80
Mg-65	Spl. Per.	Malenco peridotite	46°16′31·3″N, 9°50′59·5″E	—	—	—	—	—	—	90
P-UM 117*	Spl. Per.	Malenco peridotite	46°17′57·4″N, 9°47′35·5″E	60·2	1·4	8·8	29·6	—	—	40
Or-UM 224	Spl. Per.	Malenco peridotite	46°16′54·4″N, 9°48′34·6″E	70	1	8	21	—	ti-hbl	40
LUM-216*	Spl. Per.	Malenco peridotite	46°17′16·9″N, 9°48′06·1″E	62·1	1·6	9·7	26·6	—	phl, ti-hbl	10
LUM-400*	Spl. Per.	Malenco peridotite	46°18′11·6″N, 9°49′43·6″E	66·2	1·4	7·0	24·4	—	ti-hbl	<5
LUM-112*	Spl. Per.	Malenco peridotite	46°18′11·6″N, 9°49′43·6″E	72·3	2·3	5·4	20·0	—	ti-hbl	10
VEP-7*	Spl. Per.	Upper Platta	46°34′18·4″N, 9°41′07·8″E	36·7	3·6	28·9	30·7	—	—	70
FAP-3-I*	Spl. Per.	Upper Platta	46°32′58·4″N, 9°40′23·0″E	61·5	1·4	8·9	28·1	—	—	80
NAP-2*	Spl. Plg. Per.	Lower Platta	46°30′29·5″N, 9°39′08·2″E	55·6	0·5	10·2	26·4	7	—	80
NAP-3*	Spl. Per.	Lower Platta	46°30′29·5″N, 9°39′08·2″E	70·2	1·5	—	28·1	—	—	90
LAP-1*	Spl. Plg. Per.	Lower Platta	46°30′23·2″N, 9°29′06·2″E	60·6	0·5	6·4	27·5	5	—	90
SUP-4*	Spl. Plg. Per.	Lower Platta	46°31′38·2″N, 9°37′44·6″E	58·9	0·9	3·3	30·4	6·5	—	60
SUP-5*	Spl. Plg. Per.	Lower Platta	46°31′36·2″N, 9°37′42·5″E	58·1	0·6	4·2	29·5	8·4	—	80
STP-1*	Spl. Plg. Per.	Lower Platta	46°29′48·0″N, 9°37′07·0″E	59·9	0·7	6·1	26·2	9	—	80
STP-3*	Spl. Plg. Per.	Lower Platta	46°29′43·1″N, 9°37′18·6″E	60	0·5	4·8	29·8	4·9	—	60
CRP-1	Spl. Plg. Per.	Lower Platta	46°28′07·8″N, 9°37′40·6″E	—	—	—	—	—	—	90
LUM-217*	Spl. Per.	Malenco	46°17′16·9″N, 9°48′06·1″E	70	1·4	7	21·6	—	—	20
LUM-226*	Spl. Per.	Malenco	46°17′16·9″N, 9°48′06·1″E	71	1	4	24	—	—	50
LUM-228*	Spl. Per.	Malenco	46°17′16·9″N, 9°48′06·1″E	68	1·5	7·6	22·9	—	—	10
Or-UM 201*	Spl. Per.	Malenco	46°17′04·4″N, 9°48′29·6″E	61	2	9·3	27·7	—	—	50
Or-UM 234*	Spl. Per.	Malenco	46°17′02·0″N, 9°48′31·5″E	66	1·5	8	24·5	—	ti-hbl	40
Or-UM 235*	Spl. Per.	Malenco	46°17′02·0″N, 9°48′31·5″E	71	1·8	7·7	19·5	—	—	25
Or-UM 236*	Spl. Per.	Malenco	46°17′02·0″N, 9°48′31·5″E	68	1·8	6·5	23·7	—	ti-hbl	30
Or-UM 309h*	Spl. Per.	Malenco	46°17′02·0″N, 9°44′31·4″E	73·6	1·6	1·5	23·3	—	ti-hbl	50
LUM-109*	Spl. Per.	Malenco	46°18′11·6″N, 9°49′43·6″E	68·5	2·2	6·6	22·7	—	—	20
LUM-111*	Spl. Per.	Malenco	46°18′11·6″N, 9°49′43·6″E	68·7	2·2	6·3	22·8	—	—	20
B-UM201*	Serp. Per.	Malenco	46°16′55·5″N, 9°49′48·0″E	46·1	1·1	10·0	42·8	—	—	90
P-UM 16*	Serp. Per.	Malenco	46°17′44·4″N, 9°47′31·5″E	53·5	2·0	17·5	27·0	—	—	80
P-UM 18*	Serp. Per.	Malenco	46°17′44·4″N, 9°47′31·5″E	59	1·9	10·3	28·8	—	—	60
P-UM 24*	Serp. Per.	Malenco	46°17′49·4″N, 9°47′28·6″E	60·2	1·9	10·0	27·9	—	—	80
P-UM 116*	Serp. Per.	Malenco	46°17′47·4″N, 9°47′38·3″E	57·5	1·8	13·2	27·5	—	—	80

(continued)

Table 1: Continued

Sample no.	Rock type	Unit	Location	ol	spl	cpx	opx	plg	other	% alteration
D-UM 24*	Serp. Per.	Malenco	46°17′43·4″N, 9°47′31·5″E	55·8	1·7	4·7	37·8	—	—	90
D-UM 15*	Serp. Per.	Malenco	46°17′43·4″N, 9°47′31·4″E	57·0	1·5	6·4	35·1	—	—	90
C10-5	Serpentinite	Malenco	46°14′45·6″N, 9°48′23·6″E	—	—	—	—	—	—	
P7-1	Serpentinite	Malenco	46°14′28·3″N, 9°45′24·1″E	—	—	—	—	—	—	
P56-57	Serpentinite	Malenco	46°14′30·1″N, 9°45′24·1″E	—	—	—	—	—	—	
P111-111	Serpentinite	Malenco	46°14′44·9″N, 9°46′55·4″E	—	—	—	—	—	—	
C19-10	Serpentinite	Malenco	46°14′20·5″N, 9°46′43·6″E	—	—	—	—	—	—	
P115-119	Serpentinite	Malenco	46°14′21·1″N, 9°45′33·9″E	—	—	—	—	—	—	
P61-63	Serpentinite	Malenco	46°14′21·4″N, 9°45′18·0″E	—	—	—	—	—	—	
P60-62	Serpentinite	Malenco	46°14′28·1″N, 9°45′19·1″E	—	—	—	—	—	—	
P49-50	Serpentinite	Malenco	46°14′46·6″N, 9°45′12·8″E	—	—	—	—	—	—	
P43-41	Serpentinite	Malenco	46°15′00·8″N, 9°45′23·7″E	—	—	—	—	—	—	
T88-83	Serpentinite	Malenco	46°14′48·8″N, 9°44′46·2″E	—	—	—	—	—	—	
P67-66	Serpentinite	Malenco	46°14′33·8″N, 9°44′37·8″E	—	—	—	—	—	—	
C85-81	Serpentinite	Malenco	46°14′59·3″N, 9°44′36·2″E	—	—	—	—	—	—	
P73-73	Serpentinite	Malenco	46°14′59·3″N, 9°44′35·4″E	—	—	—	—	—	—	
C55-54	Serpentinite	Malenco	46°14′59·0″N, 9°44′35·8″E	—	—	—	—	—	—	
P70-69	Serpentinite	Malenco	46°14′43·3″N, 9°44′28·3″E	—	—	—	—	—	—	

*Modal composition calculated by least-squares regression (Mannor, written by P. Ulmer) using bulk-rock compositions, assuming $Fe^{3+} = 0$, Tschermaks-in-pyx = 0·05. All other modes are visual estimates based on thin-section observations; no data are provided for Mg-65 (antigorite serpentinite, with relics of primary cpx), VSP-6 (fine-grained peridotite mylonite) or for all the samples labeled serpentinite (almost no mantle relicts were found). Per cent alteration includes partially serpentinized mantle minerals and altered plagioclase.
†Spinel peridotite with pyroxenite layers.

Table 2: Major element compositions of clinopyroxenes from peridotites of the Eastern Central Alps

Sample:	VEP-11		FAP-4*		VEP-8*		VEP-3		FAP-6		MSP-1*		CRP-3/2*		NAP-7/2*	
Location:	UPLT		UPLT		UPLT		UPLT		UPLT		LPLT		LPLT		LPLT	
n:	8	2s	6	2s	10	2s	5	2s	4	2s	5	2s	9	2s	6	2s
SiO_2	51·72	0·41	51·17	0·21	51·87	0·41	51·51	0·65	50·78	0·97	50·48	0·61	51·30	0·59	49·43	1·32
TiO_2	0·61	0·09	0·80	0·07	0·53	0·04	0·47	0·03	0·66	0·25	0·66	0·13	0·72	0·04	0·84	0·06
Cr_2O_3	0·98	0·16	0·58	0·11	0·95	0·22	0·74	0·03	0·78	0·15	1·14	0·07	1·12	0·07	0·83	0·04
Al_2O_3	6·45	0·58	6·42	0·48	6·19	0·36	6·40	0·98	6·83	0·40	5·00	0·52	4·42	0·69	5·38	0·38
FeO	2·73	0·44	3·18	0·25	2·50	1·21	2·49	0·49	2·62	0·54	2·98	0·14	3·00	0·15	3·60	0·35
MnO	0·07	0·02	0·09	0·01	0·11	0·03	0·08	0·04	0·06	0·03	0·10	0·02	0·10	0·02	0·11	0·02
MgO	15·32	0·84	15·15	0·51	15·18	0·72	14·60	0·29	15·22	0·63	15·78	0·23	16·05	0·51	16·42	1·99
NiO	0·04	0·04	0·05	0·03	0·04	0·02	0·06	0·03	0·05	0·03	0·06	0·05	0·05	0·03	0·04	0·01
CaO	20·10	1·02	21·41	0·63	21·21	0·89	21·56	0·90	20·94	1·10	22·65	0·32	23·02	0·42	21·86	2·41
Na_2O	1·65	0·22	1·41	0·21	1·46	0·51	1·70	0·48	1·41	0·37	0·43	0·06	0·65	0·08	0·62	0·11
Σ	99·8		100·2		100·1		99·8		99·5		99·3		100·5		99·1	
Mg-no.	0·909		0·895		0·916		0·913		0·912		0·904		0·905		0·891	

(continued)

Table 2: Continued

Sample:	STP-5*		STP-2*		STP-7		STP-4		SUP-2		NAP-6		SUP-3		NAP-5	
Location:	LPLT		LPLT		LPLT		LPLT		LPLT		LPLT		LPLT		LPLT	
n:	10	2σ	25	2σ	6	2σ	5	2σ	4	2σ	4	2σ	3	2σ	5	2σ
SiO_2	51·01	0·49	52·16	0·41	50·80	0·39	51·05	0·46	50·10	1·00	53·18	0·61	51·16	0·66	50·84	0·58
TiO_2	0·89	0·06	0·24	0·04	0·76	0·12	0·93	0·07	0·94	0·02	0·23	0·11	0·76	0·02	0·86	0·12
Cr_2O_3	0·94	0·04	0·81	0·07	1·01	0·13	1·01	0·07	1·01	0·05	0·64	0·20	1·02	0·01	1·00	0·12
Al_2O_3	4·51	0·35	4·90	0·31	5·58	0·63	4·43	0·32	4·70	0·17	4·49	0·86	4·54	0·56	4·24	0·66
FeO	3·19	0·42	2·48	0·12	3·08	0·30	2·93	0·31	3·11	0·20	2·46	0·14	3·00	0·60	2·95	0·17
MnO	0·07	0·03	0·10	0·02	0·06	0·04	0·10	0·03	0·10	0·03	0·09	0·02	0·10	0·02	0·10	0·03
MgO	16·34	0·37	16·35	0·43	15·96	0·71	16·02	0·56	15·99	0·77	16·21	0·30	16·11	0·74	15·98	0·48
NiO	0·04	0·03	0·04	0·03	0·06	0·04	0·04	0·03	0·07	0·03	0·05	0·04	0·07	0·03	0·04	0·03
CaO	22·28	0·37	22·29	0·47	22·28	0·94	22·92	1·05	22·42	0·77	22·09	0·61	22·02	0·72	0·66	0·06
Na_2O	0·59	0·04	0·69	0·04	0·70	0·11	0·59	0·06	0·70	0·02	0·76	0·14	0·58	0·08	0·01	0·01
Σ	99·8		100·1		100·3		100·4		99·1		100·2		99·4		99·6	
Mg-no.	0·901		0·922		0·902		0·911		0·902		0·922		0·906		0·906	

Sample:	Mg-65		P-UM 117		Or-UM 224*		LUM-216*		LUM-400*		LUM-112*		To-7*		Totalp-7*	
Location:	MAL		MAL		MAL		MAL		MAL		MAL		DAV		DAV	
n:	11	2σ	17	2σ	6	2σ	5	2σ	5	2σ	4	2σ	4	2σ	5	2σ
SiO_2	50·43	0·18	50·97	0·36	52·24	0·22	52·98	0·22	53·33	0·23	53·35	0·11	51·35	0·36	51·51	0·29
TiO_2	0·76	0·03	0·96	0·05	0·56	0·09	0·52	0·03	0·35	0·02	0·30	0·03	0·62	0·05	0·61	0·05
Cr_2O_3	0·80	0·03	0·83	0·07	0·95	0·04	0·89	0·04	0·98	0·07	1·22	0·08	0·77	0·04	0·78	0·06
Al_2O_3	5·86	0·16	6·97	0·40	6·58	0·21	6·90	0·19	5·49	0·06	5·33	0·09	7·07	0·31	6·91	0·28
FeO	3·32	0·19	2·61	0·06	2·29	0·08	2·45	0·08	2·17	0·12	2·11	0·07	2·35	0·06	2·40	0·13
MnO	0·10	0·02	0·09	0·02	0·07	0·01	0·09	0·03	0·07	0·01	0·08	0·03	0·04	0·05	0·06	0·03
MgO	16·35	0·49	14·22	0·50	14·54	0·16	14·76	0·43	15·63	0·23	15·21	0·13	14·10	0·27	14·52	0·14
NiO	0·05	0·02	0·04	0·02	0·03	0·01	0·03	0·03	0·05	0·02	0·05	0·03	0·03	0·02	0·03	0·04
CaO	22·36	0·65	21·82	0·35	21·04	0·16	20·84	0·67	21·42	0·28	21·42	0·12	21·91	0·27	21·64	0·30
Na_2O	0·76	0·06	1·71	0·09	2·00	0·08	2·01	0·07	1·55	0·05	1·65	0·03	1·82	0·11	1·93	0·09
Σ	100·8		100·2		100·3		101·5		101·1		100·7		100·1		100·4	
Mg-no.	0·898		0·906		0·919		0·915		0·928		0·928		0·915		0·915	

Concentrations in wt %; MAL, Malenco peridotite; LPLT, lower Platta unit; UPLT, upper Platta unit; DAV, Davos peridotite (for location see Fig. 1); *n*, number of analyses; 2σ, standard deviation of the mean. Analytical conditions: wavelength-dispersive spectrometers on a Cameca SX50 electron microprobe; 15 kV acceleration voltage, 20 nA beam current, beam size of ~1 μm, 20s counting time on peak and half that time on background position on either side of the peak, 10 s for Na. A ZAF-type correction procedure was applied to the data. K_2O <0·01.
*Data from Müntener *et al.* (2004).

TiO_2 contents from the lower Platta unit generally fall off the trend described by clinopyroxenes from the spinel peridotites. The high Ti and Cr contents of many lower Platta and Iberia samples is characteristic of plagioclase peridotites and has been interpreted as the result of either subsolidus equilibration (Rampone *et al.*, 1993) or refertilization and melt–rock reaction with migrating liquids at shallow pressures (Rampone *et al.*, 1997; Müntener & Piccardo, 2003). However, two samples from the lower Platta unit are substantially lower in TiO_2 and also in other incompatible elements (see below).

The Sc–V relationships of the clinopyroxenes are displayed in Fig. 5, together with data for garnet pyroxenites from Totalp and Malenco (O. Müntener, unpublished data).

Table 3: Major element compositions of orthopyroxene from peridotites of the Eastern Central Alps

Sample:	FAP-6		SUP-2		MSP-1		LUM-216		LUM-400		LUM-112		To-7		Totalp-7	
Location:	PLT		PLT		PLT		MAL		MAL		MAL		DAV		DAV	
n:	4	2σ	4	2σ	5	2σ	8	2σ	4	2σ	7	2σ	4	2σ	3	2σ
SiO_2	55·83	1·11	54·52	1·12	54·69	0·75	55·28	0·14	55·48	0·17	55·13	0·22	54·16	0·83	55·09	0·84
TiO_2	0·20	0·08	0·25	0·06	0·25	0·02	0·12	0·01	0·07	0·01	0·06	0·02	0·14	0·03	0·13	0·02
Al_2O_3	3·18	0·95	3·35	0·44	3·27	0·21	4·07	0·16	3·98	0·25	3·93	0·19	4·79	0·28	4·69	0·27
Cr_2O_3	0·22	0·05	0·61	0·03	0·70	0·12	0·36	0·04	0·48	0·03	0·57	0·03	0·34	0·05	0·32	0·04
FeO	6·08	0·51	6·68	0·98	6·81	0·54	6·17	0·17	5·60	0·14	5·84	0·16	6·65	0·17	6·40	0·15
MnO	0·15	0·03	0·15	0·03	0·18	0·01	0·13	0·04	0·13	0·01	0·12	0·02	0·13	0·05	0·12	0·03
NiO	0·08	0·05	0·09	0·03	0·08	0·04	0·09	0·03	0·08	0·01	0·10	0·02	0·09	0·03	0·09	0·03
MgO	33·97	0·58	32·87	0·45	31·83	0·35	33·21	0·14	33·51	0·16	33·89	0·16	33·02	0·46	33·81	0·16
CaO	0·55	0·10	1·01	0·58	1·67	0·38	0·51	0·07	0·57	0·05	0·42	0·03	0·52	0·09	0·45	0·08
Na_2O	0·02	0·02	0·03	0·03	0·06	0·03	0·07	0·02	0·07	0·01	0·03	0·01	0·06	0·02	0·06	0·01
Σ	100·3		99·7		99·6		100·0		100·0		100·0		99·9		101·2	
Mg-no.	0·909		0·898		0·893		0·906		0·914		0·912		0·898		0·904	

Table 4: Major element compositions of olivine from peridotites of the Eastern Central Alps

Sample:	Or-UM-224		LUM-216		LUM-400		LUM-112		To-7		Totalp-7	
Location:	MAL		MAL		MAL		MAL		DAV		DAV	
n:	3	2σ	8	2σ	4	2σ	5	2σ	5	2σ	4	2σ
SiO_2	40·22	0·75	40·78	0·14	41·04	0·06	40·72	0·25	40·84	0·25	41·13	0·43
TiO_2	<0·01		0·01	0·01	<0·01		<0·01		0·00	0·01	0·01	0·01
Cr_2O_3	0·03	0·01	0·01	0·01	<0·01		<0·01		0·01	0·02	0·00	0·00
Al_2O_3	<0·01		0·01	0·01	0·04	0·03	<0·01		0·01	0·01	0·02	0·02
FeO	11·99	0·19	9·95	0·14	8·63	0·16	9·63	0·37	10·66	0·27	9·84	0·16
MnO	0·20	0·03	0·15	0·03	0·17	0·01	0·15	0·02	0·15	0·01	0·20	0·05
MgO	47·45	0·35	48·66	0·15	49·68	0·17	49·08	0·38	49·04	0·20	49·85	0·57
NiO	0·38	0·04	0·42	0·06	0·40	0·03	0·40	0·03	0·41	0·03	0·42	0·03
CaO			0·01	0·01	0·02	0·00			0·01	0·01	0·03	0·05
Σ	100·3		100·0		100·0		100·0		101·1		101·5	
Mg-no.	0·871		0·897		0·911		0·901		0·886		0·894	

Concentrations reported in wt %; MAL, Malenco peridotite; PLT, Platta peridotite; DAV, Davos peridotite; *n*, number of analyses; 2σ, standard deviation of the mean. Na_2O <0·03, K_2O <0·01. No olivine is preserved in samples from the Platta nappe.

Most spinel peridotites have relatively low Sc and V contents, with the exception of some clinopyroxene from the upper Platta unit where Sc is higher or lower for a given V content. In accordance with textural observations (Fig. 3), some of the upper Platta clinopyroxenes are interpreted to preserve a garnet signature, either by replacing garnet (high Sc, low V) or by preserving a signature (low Sc, high V) that recalls equilibration with garnet. In contrast, plagioclase peridotites show a positive correlation between Sc and V (Fig. 5), with the most enriched samples approaching the composition of primitive N-MORB clinopyroxene (e.g. Vannucci *et al.*, 1993*a*).

Table 5: Major element compositions of spinel from peridotites of the Eastern Central Alps

Sample:	CRP-3		Sup-2		MSP-1		STP-5		STP-1	NAP-5		FAP-6		SUP-3	
Location:	PLT		PLT		PLT		PLT		PLT	PLT		PLT		PLT	
n:	11	2σ	6	2σ	10	2σ	6	2σ	1	5	2σ	5	2σ	6	2σ
SiO_2	<0·02		<0·02		<0·02		<0·02		0·08	<0·02		<0·02		0·38	0·54
TiO_2	0·90	0·42	0·58	0·13	0·63	0·18	0·58	0·08	0·69	0·37	0·16	0·08	0·02	0·53	0·01
Cr_2O_3	32·54	0·74	30·73	2·31	33·03	2·81	28·52	0·88	35·51	32·16	0·84	10·36	2·26	27·38	0·21
Fe_2O_3	30·44	0·31	31·74	2·54	29·81	6·78	34·74	1·02	28·05	31·00	1·31	56·91	2·55	35·85	0·86
Al_2O_3	5·71	0·88	6·15	0·79	4·28		6·00	0·73	6·33	6·71	0·56	1·35		5·07	
FeO	15·65	0·50	15·22	1·36	18·44	1·52	15·75	1·05	17·62	15·84	0·68	10·33	0·68	13·39	0·05
MnO	0·61	0·07	0·31	0·02	0·14	0·03	0·34	0·05	0·37	0·40	0·02	—	—	0·29	0·01
MgO	13·73	0·12	13·92	1·04	11·59	2·12	14·41	0·86	12·64	13·57	0·51	19·60	0·75	15·60	0·16
NiO	0·21	0·05	0·22	0·05	0·18	0·06	0·20	0·03	0·17	0·18	0·03	0·36	0·05	0·20	0·01
CaO	0·01	0·01	<0·01		0·05	0·03	<0·01		0·04	<0·01	0·00	0·06	0·04	0·37	0·52
Σ	99·8		98·9		98·2		100·2		101·5	100·3		99·1		99·1	
Mg-no.	0·540		0·544		0·481		0·548		0·491	0·525		0·763		0·608	

Sample:	LUM-216		LUM-400		LUM-112		To-7		Totalp-7	
Location:	MAL		MAL		MAL		DAV		DAV	
n:	8	2σ	3	2σ	7	2σ	4	2σ	4	2σ
SiO_2	<0·02		<0·02		<0·02		0·01	0·01	<0·02	
TiO_2	0·18	0·03	0·11	0·10	0·04	0·02	0·06	0·01	0·04	0·01
Cr_2O_3	11·10	0·13	14·90	0·33	18·80	0·17	9·09	0·51	8·47	0·81
Al_2O_3	56·00	0·51	53·70	0·29	48·10	0·17	58·73	0·40	59·21	0·59
Fe_2O_3	1·43		0·44		1·87		1·06	0·54	1·77	0·28
FeO	12·20	0·31	11·70	0·84	14·50	0·21	10·40	0·69	10·23	0·37
MnO	0·16	0·02	0·17	0·01	0·31	0·02	0·10	0·01	0·12	0·01
MgO	18·40	0·22	18·60	0·39	16·00	0·09	19·86	0·47	20·11	0·27
NiO	0·36	0·05	0·32	0·05	0·23	0·05	0·40	0·05	0·44	0·03
CaO	<0·01		<0·01		<0·01		0·01	0·01	0·01	0·02
Σ	99·8		99·9		99·9		99·6		100·3	
Mg-no.	0·729		0·739		0·663		0·76		0·76	

Concentrations reported in wt %; MAL, Malenco peridotite; PLT, Platta peridotite; DAV, Davos peridotite (for location see Table 1); *n*, number of analyses; 2σ, standard deviation of the mean. $Na_2O < 0·02$ wt %.

Clinopyroxene REE patterns from spinel and plagioclase lherzolites are illustrated in Fig. 6. Most clinopyroxenes from spinel peridotites (Fig. 6a and c) have moderately depleted trace element patterns with a weak LREE to HREE fractionation (Ce_N/Yb_N: 0·25–0·78), weak but variable positive and negative Sr anomalies and no Eu anomaly. Based on their REE and other incompatible element contents (Fig. 6b and d), the peridotites from the lower Platta unit can be divided into three groups. (1) Six out of nine samples show convex-upward REE patterns with high middle REE (MREE) contents (Gd_N, 15–30; $Gd_N/Yb_N > 1$) and a significant negative Eu and Sr anomaly, indicating equilibration with plagioclase. (2) Clinopyroxene with a strongly fractionated REE pattern (STP-2: $Ce_N/Yb_N < 0·01$, $Gd_N/Yb_N = 0·66$, Ti/Zr = 1470) similar to that of depleted clinopyroxene from abyssal peridotites (Johnson *et al.*, 1990; Hellebrand *et al.*, 2002) locally occurs next to fertile plagioclase peridotite in the same outcrop. Such a trace element pattern has been interpreted by Müntener *et al.* (2004) as the product of near fractional melting in the garnet stability field, followed by an approximately equal amount of melting in the spinel stability

Table 6: Major element compositions of pargasite from peridotites of the Eastern Central Alps

Sample:	SUP-2		STP-4		FAP-6		Or-UM 224	LUM-216		LUM-400		LUM-112		To-7		Totalp-7
Location:	LPLT		LPLT		UPLT		MAL	MAL		MAL		MAL		DAV		DAV
n:	3	2σ	4	2σ	3	2σ	1	1	1	1	1	1	1	4	2σ	1
SiO_2	42·32	1·32	42·86	0·76	41·30	0·34	42·38	43·66	42·34	45·53	43·65	43·65	44·37	42·32	0·26	41·63
TiO_2	3·52	0·38	3·33	0·36	5·60	0·65	3·65	5·58	5·08	3·25	3·81	3·37	3·28	3·72	0·20	3·21
Cr_2O_3	1·74	0·08	1·46	0·28	0·99	0·10	1·08	1·21	1·04	0·94	1·29	1·46	1·16	0·72	0·08	0·73
Al_2O_3	12·39	0·31	11·83	0·72	13·23	0·19	12·87	13·64	14·02	12·64	13·64	13·57	13·10	14·40	0·42	13·67
Fe_2O_3	0·71		0·42		0·14		0·89	0·00	0·00	0·41	0·00	0·00	1·15	0·72	1·25	0·89
FeO	3·63	0·98	4·15	0·49	3·99	0·40	3·20	2·66	3·19	2·26	2·45	3·49	2·36	3·62	1·06	3·36
MnO	0·06	0·01	0·04	0·01	0·04	0·04	0·12	0·05	0·12	0·03	0·08	0·11	0·06	0·05	0·01	0·00
MgO	16·92	0·34	16·94	0·71	15·97	0·41	18·00	18·59	17·35	18·59	18·18	17·39	18·10	16·86	0·26	16·84
NiO	0·13	0·03	0·11	0·01	0·10	0·05	0·12	0·04	0·12	0·07	0·08	0·06	0·13	0·11	0·03	0·10
CaO	12·13	0·49	12·55	0·22	11·83	0·24	11·84	12·26	11·88	12·30	12·62	12·03	11·96	11·92	0·27	12·29
Na_2O	3·40	0·06	2·96	0·17	3·48	0·10	3·97	3·12	2·97	2·89	3·12	3·43	3·40	3·54	0·19	2·77
K_2O	0·07	0·02	0·02	0·01	0·20	0·09	0·05	0·01	0·87	0·13	0·01	0·20	0·17	0·36	0·05	0·32
Cl	–	–	–	–	–	–	0·01	–	0·08	0·01	0·01	–	–	–	–	–
Σ	99·1		98·7		98·9		100·2	101·3	101·1	101·2	101·4	100·9	101·4	100·1		100·4
Mg-no.	0·876		0·870		0·874		0·889	0·926	0·894	0·926	0·930	0·899	0·905	0·915		0·915

Concentrations reported in wt %; MAL, Malenco peridotite; PLT, Platta peridotite; DAV, Davos peridotite; *n*, number of analyses; 2σ, standard deviation of the mean. Representative single spot analyses are indicated by $n = 1$.

field. (3) One sample (NAP 99-6) has a concave-downward REE pattern with $(Ce/Yb)_N > 1$, and no Eu anomaly. Furthermore, this sample has $Zr_N/Hf_N > 1$ and identical MREE to HREE contents to sample STP-2, but shows essentially flat LREE to MREE and significant positive Nb and Ta anomalies. Such a trace element pattern can be explained by post-melting metasomatism and trace element enrichment as indicated by the presence of small grains of phlogopite in this sample.

Orthopyroxene

Orthopyroxene (opx) porphyroclasts were analysed in eight samples and show well-equilibrated and homogeneous core composition for most elements, as shown by the small standard deviations (Table 3). The CaO content of orthopyroxene in spinel peridotite is generally lower than 0·6 wt %, indicating subsolidus equilibration. CaO is significantly higher in two samples from the lower Platta unit. The higher CaO and the lower Al_2O_3 content are consistent with equilibration with plagioclase. Chondrite-normalized orthopyroxene REE patterns are illustrated in Fig. 7. Most of the samples show strong LREE depletion, with $(Ce/Yb)_N < 0·1$. One sample (FAP 6) shows evidence for being derived from garnet breakdown, as demonstrated by the symplectitic intergrowth with pyroxene, spinel and plagioclase (Fig. 3). This anomalous sample exhibits a steep REE pattern with $(Ce/Yb)_N < 0·005$, and high REE content.

Spinel

Spinel compositions unaffected by subsequent Alpine metamorphism could be determined in 13 samples (Table 5). They show a bimodal distribution of Cr-number [= molar Cr/(Cr + Al)], spinel peridotites being lower than 0·22, and plagioclase peridotites (lower Platta unit) varying between 0·35 and 0·47 (Fig. 8a). The TiO_2 content of spinel is an additional monitor for the presence or absence of plagioclase, elevated contents being a characteristic feature of plagioclase peridotites (Dick, 1989). In the lower Platta unit spinels with Cr-number >0·35 have TiO_2 contents well above 0·35 wt % (Fig. 8b). One Ti-pargasite and phlogopite-bearing spinel peridotite from Malenco reaches 0·18 wt % TiO_2, indicating that its spinel compositions might have been modified by migrating alkaline melts. The spinel data from this study are similar to data from other areas of the Alps (Ligurides, Lanzo) and overlap with spinel compositions from the Iberia–Newfoundland margin. The variation extends to lower Cr-numbers than Iberia and Newfoundland, indicating less depletion in the Alpine samples.

Table 7: Trace element compositions of clinopyroxene, Eastern Central Alps peridotites

	Upper Platta unit								Lower Platta unit											
	CUP*		FAP-4*		VEP-8*		FAP-6		STP-7*		SUP-2*		MSP-1*		CRP-3/2*		NAP-7/2*		VSP-6*	
n:	3	2σ	3	2σ	3	2σ	4	2σ	6	2σ	4	2σ	5	2σ	2	2σ	6	2σ	6	2σ
Li (μg/g)	3·5	0·3	3·3	1·5	3·0	0·6	—		3·7	1·5	2·4	0·6	5·7	1·1	2·3	0·4	3·9	1·0	2·6	0·7
B	—		—		—		—		—		—		—		—		—		—	
Sc	53·2	10·2	91·7	5·7	44·4	2·3	59·4	14·9	58·6	4·6	91·4	4·5	103·4	3·4	82·1	3·1	77·1	4·5	73·3	3·6
Ti	4077	42	4802	53	2788	42	3261	149	3517	330	5642	172	4073	0	6030	25	6187	346	4471	368
V	292	14	299	3	273	5	280	11	263	13	342	10	462	38	351	10	335	18	314	12
Cr	4721	118	3968	228	7258	149	6367	874	6668	631	6856	422	7732	566	6813	203	5688	640	5651	150
Co	—		—		—		—		—		—		—		—		—			
Ni	—		—		—		349	8	—		—		—		—		—			
Zn	—		—		5·94	0·86	7·53	0·17	9·39	1·49	—		—		—		—		9·89	0·83
Rb	<0·047		<0·036		<0·042		<0·037		0·31	0·26	<0·037		<0·054		<0·044		<0·046		0·02	0·01
Sr	70·36	4·22	46·47	1·81	49·60	2·69	69·80	5·29	14·18	2·74	8·19	0·91	4·35	0·56	6·63	0·23	5·24	1·05	6·17	0·95
Y	16·61	0·43	32·03	2·86	18·70	0·41	20·06	3·03	23·17	2·09	28·56	3·02	20·53	0·20	40·33	0·05	32·62	1·35	28·35	2·23
Zr	26·79	0·51	26·67	1·56	26·59	0·74	34·93	4·04	53·31	6·37	57·04	7·02	24·74	0·88	66·83	0·75	61·63	3·85	57·29	6·22
Nb	0·25	0·13	<0·053		<0·046		0·35	0·05	0·05	0·02	0·37	0·25	0·16	0·03	0·12	0·05	0·15	0·06	0·24	0·07
Cs	<0·015		<0·017		<0·018		—		0·27	0·20	<0·010		0·13	0·07	<0·021		<0·011		<0·009	
Ba	<0·110		<0·110		<0·105		0·13	0·03	0·50	0·23	<0·072		0·35	0·17	<0·11		<0·065		<0·078	
La	1·27	0·06	0·63	0·09	0·60	0·01	—		2·06	0·22	1·08	0·14	0·81	0·08	1·05	0·05	1·00	0·04	1·10	0·07
Ce	4·32	0·15	3·28	0·01	2·29	0·05	4·15	0·03	10·39	0·94	5·77	0·69	3·70	0·17	6·44	0·06	5·59	0·14	5·71	0·26
Pr	0·74	0·06	0·74	0·01	0·49	0·03	0·76	0·01	1·96	0·17	1·23	0·11	0·65	0·05	1·38	0·01	1·20	0·07	1·18	0·05
Nd	4·36	0·14	5·17	0·36	3·36	0·15	4·68	0·09	11·23	0·92	7·54	0·50	3·86	0·20	9·05	0·36	7·75	0·26	7·72	0·56
Sm	1·88	0·28	2·48	0·21	1·58	0·03	1·83	0·07	3·33	0·31	3·06	0·31	1·78	0·11	3·91	0·34	3·18	0·07	3·06	0·29
Eu	0·67	0·04	0·91	0·11	0·72	0·01	0·83	0·04	1·16	0·10	0·98	0·11	0·57	0·05	1·21	0·05	1·10	0·05	1·06	0·05
Gd	2·56	0·07	3·38	0·26	2·63	0·17	2·58	0·13	3·80	0·28	4·30	0·47	2·74	0·19	5·57	0·12	4·86	0·25	4·32	0·30
Tb	0·46	0·05	0·75	0·08	0·51	0·01	0·54	0·06	0·68	0·08	0·84	0·02	0·56	0·02	1·05	0·01	0·85	0·03	0·83	0·08
Dy	3·08	0·04	5·60	0·41	3·40	0·09	3·58	0·51	4·45	0·39	5·53	0·33	3·73	0·22	7·32	0·29	6·10	0·36	5·31	0·50
Ho	0·62	0·01	1·30	0·13	0·75	0·03	0·79	0·12	0·95	0·09	1·12	0·09	0·82	0·02	1·56	0·08	1·28	0·05	1·15	0·13
Er	1·58	0·10	4·00	0·56	2·07	0·01	2·25	0·45	2·50	0·31	3·37	0·24	2·35	0·04	4·42	0·10	3·59	0·16	3·02	0·28
Tm	0·22	0·02	0·53	0·04	0·30	0·00	0·32	0·05	0·36	0·04	0·43	0·02	0·32	0·01	0·62	0·02	0·50	0·03	0·41	0·04
Yb	1·84	0·04	3·63	0·16	2·03	0·06	2·14	0·18	2·21	0·17	2·66	0·21	1·90	0·10	4·00	0·27	3·07	0·20	2·70	0·22
Lu	0·27	0·04	0·62	0·13	0·29	0·01	0·31	0·05	0·30	0·03	0·37	0·03	0·23	0·00	0·51	0·00	0·44	0·02	0·36	0·03
Hf	0·84	0·05	1·18	0·09	1·07	0·14	1·01	0·09	1·33	0·13	2·07	0·20	0·89	0·06	1·65	0·11	1·81	0·14	1·68	0·17
Ta	0·02	0·04	<0·035		<0·007		0·05	0·00	0·01	0·01	<0·020		<0·029		0·03	0·01	0·02	0·00	0·03	0·01
Th	0·03	0·02	<0·018		<0·005		0·04	0·01	0·02	0·01	0·04	0·01	<0·017		<0·015		0·02	0·01	0·03	0·01
U	0·02	0·02	<0·017		<0·006		0·03	0·01	0·02	0·01	<0·009	—	<0·018		<0·008		0·01	0·01	0·01	0·00
Ce/Yb	0·65		0·25		0·31		0·54		1·30		0·60		0·54		0·44		0·50		0·59	
Zr/Hf	31·7	2·9	22·6	3·4	24·9	2·8	34·5	7·8	40·2	9·8	27·5	6·6	27·8	2·9	40·5	3·3	34·1	5·2	34·1	8·0
Nb/Ta	10·7						6·8	1·7	3·7	4·7					4·2		6·2		7·6	

(continued)

Table 7: Continued

	Lower Platta unit						Malenco unit										Davos			
	STP-5*		STP-2*		NAP-99-6		Or-UM 224*		Mg-65		LUM-216*		LUM-400*		LUM-112*		To-7*		Totalp-7*	
n:	10	2σ	3	2σ	6	2σ	6	2σ	4	2σ	5	2σ	5	2σ	4	2σ	3	2σ	10	2σ
Li (μg/g)	4·3	1·7	3·2	0·4	2·2	0·2	6·8	1·2	—		0·3	0·1	0·2	0·1	1·1	0·8	—		2·6	0·7
B							1·5	0·7	—		1·6	0·4	1·0	0·4	1·4	0·2	—		—	
Sc	77	6	60	2	58	3	69	3	65	8	71	5	68	2	60	2	65	3	69	6
Ti	5126	462	1578	77	1519	181	3108	79	3944	375	2991	187	1838	48	1529	56	3246	120	3345	205
V	341	18	252	6	243	9	271	7	288	35	274	13	242	4	241	5	275	7	270	8
Cr	5547	442	6248	127	6015	374	6019	364	4907	279	5280	459	6861	308	9283	55	5031	275	4907	454
Co	—		—		—		18·4	1·0	—		16·6	1·1	17·2	0·7	18·8	0·5	—		—	
Ni	—		—		—		300	14	348	18	301	29	306	12	313	6	306	15	—	
Zn	11·49	2·64	—		9·31	1·19	5·90	0·64	10·87	0·21	4·87	0·35	6·12	0·51	6·53	0·28	5·24	0·79	5·83	1·06
Rb	0·04	0·02	<0·022		0·04	0·06	<0·035		0·04		<0·017		<0·018		0·13	0·13	0·10		<0·026	0·03
Sr	6·13	0·71	3·79	0·09	24·07	0·78	76·40	1·35	8·25	1·66	92·52	3·76	32·79	0·91	55·27	0·64	42·46	2·31	39·74	1·43
Y	33·17	2·40	11·20	0·45	11·28	0·65	19·81	0·75	27·20	1·02	18·44	0·27	15·81	0·21	14·54	0·81	20·51	0·23	20·47	0·85
Zr	66·41	6·58	1·08	0·04	5·38	0·70	31·76	0·60	42·91	3·65	28·63	1·70	17·66	0·68	17·19	0·10	22·78	0·45	26·19	1·48
Nb	0·24	0·11	<0·030		1·26	0·25	0·24	0·07	0·80	0·29	0·44	0·21	0·14	0·05	0·13	0·04	0·50	0·03	0·04	0·03
Cs	<0·007		<0·006		<0·006		—		—		—		—		—		—		<0·008	
Ba	0·09	0·06	<0·058		0·54	0·71	0·11	0·12	0·19	0·03	0·09	0·09	0·05	0·06	0·05	0·04	0·05	0·02	0·21	0·10
La	0·90	0·12	<0·002		1·43	0·08	1·16	0·06	—		2·14	0·04	0·48	0·03	0·65	0·05	—		0·49	0·06
Ce	5·15	0·45	0·02	0·01	3·59	0·25	3·81	0·11	4·48	0·14	5·83	0·11	1·64	0·12	2·48	0·05	3·90	0·26	2·41	0·15
Pr	1·15	0·08	0·02	0·01	0·51	0·04	0·68	0·04	0·95	0·05	0·88	0·04	0·33	0·02	0·47	0·03	0·69	0·05	0·56	0·04
Nd	8·05	0·67	0·37	0·01	2·33	0·24	4·21	0·30	5·91	0·18	4·63	0·08	2·24	0·17	2·83	0·32	4·24	0·33	3·80	0·34
Sm	3·45	0·29	0·45	0·03	0·72	0·09	1·74	0·14	2·32	0·12	1·59	0·16	1·10	0·10	1·10	0·21	1·77	0·17	1·70	0·17
Eu	1·14	0·07	0·24	0·01	0·32	0·02	0·72	0·05	0·97	0·07	0·72	0·03	0·51	0·04	0·52	0·02	0·79	0·06	0·75	0·07
Gd	4·89	0·37	1·10	0·07	1·19	0·15	2·49	0·13	3·69	0·32	2·31	0·15	1·85	0·11	1·67	0·10	2·50	0·06	2·63	0·16
Tb	0·93	0·07	0·25	0·01	0·27	0·03	0·52	0·03	0·76	0·06	0·46	0·04	0·38	0·02	0·33	0·01	0·53	0·01	0·53	0·02
Dy	6·30	0·55	2·03	0·11	2·01	0·20	3·55	0·12	4·83	0·23	3·26	0·10	2·77	0·08	2·36	0·08	3·60	0·09	3·74	0·21
Ho	1·34	0·10	0·45	0·01	0·45	0·03	0·81	0·03	1·06	0·02	0·72	0·05	0·61	0·03	0·56	0·04	0·80	0·01	0·82	0·06
Er	3·58	0·36	1·30	0·06	1·31	0·14	2·17	0·11	2·78	0·07	2·08	0·22	1·69	0·08	1·48	0·17	2·18	0·09	2·26	0·13
Tm	0·50	0·06	0·19	0·01	0·19	0·02	0·32	0·02	0·40	0·01	0·30	0·03	0·26	0·02	0·23	0·01	0·32	0·01	0·34	0·02
Yb	3·19	0·22	1·38	0·09	1·24	0·10	2·21	0·15	2·95	0·37	2·07	0·22	1·71	0·13	1·62	0·09	2·26	0·05	2·28	0·18
Lu	0·41	0·03	0·19	0·01	0·17	0·02	0·32	0·03	0·37	0·03	0·28	0·02	0·25	0·02	0·20	0·02	0·30	0·01	0·33	0·02
Hf	2·03	0·36	0·18	0·02	0·28	0·05	0·94	0·10	1·18	0·18	0·82	0·03	0·65	0·05	0·54	0·03	0·78	0·04	1·03	0·12
Ta	0·02	0·01	<0·008		0·13	0·02	0·02	0·00	0·03	0·00	0·08	0·01	0·01	0·00	0·02	0·00	0·06	0·01	<0·012	0·00
Th	0·04	0·01	<0·007		0·13	0·01	0·04	0·02	0·14	0·01	0·06	0·01	0·01	0·00	0·01	0·00	0·08	0·00	<0·009	0·01
U	0·01	0·01	<0·006		0·03	0·02	0·02	0·01	0·02	0·01	0·03	0·01	0·01	0·00	0·01	0·00	0·03	0·00	<0·007	0·00
Ce/Yb	0·44		0·003		0·80		0·47		0·42		0·78		0·26		0·42		0·48		0·29	
Zr/Hf	32·8	11·1	5·9	1·1	19·4		33·8	4·5	36·3	10·2	22·4	2·9	27·4	3·5	32·1	2·1	29·3	2·3	25·5	5·0
Nb/Ta	9·9				9·7		15·1		31·3				10·3		7·8			3·8		

*Parts of trace element data from Müntener *et al.* (2004).

Table 8: Trace element composition of orthopyroxene

	FAP-6		MSP-1		SUP-2		LUM-216		LUM-400		LUM-112		To-7		Totalp-7	
n:	2	2σ	3	2σ	6	2σ	5	2σ	5	2σ	4	2σ	6	2σ	4	2σ
Li (ppm)	—		3·1	0·1	1·7	0·6	1·0	0·5	0·3	0·1	0·6	0·2	—		2·2	1·0
B	—		—				1·0	0·4	0·8	0·1	1·3	0·4	—		—	
Sc	61	15	51	4	35	3	12·0	0·9	15·9	0·6	16·2	0·5	15	1	11	1
Ti	1209	369	1526	78	1465	47	578	17	443	17	436	5	664	35	500	47
V	167	15	226	38	155	14	81	3	89	3	93	3	100	3	69	6
Cr	1890	40	5044		4174		2141	130	2790	108	3683	198	2050	168	1630	221
Co	—		—		—		49·3	2·1	50·7	2·8	57·6	5·3	—		—	
Ni	689	30	—		—		608	18	648	26	722	56	685	54	—	
Zn	11·5	2·6	11·5	2·6	—		21	2	25	2	31	2	24	2	17	2
Rb	0·071	0·004	<0·029		<0·035		<0·021		<0·013		0·028	0·007	0·054	0·032	<0·04	
Sr	0·30	0·04	0·17	0·10	0·18	0·08	0·33	0·25	0·06	0·04	0·25	0·19	0·40	0·10	0·44	0·10
Y	4·5	0·5	2·8	0·1	2·7	0·21	0·62	0·06	0·66	0·03	1·0	0·5	0·77	0·09	0·64	0·04
Zr	7·9	2·1	2·9	0·1	4·67	0·53	0·75	0·14	0·62	0·07	0·75	0·27	0·91	0·15	0·82	0·05
Nb	<0·2		<0·22		<0·044		0·014	0·011	0·011	0·002	0·017	0·011	0·011	0·005	<0·04	
Cs	—		<0·01		<0·01		—						—		0·03	0·01
Ba	0·160	0·100	<0·12		<0·10		0·098	0·083	0·027	0·021	0·055	0·030	0·048	0·014	0·105	0·012
La	<0·006		<0·01		<0·013		0·013	0·005	<0·005		0·010	0·004	—		0·008	0·003
Ce	0·019	0·008	0·065	0·035	0·047	0·027	0·029	0·019	0·005	0·002	0·028	0·008	0·021	0·007	0·014	0·003
Pr	<0·005		<0·013		0·017	0·001	0·006	0·004	0·003	0·001	0·007	0·002	0·005	0·001	<0·006	
Nd	0·055	0·033	0·122	0·001	0·093	0·029	0·026	0·011	0·012	0·003	0·036	0·024	0·028	0·005	0·044	0·010
Sm	0·036	0·022	0·097	0·051	0·071	0·012	0·020	0·006	0·015	0·010	0·021	0·006	0·023	0·011	0·024	0·004
Eu	0·019	0·016	0·031	0·004	0·025	0·009	0·008	0·001	0·006	0·003	0·012	0·003	0·011	0·003	0·010	0·000
Gd	0·094	0·010	0·156	0·031	0·131	0·047	0·026	0·014	0·025	0·010	0·034	0·012	0·037	0·009	0·038	0·011
Tb	0·034	0·014	0·047	0·021	0·035	0·009	0·008	0·002	0·007	0·002	0·009	0·003	0·009	0·003	0·012	0·003
Dy	0·464	0·166	0·366	0·061	0·325	0·051	0·078	0·032	0·075	0·018	0·074	0·021	0·087	0·021	0·091	0·011
Ho	0·154	0·034	0·123	0·031	0·105	0·022	0·025	0·003	0·027	0·006	0·029	0·005	0·028	0·004	0·026	0·004
Er	0·666	0·054	0·461	0·043	0·362	0·056	0·075	0·018	0·087	0·021	0·102	0·015	0·111	0·023	0·100	0·024
Tm	0·140	0·013	0·070	0·024	0·063	0·013	0·019	0·003	0·024	0·004	0·022	0·006	0·022	0·004	0·023	0·006
Yb	1·224	0·423	0·600	0·220	0·521	0·112	0·196	0·030	0·205	0·028	0·186	0·043	0·237	0·019	0·195	0·051
Lu	0·217	0·018	0·113	0·004	0·095	0·021	0·037	0·005	0·038	0·004	0·036	0·004	0·043	0·004	0·031	0·009
Hf	0·190	0·054	0·130	0·014	0·173	0·052	0·032	0·001	0·031	0·005	0·028	0·005	0·042	0·008	0·040	0·009
Ta	<0·006		<0·02		<0·02		<0·004		<0·002		<0·003		<0·003	0·001	<0·003	
Th	<0·005		<0·012		<0·013		0·006	0·001	<0·002		0·005	0·003	<0·003	—	<0·003	
U	<0·003		<0·008		<0·009		<0·003		<0·002		0·006	0·001	0·002	0·001	<0·002	
Ce_N/Yb_N	0·004		0·030		0·025		0·040		0·007		0·041		0·025		0·020	
Zr/Hf	41·4	11·1	22·5	11·1	27·0	1·1	23·3	5·8	20·0	6·3	27·4	18·4	21·7	9·8	20·5	7·3
Nb/Ta																

Table 9: Trace element compositions of Ti-pargasite

	Lower Platta unit			Malenco unit					Totalp		
	FAP-6	SUP-2		LUM-216		LUM-400		LUM-112	To-7		Totalp-7
n:	1	3	2σ	5	2σ	5	2σ	1	3	2σ	1
Li (ppm)	—	5·8	1·4	0·8	0·7	0·3	0·1	0·3	—		—
B	—	—		4·7	1·1	3·6	1·0	<1·79	—		—
Sc	283	152	5·53	76	10	92	19	98	72	8	73
Ti	32418	21057	1560	22502	2171	8219	2172	11175	17595	2372	19920
V	1023	902	70	603	47	482	35	578	537	51	579
Cr	5375	11941	1173	7231	1362	7933	1398	8783	5276	653	6292
Co	—	—		38·6	3·0	32·1	2·2	34·0			—
Ni	682	—		949	70	719	149	856	837·2	24·1	—
Zn	11·1	—		8·6	1·9	7·8	2·4	6·6	8·4	0·4	13·6
Rb	1·984	<0·151		<0·131		0·13	0·03	0·123	5·5	2·5	4
Sr	42·2	30·5	4·3	228	22	56	23	104	118	7	143
Y	120·0	58·4	5·3	34·3	4·1	27·1	0·6	24·1	34·8	0·6	43·1
Zr	149·2	81·1	4·7	40·1	6·8	23·5	5·0	20·2	29·7	0·2	34·8
Nb	32·68	6·88	1·00	22·9	2·8	4·2	0·5	4·9	26·5	4·3	3·2
Cs	—	0·21	0·06								
Ba	36·36	0·91	0·17	3·15	4·03	2·65	1·18	1·56	153·55	62·72	27·96
La	—	1·62	0·18	3·26	0·40	0·81	0·07	0·95	—		0·93
Ce	8·12	9·32	0·70	9·39	0·58	2·63	0·15	3·64	6·57	0·22	4·66
Pr	1·99	1·88	0·19	1·39	0·11	0·56	0·07	0·65	1·16	0·02	0·99
Nd	12·03	11·32	0·76	7·66	0·46	3·98	0·46	3·55	6·77	0·06	6·27
Sm	6·41	5·13	0·40	2·93	0·56	1·64	0·30	1·53	2·90	0·01	3·12
Eu	1·54	1·82	0·14	1·29	0·29	0·84	0·08	0·58	1·20	0·06	1·61
Gd	11·25	7·74	1·58	4·58	0·58	2·96	0·74	2·10	4·32	0·39	4·61
Tb	2·81	1·43	0·16	0·82	0·10	0·62	0·09	0·47	0·85	0·06	0·96
Dy	19·75	11·18	1·30	5·86	0·66	4·89	0·15	3·82	5·96	0·32	7·90
Ho	4·77	2·17	0·15	1·30	0·12	1·02	0·06	0·81	1·35	0·00	1·47
Er	14·17	6·93	0·83	3·57	0·79	2·98	0·35	2·25	3·72	0·27	4·24
Tm	1·84	0·80	0·08	0·57	0·11	0·43	0·03	0·34	0·57	0·04	0·63
Yb	12·68	5·37	0·55	4·15	0·89	3·09	0·47	2·81	3·70	0·08	4·85
Lu	1·58	0·74	0·07	0·58	0·12	0·43	0·04	0·38	0·50	0·02	0·68
Hf	4·669	2·605	0·130	1·089	0·412	0·747	0·162	0·533	1·147	0·120	1·570
Ta	1·315	0·291	0·030	0·922	0·224	0·091	0·051	0·112	0·654	0·076	0·080
Th	0·069	<0·002		0·036	0·040	<0·002		<0·002	0·057	0·040	0·010
U	0·019	<0·006		0·019	0·010	0·004		<0·006	0·024	0·006	<0·002
Ce_N/Yb_N	0·18	0·48		0·63		0·23		0·36	0·49		0·27
Zr/Hf	32·0	31·1	3·5	36·9	2·9	31·5	3·5	37·9	25·9	2·3	22·2
Nb/Zr	0·22	0·08		0·57		0·18		0·24	0·89		0·09
Nb/Ta	24·85	23·66		24·89		46·36		43·72	40·52	0·00	39·63
Nb/La		4·236		7·026		5·168		5·182			3·409
Mg-no.	0·874	0·876		0·926		0·926		0·899	0·915		0·915

Table 10: Bulk-rock major and trace element compositions of the Platta ultramafic rocks

	Upper Platta						Lower Platta											
	VEP2	VEP7	VEP8	FAP3-I	FAP4	NAP99-7	NAP99-3	LAP1	NAP99-2	SUP2	SUP3	SUP4	SUP5	STP1	STP2	STP3	MSP1	CRP1	CRP3
SiO_2	45·71	45·58	44·26	42·10	43·72	44·06	43·53	43·20	44·27	44·73	44·53	44·22	44·15	43·96	44·53	44·12	43·94	46·27	44·81
TiO_2	0·09	0·19	0·09	0·16	0·25	0·19	0·00	0·16	0·13	0·14	0·11	0·15	0·16	0·17	0·00	0·09	0·09	0·00	0·17
Al_2O_3	3·49	6·06	2·84	4·56	4·71	4·20	2·10	3·86	3·82	3·90	3·62	3·88	3·93	3·75	2·38	3·01	3·45	1·24	4·45
FeO	8·22	6·96	8·32	9·10	9·02	8·56	8·47	10·06	8·79	8·25	8·53	8·62	8·76	9·00	8·05	9·52	8·67	7·91	7·86
MnO	0·16	0·14	0·12	0·14	0·13	0·13	0·09	0·18	0·16	0·13	0·15	0·12	0·12	0·19	0·16	0·17	0·12	0·08	0·13
MgO	35·46	33·19	40·50	42·08	36·36	37·60	44·03	38·23	37·44	38·52	39·20	39·10	38·37	37·96	40·83	39·69	39·04	42·65	35·85
CaO	4·94	6·12	2·06	0·00	3·88	3·46	0·00	2·37	3·61	2·62	2·07	2·12	2·60	3·06	2·25	1·48	3·01	0·00	5·00
Na_2O	0·11	0·16	0·08	0·00	0·11	0·00	0·00	0·00	0·00	0·00	0·00	0·00	0·07	0·00	0·00	0·00	0·00	0·00	0·06
K_2O	0·00	0·00	0·00	0·00	0·00	0·00	0·00	0·00	0·00	0·00	0·00	0·00	0·00	0·00	0·00	0·00	0·00	0·00	0·00
P_2O_5	0·15	0·12	0·09	0·12	0·11	0·13	0·09	0·10	0·11	0·11	0·12	0·10	0·12	0·13	0·11	0·09	0·11	0·09	0·11
Cr_2O_3	0·48	0·49	0·44	0·46	0·44	0·45	0·46	0·45	0·41	0·41	0·44	0·44	0·47	0·49	0·49	0·48	0·37	0·55	0·46
NiO	0·29	0·22	0·27	0·27	0·27	0·27	0·30	0·28	0·27	0·25	0·27	0·29	0·28	0·28	0·31	0·29	0·24	0·33	0·24
LOI	11·68	8·56	12·35	12·82	10·98	11·37	13·06	11·73	11·21	11·37	12·41	11·85	11·32	11·67	12·25	12·1	10·94	12·31	10·43
Mg-no.	0·885	0·895	0·897	0·892	0·878	0·887	0·903	0·871	0·884	0·893	0·891	0·890	0·886	0·883	0·900	0·881	0·889	0·906	0·890
Trace elements (μg/g)																			
V	68	143	65	92	121	88	52	79	74	74	72	75	77	84	71	66	76	36	90
Cr	2904	3104	2663	2773	2697	2764	2734	2773	2537	2491	2650	2660	2866	2970	2985	2890	2288	3317	2849
Ni	1996	1572	1904	1859	1877	1896	2044	1961	1910	1797	1878	2009	1940	1995	2154	2056	1708	2295	1713
Co	105	76	100	103	102	101	109	102	101	97	99	104	104	105	111	91	96	114	93
Cu	20	75	21	22	40	15	16	28	25	21	26	24	15	18	6	15	8	b.d.	37
Zn	59	46	66	37	73	54	30	50	53	49	94	54	49	107	48	70	31	59	39
ICP-MS																			
Rb 85	1·022	b.d.	b.d.	b.d.	b.d.	b.d.	b.d.	b.d.	b.d.	1·122	1·104	b.d.	b.d.	b.d.	b.d.	1·042	b.d.	b.d.	2·704
Sr 86	24·971	11·414	9·286	b.d.	8·329	b.d.	b.d.	b.d.	4·547	9·444	5·977	4·853	5·886	b.d.	b.d.	8·219	b.d.	b.d.	7·811
Y 89	2·630	3·203	1·576	4·525	7·548	4·094	0·737	3·628	3·210	3·309	2·968	3·135	3·314	3·793	1·386	2·424	1·728	0·126	4·162
Zr 90	2·834	5·549	2·242	6·043	7·517	8·567	b.d.	7·360	5·963	6·694	4·842	5·992	6·555	7·156	b.d.	3·725	2·001	b.d.	6·968
Cs 133	4·452	1·810	0·992	0·292	0·749	b.d.	b.d.	0·276	1·235	1·163	0·292	1·312	0·779	0·256	b.d.	1·422	0·233	0·208	2·424
Ba 137	5·173	3·346	b.d.	b.d.	b.d.	b.d.	b.d.	b.d.	b.d.	b.d.	b.d.	b.d.	b.d.	b.d.	b.d.	b.d.	b.d.	b.d.	b.d.
La 139	0·033	0·264	0·058	0·191	0·131	0·197	0·078	0·188	0·144	0·151	0·234	0·128	0·179	0·164	0·050	0·093	0·060	0·020	0·151
Ce 140	0·191	0·860	0·303	0·713	0·653	0·675	0·176	0·736	0·545	0·523	0·507	0·550	0·809	0·659	0·102	0·376	0·266	0·023	0·634
Pr 141	0·049	0·164	0·072	0·151	0·168	0·158	0·024	0·132	0·125	0·108	0·103	0·102	0·134	0·123	0·013	0·071	0·046	0·004	0·136
Nd 145	0·344	0·963	0·395	0·979	0·935	0·951	0·094	0·830	0·545	0·625	0·587	0·618	0·778	0·802	0·063	0·401	0·246	0·025	0·831
Sm 147	0·172	0·365	0·152	0·382	0·460	0·281	0·025	0·252	0·298	0·263	0·234	0·234	0·232	0·359	0·040	0·167	0·123	0·008	0·291
Eu 151	0·078	0·195	0·062	0·061	0·200	0·199	0·054	0·108	0·115	0·131	0·113	0·133	0·124	0·147	0·018	0·093	0·055	b.d.	0·144
Gd 157	0·301	0·411	0·194	0·570	0·800	0·587	0·040	0·381	0·462	0·407	0·361	0·387	0·424	0·480	0·075	0·255	0·209	b.d.	0·456
Tb 159	0·053	0·079	0·039	0·106	0·148	0·090	0·010	0·079	0·064	0·068	0·064	0·068	0·078	0·072	0·020	0·047	0·032	0·002	0·084
Dy 161	0·371	0·586	0·266	0·677	1·120	0·718	0·092	0·528	0·490	0·475	0·458	0·499	0·505	0·636	0·186	0·352	0·280	0·014	0·574
Ho 165	0·089	0·119	0·055	0·158	0·245	0·138	0·026	0·125	0·112	0·105	0·106	0·115	0·115	0·125	0·050	0·089	0·061	0·004	0·144
Er 166	0·237	0·356	0·145	0·436	0·698	0·388	0·076	0·340	0·311	0·314	0·268	0·342	0·308	0·393	0·136	0·253	0·188	0·015	0·396
Tm 169	0·037	0·057	0·026	0·062	0·117	0·058	0·014	0·060	0·051	0·054	0·049	0·058	0·054	0·068	0·023	0·041	0·028	0·003	0·069
Yb 174	0·266	0·385	0·150	0·442	0·803	0·432	0·111	0·349	0·309	0·325	0·300	0·356	0·369	0·422	0·176	0·283	0·160	0·025	0·433
Lu 175	0·036	0·061	0·025	0·071	0·110	0·070	0·019	0·061	0·051	0·063	0·057	0·067	0·051	0·062	0·029	0·043	0·028	0·005	0·063
Hf 180	0·068	0·141	0·082	0·192	0·261	0·212	b.d.	0·205	0·174	0·202	0·152	0·168	0·199	0·228	b.d.	0·118	0·051	b.d.	0·215
Th 232	0·0000	0·0079	0·0012	0·0066	0·0045	0·0016	0·0021	0·0043	0·0028	0·0031	0·0153	0·0012	0·0050	0·0077	0·0069	0·0111	0·0066	0·0000	0·0011
U 238	0·1159	0·0046	0·0036	0·0043	0·0083	0·0000	0·0000	0·0054	0·0000	0·0028	0·0105	0·0011	0·0000	0·0083	0·0056	0·0082	0·0071	0·0524	0·0000

b.d., below detection limit.

Table 11: Bulk-rock major and trace element compositions of the Malenco ultramafic rocks

	Peridotite and serpentinized peridotite												
	L-UM112	L-UM216	L-UM217	L-UM226	L-UM228	Or-UM 201	Or-UM 234	Or-UM235	Or-UM236	L-UM109	L-UM111	LUM400	OrUM309h
SiO_2	43·84	44·19	44·00	44·28	44·18	44·57	43·99	43·73	44·25	44·11	43·97	44·18	43·90
TiO_2	0·04	0·14	0·04	0·03	0·06	0·09	0·06	0·05	0·05	0·04	0·04	0·05	0·07
Al_2O_3	1·49	3·14	1·96	1·27	2·14	2·96	2·55	1·99	2·10	1·84	1·87	2·29	1·09
FeO	8·08	8·13	7·91	7·96	7·83	8·11	8·50	8·09	7·82	8·03	8·59	7·84	9·09
MnO	0·11	0·12	0·13	0·12	0·12	0·12	0·14	0·13	0·12	0·14	0·14	0·12	0·14
MgO	44·34	41·08	43·39	44·55	42·93	41·08	42·00	43·40	43·29	43·42	43·11	42·97	44·67
CaO	1·40	2·50	1·82	1·04	1·97	2·35	2·05	1·82	1·68	1·71	1·62	1·73	0·39
Na_2O	<0·04	<0·04	<0·04	<0·04	<0·04	<0·04	<0·04	0·08	<0·04	<0·04	<0·04	0·05	<0·04
K_2O	<0·02	<0·02	<0·02	<0·02	<0·02	<0·02	<0·02	<0·02	<0·02	<0·02	<0·02	<0·02	<0·02
P_2O_5	0·01	0·02	0·01	0·01	0·01	0·01	0·01	0·01	<0·01	<0·01	0·01	0·01	0·03
Cr_2O_3	0·31	0·35	0·38	0·36	0·39	0·37	0·37	0·34	0·34	0·34	0·31	0·39	0·22
NiO	0·37	0·32	0·37	0·36	0·35	0·34	0·33	0·36	0·35	0·37	0·35	0·36	0·38
LOI	1·74	1·74	2·36	7·54	1·68	6·11	5·46	2·67	4·50	3·16	3·35	0·52	6·06
Mg-no.	0·907	0·900	0·907	0·909	0·907	0·900	0·898	0·905	0·908	0·906	0·899	0·907	0·897
Trace elements (μg/g)													
XRF													
V	44	64	55	30	51	54	49	52	47	46	45	53	38
Cr	2377	2712	2928	2387	2960	2662	2634	2657	2501	2479	2180	2682	1471
Ni	2257	2008	2160	2071	2131	1893	1974	2118	2080	2087	2014	2205	2098
Co	105	98	90	86	99	84	97	100	97	96	98	134	129
Cu	<1	4	<1	<1	<1	4	1	<1	<1	<1	<1	18	17
Zn	35	43	39	40	41	41	44	40	41	45	48	47	49
Sc	10	12	12	6	11	9	9	12	8	10	8	9	5
S	<50	<50	<50	<50	<50	<50	<50	<50	<50	<50	<50	<50	457
ICP-MS	*1*	*1*	*2*	*2*	*2*	*2*	*2*	*2*	*2*	*2*	*2*	*1*	*2*
Rb 85	0·138	0·121	0·152	0·201	0·198	0·237	0·013	0·478	0·265	0·415	0·894	0·047	0·225
Sr 88	3·034	10·749	4·226	3·426	4·296	8·370	6·680	3·636	3·336	5·740	6·097	2·519	2·135
Y 89	0·944	2·496	0·918	0·337	1·114	2·380	1·900	0·994	0·945	1·355	1·203	1·181	0·583
Zr 90	1·311	4·836	0·557	0·480	1·208			1·028	1·078	1·478	1·098	1·417	0·547
Nb 93	0·028	0·173	0·000	0·025	0·012		<0·005	0·014	0·007	<0·005		0·026	
Cs 133	0·007	0·007	—	—	—	—	—	—	—	—	—	0·003	—
Ba 138	0·476	1·588	0·142	0·231	0·346			0·192	0·199			0·216	0·276
La 139	0·047	0·264	0·044	0·064	0·059	0·077	0·086	0·098	0·078	0·055	0·125	0·034	0·105
Ce 140	0·153	0·828	0·155	0·178	0·221	0·304	0·286	0·294	0·222	0·276	0·380	0·112	0·367
Pr 141	0·032	0·134	0·027	0·027	0·038	0·057	0·055	0·041	0·032	0·049	0·055	0·025	0·060
Nd 146	0·176	0·721	0·137	0·129	0·203	0·389	0·332	0·187	0·154	0·286	0·286	0·164	0·357
Sm 149	0·069	0·232	0·053	0·043	0·073	0·153	0·147	0·065	0·058	0·108	0·081	0·070	0·094
Eu 151	0·028	0·097	0·020	0·023	0·032	0·068	0·068	0·033	0·025	0·034	0·056	0·033	0·009
Gd 157	0·113	0·359	0·082	0·049	0·120	0·242	0·215	0·106	0·095	0·150	0·169	0·143	0·099
Tb 159	0·022	0·067	0·018	0·008	0·023	0·051	0·043	0·020	0·019	0·032	0·030	0·027	0·015
Dy 163	0·160	0·454	0·164	0·057	0·204	0·373	0·314	0·176	0·164	0·227	0·211	0·207	0·103
Ho 165	0·037	0·104	0·040	0·013	0·047	0·088	0·076	0·042	0·040	0·055	0·050	0·048	0·023
Er 167	0·120	0·308	0·107	0·040	0·126	0·256	0·219	0·120	0·108	0·166	0·146	0·153	0·063
Tm 169	0·019	0·046	0·017	0·007	0·020	0·039	0·035	0·018	0·018	0·026	0·024	0·023	0·010
Yb 174	0·125	0·304	0·096	0·077	0·121	0·254	0·214	0·101	0·095	0·135	0·134	0·155	0·056
Lu 175	0·022	0·051	0·018	0·008	0·021	0·036	0·034	0·019	0·020	0·024	0·025	0·028	0·011
Hf 178	0·046	0·175			0·013	0·112	0·071				0·043	0·059	0·020
Ta 181	0·005	0·019										0·002	
Pb 208	0·045	0·054	—	—	—	—	—	—	—	—	—	0·037	—
Th 232	0·004	0·012				0·035	0·036					0·001	0·003
U 238	0·001	0·004		0·001		0·010	0·010	0·002		0·001	0·001	0·001	0·001

(continued)

Table 11: Continued

	Serpentinite														
	B-UM201	PUM16	BUM320	P-UM1	P-UM16	P-UM18	P-UM24	P-UM116	P-UM117a	DUM24	DUM15	C10-5	P7-1	P56-57	P111-111
SiO_2	46·46	44·40	45·37	45·16	44·43	44·33	44·91	44·61	44·95	45·62	45·18	45·14	47·55	46·32	45·54
TiO_2	0·12	0·15	0·12	0·12	0·15	0·13	0·10	0·10	0·14	0·10	0·14	0·05	0·03	0·05	0·03
Al_2O_3	3·57	4·04	3·68	3·58	3·83	3·41	2·88	3·18	2·36	3·07	3·18	4·10	1·53	1·71	2·19
FeO	8·02	8·62	7·67	7·92	8·66	8·69	7·46	8·85	8·67	8·29	8·03	8·75	7·18	7·30	9·22
MnO	0·15	0·18	0·11	0·12	0·18	0·15	0·12	0·15	0·09	0·09	0·14	0·15	0·15	0·10	0·13
MgO	38·40	37·46	39·65	39·13	37·68	39·93	41·32	39·00	40·88	40·94	41·01	39·78	42·95	43·02	42·15
CaO	2·58	4·48	2·71	3·30	4·38	2·64	2·57	3·39	2·27	1·23	1·66	1·30	0·00	0·89	0·00
Na_2O	<0·04	<0·04	<0·04	<0·04	<0·04	<0·04	<0·04	<0·04	<0·04	<0·04	<0·04	<0·04	<0·04	<0·04	<0·04
K_2O	<0·02	<0·02	<0·02	<0·02	<0·02	<0·02	<0·02	<0·02	<0·02	<0·02	<0·02	<0·02	<0·02	<0·02	<0·02
P_2O_5	0·01	0·02	0·02	0·02	0·02	0·03	0·01	0·00	0·01	0·02	0·03	0·01	0·01	0·00	0·01
Cr_2O_3	0·35	0·35	0·34	0·34	0·37	0·36	0·30	0·40	0·30	0·30	0·29	0·42	0·34	0·34	0·43
NiO	0·33	0·29	0·32	0·31	0·30	0·33	0·32	0·31	0·32	0·34	0·34	0·30	0·26	0·26	0·31
LOI	10·28	8·46	9·86	8·43	8·46	6·26	9·16	8·71	8·98	11·08	9·16	10·56	11·52	11·97	12·21
Mg-no.	0·895	0·886	0·902	0·898	0·886	0·891	0·908	0·887	0·894	0·898	0·901	0·890	0·914	0·913	0·891
Trace elements (μg/g)															
XRF															
V	49	82	73	68	69	57	59	61	51	60	51	75	26	37	44
Cr	2359	2676	2469	2337	2509	2518	1953	2677	1905	1869	1959	2659	2067	2091	2501
Ni	1812	1721	1814	1761	1537	1794	1690	1709	1732	1926	1788	1875	1441	1469	1852
Co	67	89	84	76	63	81	55	52	49	50	67	73	47	20	63
Cu	0	32	29	<4	11	10	<4	<4	<4	5	14	47	13	16	10
Zn	59	61	57	41	44	48	41	46	41	39	43	58	58	41	52
Sc	9	14	14	10	11	10	12	10	10	10	8	14	8	11	9
S	<50	549	<50	<50	392	<50	<50	<50	<50	<50	<50	<50	<50	16	0
ICP-MS	*2*		*1*	*1*				*2*	*2*	*2,4*	*2,4*	*3*	*3*	*3*	*3*
Rb 85	0·224	—	0·042	0·056	—	—	—	0·125	0·182	0·145	0·211	—	—	—	—
Sr 88	5·256	—	3·080	5·683	—	—	—	1·430	2·396	2·900	6·602	—	—	—	—
Y 89	1·214	—	2·057	2·026	—	—	—	2·860	1·470	4·288	3·659	—	—	—	—
Zr 90	2·348	—	2·827	3·523	—	—	—		2·289	43·880	22·980	—	—	—	—
Nb 93	0·098	—	0·104	0·045	—	—	—					—	—	—	—
Cs 133	—	—	0·001	0·007	—	—	—	—	—	—	—	—	—	—	—
Ba 138	0·349	—	0·098	0·287	—	—	—					—	—	—	—
La 139	0·107	—	0·104	0·141	—	—	—	0·075	0·088	0·106	0·159	—	—	—	—
Ce 140	0·332	—	0·364	0·504	—	—	—	0·225	0·308	0·159	0·397	—	—	—	—
Pr 141	0·056	—	0·072	0·089	—	—	—	0·057	0·065	0·036	0·078	—	—	—	—
Nd 146	0·256	—	0·449	0·520	—	—	—	0·409	0·398	0·276	0·464	—	—	—	—
Sm 149	0·089	—	0·181	0·175	—	—	—	0·176	0·153	0·114	0·207	—	—	—	—
Eu 151	0·040	—	0·074	0·072	—	—	—	0·072	0·046	0·060	0·089	—	—	—	—
Gd 157	0·160	—	0·279	0·269	—	—	—	0·285	0·223	0·171	0·269	—	—	—	—
Tb 159	0·027	—	0·053	0·048	—	—	—	0·052	0·038	0·031	0·052	—	—	—	—
Dy 163	0·219	—	0·379	0·338	—	—	—	0·373	0·264	0·213	0·365	—	—	—	—
Ho 165	0·047	—	0·086	0·076	—	—	—	0·088	0·058	0·051	0·084	—	—	—	—
Er 167	0·122	—	0·265	0·234	—	—	—	0·258	0·155	0·160	0·248	—	—	—	—
Tm 169	0·020	—	0·039	0·037	—	—	—	0·040	0·023	0·025	0·038	—	—	—	—
Yb 174	0·136	—	0·262	0·250	—	—	—	0·271	0·128	0·169	0·268	—	—	—	—
Lu 175	0·020	—	0·046	0·044	—	—	—	0·043	0·020	0·031	0·043	—	—	—	—
Hf 178	0·038	—	0·101	0·131	—	—	—	0·170	0·108	0·843	0·474	—	—	—	—
Ta 181		—	0·005	0·004	—	—	—					—	—	—	—
Pb 208	—	—	0·196	0·080	—	—	—	—	—	—	—	—	—	—	—
Th 232	0·001	—	0·008	0·007	—	—	—	0·038			0·017	—	—	—	—
U 238	0·004	—	0·006	0·001	—	—	—	0·009		0·001	0·003	—	—	—	—

(continued)

Table 11: Continued

	Serpentinite											
	C19-10	P115-119	P61-63	P60-62	P49-50	P43-41	T88-83	P67-66	C85-81	P73-73	C55-54	P70-69
SiO_2	45·56	46·27	45·35	43·46	44·27	45·23	44·26	47·38	44·30	46·15	42·85	45·15
TiO_2	0·11	0·03	0·09	0·13	0·02	0·03	0·02	0·05	0·08	0·12	0·13	0·14
Al_2O_3	3·63	2·14	2·93	2·77	1·80	2·75	1·39	2·38	2·73	2·66	2·32	3·30
FeO	8·82	7·57	8·72	9·40	8·30	8·18	8·26	7·29	8·20	8·01	8·18	8·52
MnO	0·10	0·13	0·14	0·13	0·16	0·11	0·12	0·10	0·14	0·10	0·16	0·14
MgO	40·30	43·22	41·95	40·92	44·09	40·52	45·06	41·32	41·11	40·77	45·48	38·20
CaO	0·74	0·00	0·08	2·51	0·53	2·37	0·01	0·82	2·71	1·50	0·31	3·37
Na_2O	<0·04	<0·04	<0·04	<0·04	<0·04	<0·04	<0·04	<0·04	<0·04	<0·04	<0·04	<0·04
K_2O	<0·02	<0·02	<0·02	<0·02	<0·02	<0·02	<0·02	<0·02	0·07	<0·02	<0·02	0·44
P_2O_5	0·01	0·01	0·01	0·00	0·00	0·00	0·01	0·00	0·01	0·01	0·01	0·02
Cr_2O_3	0·40	0·39	0·38	0·37	0·45	0·42	0·44	0·32	0·33	0·37	0·29	0·42
NiO	0·33	0·24	0·35	0·32	0·38	0·37	0·42	0·35	0·32	0·32	0·29	0·30
LOI	10·76	11·57	11·52	13·40	10·38	11·93	4·62	7·15	6·92	4·76	5·33	3·57
Mg-no.	0·891	0·910	0·895	0·886	0·904	0·898	0·907	0·910	0·899	0·901	0·908	0·889
Trace elements (μg/g)												
XRF	*3*	*3*	*3*	*3*	*3*	*3*	*3*	*3*	*3*	*3*	*3*	*3*
V	65	35	50	49	27	37	42	41	46	61	33	79
Cr	2514	2268	2217	2265	2680	2491	3142	1329	2336	2683	1962	3092
Ni	1954	1318	1944	1603	1827	1989	2407	2084	1822	1923	1654	1847
Co	74	19	65	87	58	63	105	94	98	80	105	97
Cu	7	14	9	20	18	6	14	17	12	13	9	13
Zn	46	51	54	40	49	40	49	53	48	48	54	49
Sc	14	7	12	13	10	2	10	7	13	13	10	13
S	<50	<50	<50	762	415	<50	124	335	66	<50	<50	418

1, ICP-MS analysis performed at Montpellier, following the procedures described by Ionov *et al*. (1992); *2*, ICP-MS analysis performed at EMPA Dübendorf (Switzerland), following the procedures described by Müntener (1997); *3*, whole-rock XRF analyses from Paglia (1996); *4*, whole-rock analysis from Reber (1995).

Olivine

Primary olivine is preserved only in samples from the Davos and Malenco peridotites, but is completely serpentinized in the Platta samples (except within mylonites). Overall, olivine is forsteritic in composition ($Fo_{87–91}$) and on average lower in forsterite content than abyssal peridotites (Dick, 1989). NiO averages 0·41 wt %, consistent with mantle peridotite. Systematic co-variations of forsterite and NiO contents are not observed.

Amphibole

The amphiboles analyzed are all interstitial grains, in equilibrium with the mantle assemblage as indicated by their high Mg-number (Table 6). They range from kaersutite (Ti > 0·5 p.f.u.) to Ti-rich pargasite. Amphibole associated with phlogopite is significantly higher in K_2O at similar Cr_2O_3. All amphiboles have a LREE-depleted trace element pattern (CeN/YbN: 0·18–0·63) with (Nb/La) > 1 and Nb/Ta ratios exceeding primitive mantle values. Most amphiboles show a weak to positive Sr anomaly and only one sample displays a distinctive negative Sr anomaly (Fig. 9). This latter characteristic is found in samples where spinel has high Cr-number and high TiO_2 contents, indicating that the negative Sr anomalies are caused by equilibration with plagioclase. The strongly variable Rb and Ba contents can probably be explained by equilibration with phlogopite in some cases. Niobium and Ta (Nb/Ta: 24–46) are decoupled from other trace element variations and are not correlated with Sr anomalies or the REE content.

GEOTHERMOMETRY

Equilibrium temperatures for the various peridotites were calculated based on mineral composition data reported in Tables 2, 3, and 5, respectively. For the spinel peridotites, Ca-in-orthopyroxene (Brey & Köhler, 1990), and the Cr–

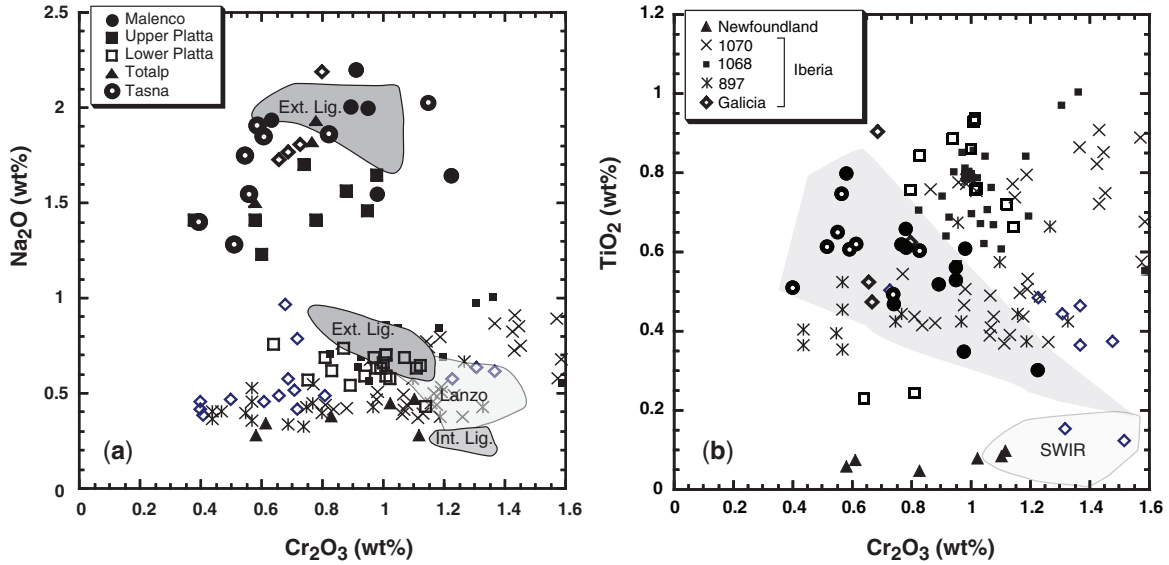

Fig. 4. Clinopyroxene major element compositions from the Malenco, Platta, Totalp and Tasna peridotites, compared with those of the Ligurides, Lanzo (Western Alps) and Iberia–Newfoundland. (a) Na_2O vs Cr_2O_3 (wt %). It should be noted that high-Na clinopyroxene is restricted to 'subcontinental peridotites' and 'metasomatic harzburgites', whereas low-Na clinopyroxenes are found in depleted peridotites and those that equilibrated with plagioclase. (b) TiO_2 vs Cr_2O_3 (wt %). Grey field encompasses clinopyroxene from spinel peridotites. Simple melting models predict decreasing TiO_2 and increasing Cr_2O_3 for clinopyroxene in residual peridotites. Data from South West Indian Ridge (SWIR; Hellebrand *et al.*, 2002) and Newfoundland (Müntener & Manatschal, 2006) represent residues of high degrees of partial melting. Most clinopyroxenes from Iberia do not fall into this field and are enriched in both Cr_2O_3 and TiO_2. Data for Liguria are from Rampone *et al.* (1995, 1996) and Montanini *et al.* (2006); for Lanzo from Boudier (1978), Ernst (1978), Pognante *et al.* (1985) and Kaczmarek & Müntener (2008); for Iberia–Newfoundland from Kornprobst & Tabit (1988), Cornen *et al.* (1996), Hébert *et al.* (2001), Chazot *et al.* (2005) and Müntener & Manatschal (2006).

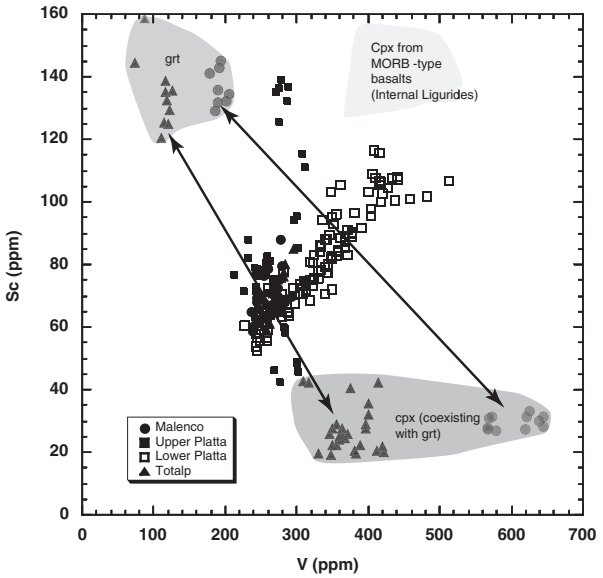

Fig. 5. Sc vs V relationships in clinopyroxenes from the studied peridotites. Clinopyroxenes from plagioclase peridotites show a positive correlation between Sc and V, with the highest values approaching clinopyroxene compositions from N-MORB ophiolites (shaded field: Vannucci *et al.*, 1993*a*). Clinopyroxenes from spinel peridotites are generally lower in both Sc and V. Samples from the upper Platta unit show negative correlations, with both high and low Sc contents. These signatures are probably inherited from cpx related to garnet pyroxenites. Dark shaded fields illustrate Sc–V relationships for clinopyroxene coexisting with garnet from garnet pyroxenites from Totalp and Malenco (O. Müntener, unpublished data).

Al exchange between orthopyroxene and spinel (Caroll Webb & Wood, 1986) were applied, whereas for plagioclase peridotites only Ca-in-orthopyroxene could be used. The Ca-in-orthopyroxene thermometer is based on mutual solubility of the diopside and enstatite molecules in coexisting orthopyroxene and clinopyroxene, and requires an estimate of pressure, as the solvus is weakly pressure dependent (~5°C/0·1 GPa, e.g. Brey *et al.*, 1990). We have chosen a pressure of 1·5 GPa for spinel peridotite and 1·0 GPa for plagioclase peridotite. The Cr–Al exchange between orthopyroxene and spinel requires equilibrium between olivine, Cr–Al spinel and orthopyroxene, and cannot be applied to plagioclase peridotites. The average temperature range for the spinel peridotites is 870–950°C, and the average difference between the thermometers of Brey & Köhler (1990), Caroll Webb & Wood (1986) and Witt-Eickschen & Seck (1991) are about 30°C. This suggests that orthopyroxene, clinopyroxene and spinel approached equilibrium at temperatures close to 920°C. These results are significantly lower than those calculated for the plagioclase peridotites, which vary between 1030 and 1180°C (at 1·0 GPa). Similarly high temperatures were also calculated by applying the T_{Sc} thermometer based on Sc partioning between orthopyroxene and clinopyroxene (Seitz *et al.*, 1999). Although the higher temperatures in the plagioclase peridotites are somewhat uncertain because of the scarcity of preserved

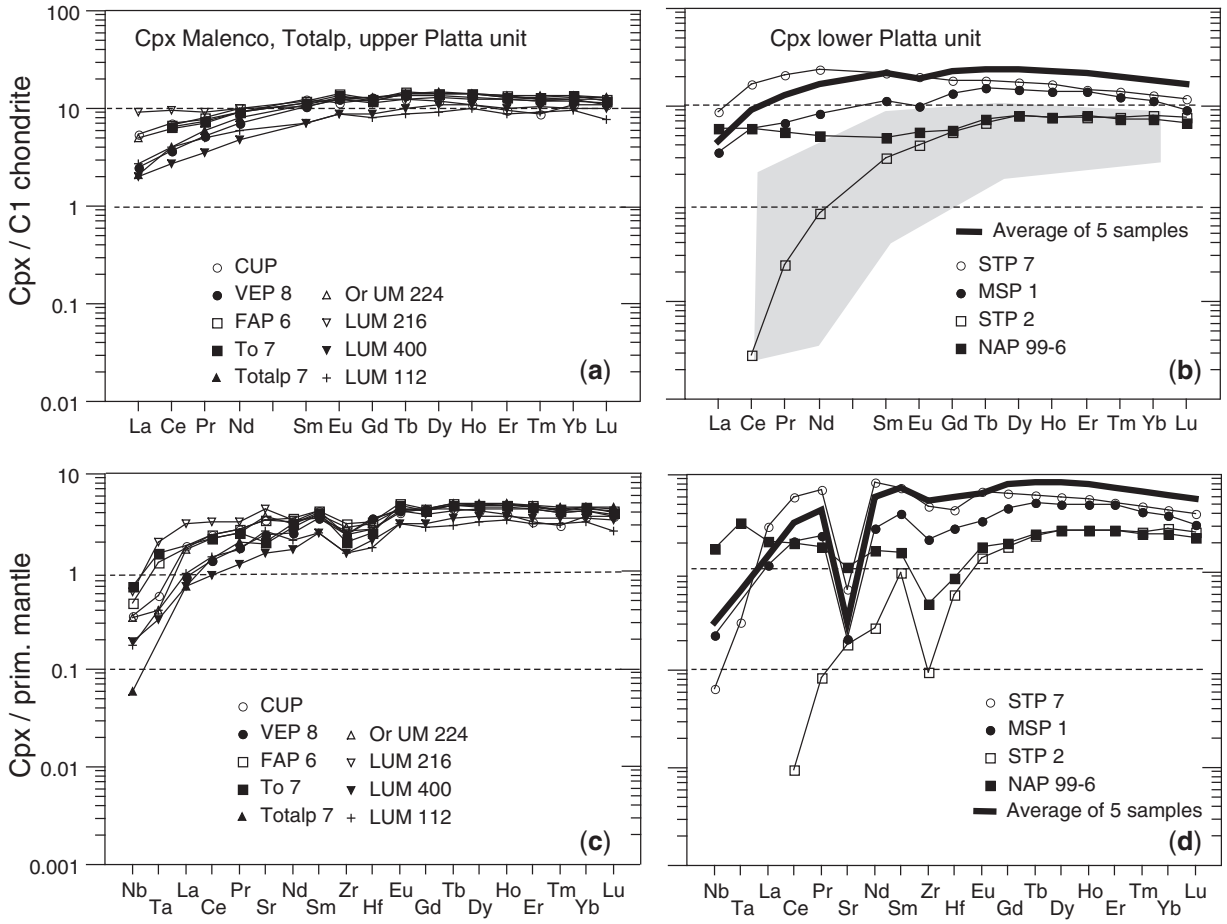

Fig. 6. Trace element compositions of clinopyroxene (cpx) from mantle rocks in the Eastern Central Alps ophiolites determined by LA-ICPMS. (a) Chondrite-normalized REE patterns of clinopyroxenes from spinel peridotites of the Totalp, Malenco and upper Platta peridotites that are exhumed close to the former Adria continental margin. (b) Chondrite-normalized REE patterns of cpx from peridotites from the lower Platta unit. These data show that clinopyroxenes in plagioclase lherzolites have higher MREE, a distinct negative Eu anomaly and REE pattern unlike the clinopyroxenes from the spinel peridotites. Shaded field is from Johnson *et al.* (1990). (c) Primitive mantle normalized clinopyroxene trace element patterns displaying weak negative Zr and Hf anomalies, as expected for clinopyroxene in equilibrium with orthopyroxene. It should be noted that there is no Sr anomaly. (d) Primitive mantle normalized trace element patterns for the lower Platta unit. The fractionation of Zr from Hf with an increasingly fractionated REE pattern should be noted. Sample NAP-99-6 displays elevated Nb–Ta and a LREE-enriched pattern, but very similar MREE to HREE compared with STP-2. Bold line in (b) and (d) is the average of five clinopyroxenes from the lower Platta unit.

orthopyroxene in the samples, trace element partitioning between orthopyroxene and clinopyroxene is qualitatively consistent with the calculations (see below).

BULK-ROCK CHEMISTRY

Figure 10 illustrates the variation of a range of major and trace elements against Mg-number and Al_2O_3 in bulk-rocks. Although dunites from Malenco are not included, major and minor elements in bulk-rocks from both Platta and Malenco display a wide range of variation from refractory (e.g. 45·1 wt % MgO and 1·39 Al_2O_3) to fertile compositions (35·9 wt % MgO and 4·45 Al_2O_3). Some of the samples from the upper Platta unit display even higher Al contents. This feature reflects the presence of millimeter-scale deformed websterite layers that are common in the upper Platta unit (Fig. 3). Calculated Mg-numbers of most peridotites fall within the range of 0·88–0·91. On average, the Malenco rocks are more depleted than the upper Platta rocks. The major and minor element covariation trends, most notably the V, Yb, TiO_2 and Al_2O_3 variations (Fig. 10), are similar to those of mantle peridotite suites worldwide [see, e.g. Bodinier & Godard (2003) and Canil (2004) for a more complete compilation of literature data] and seem, at first glance, compatible with the interpretation of variable degrees of melting.

Similar to the majority of orogenic peridotites, the peridotites from the Platta and Malenco peridotites display a narrow range of Cr contents for widely varying Al_2O_3

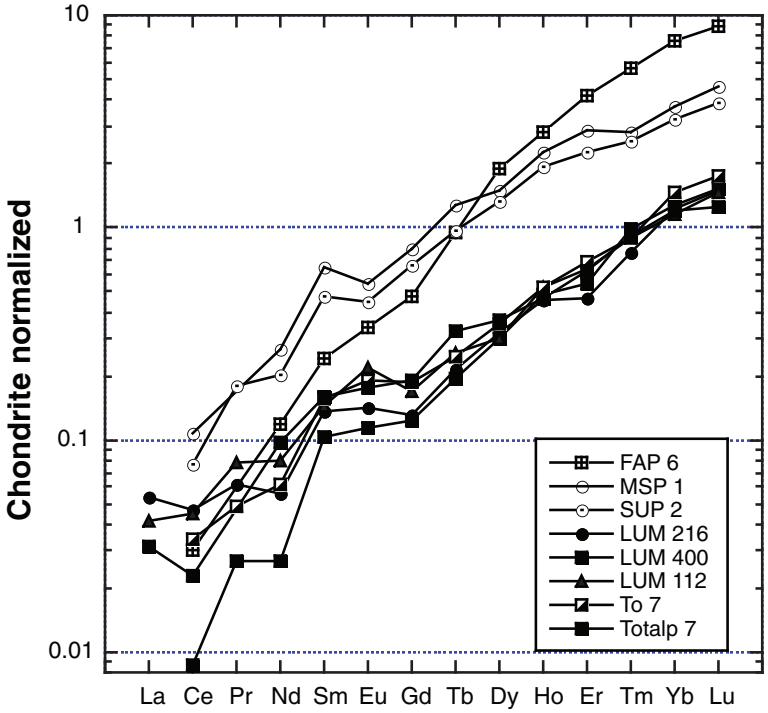

Fig. 7. Chondrite-normalized REE patterns of orthopyroxene from the Eastern Central Alps peridotites. Sample FAP 6 is an orthopyroxene from the symplectitic intergrowth shown in Fig. 4. The strongly fractionated REE pattern with $(Ce/Yb)_N < 0{\cdot}005$ indicates that orthopyroxene inherited its REE pattern from precursor garnet. Such steep REE patterns have also been reported from the Zabargad peridotite (Vannucci *et al.*, 1993*b*). It should be noted that the orthopyroxene REE content is significantly higher in samples from the lower Platta unit, compared with Malenco and Totalp.

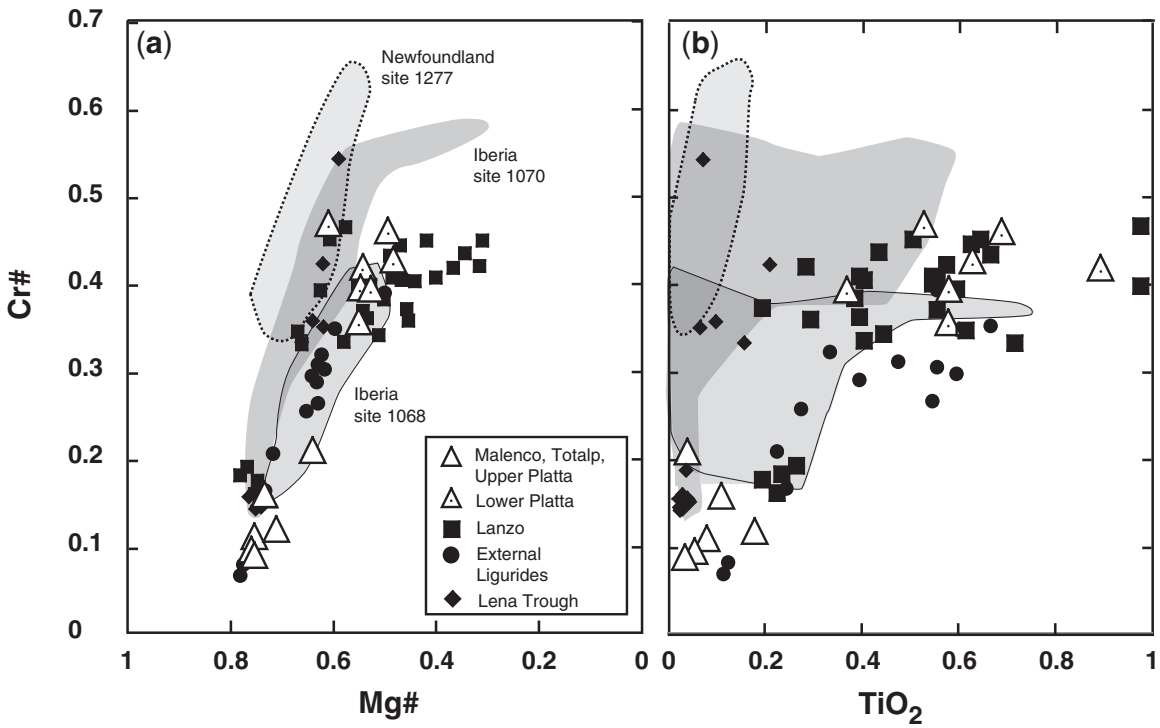

Fig. 8. Spinel compositions in the Malenco, Totalp and Platta peridotites. Spinels from Malenco and Totalp have low Cr-number and low TiO_2 contents, whereas spinels from the lower Platta unit display elevated Cr-number and TiO_2 contents exceeding 0·4, similar to plagioclase peridotites from Iberia and Lanzo. Data for external Ligurides are from Rampone *et al.* (1995); for Lanzo peridotites from Piccardo *et al.* (2007) and Kaczmarek & Müntener (2008); for Iberia–Newfoundland peridotites from Hébert *et al.* (2001) and Müntener & Manatschal (2006).

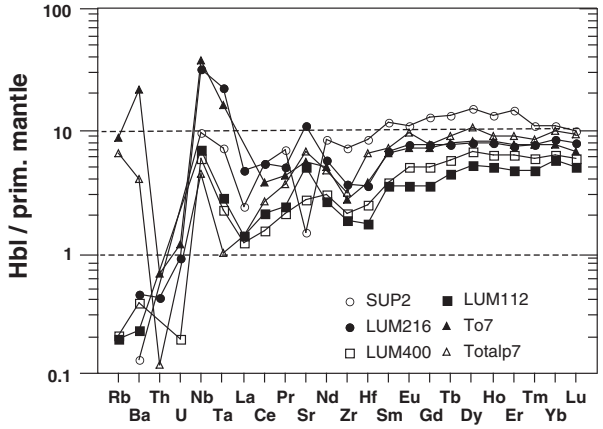

Fig. 9. Primitive mantle-normalized hornblende trace element patterns for samples from Malenco, Totalp and Platta. All Ti-hornblendes show $Nb_N > Ta_N$ and low U–Th contents. Ti-hornblendes that equilibrated with spinel peridotite assemblages show Sr anomalies >1, whereas the only sample from the lower Platta unit that preserved Ti-hornblende shows a large negative Sr anomaly, consistent with equilibration with plagiocase.

contents (Fig. 10c), in contrast to cratonic peridotites (Canil, 2004). Figure 10f illustrates the covariation of Al_2O_3 vs Yb for the analyzed peridotites. Although the general trends for the Platta and Malenco peridotites are similar, there is a tendency for the Platta peridotites to be higher in Al_2O_3, closely corresponding to the 1·5 GPa melting trend (Canil, 2004). However, as discussed in detail below, our alternative interpretation is that the Al-rich peridotite of the lower Platta unit represents peridotites refertilized by a basaltic melt that was produced at shallow levels.

Figure 11 shows bulk-rock trace element diagrams for the analyzed samples. Chondrite-normalized REE data from the Malenco peridotites show moderately fractionated REE patterns (LREE/HREE: 0·2–0·8) at overall lower absolute REE concentrations than the samples from the lower Platta unit (Fig. 11a and e). One sample from the upper Platta unit displays HREE values that are substantially higher than those of primitive mantle (Fig. 11c), which is probably the result of small, disrupted pyroxenite veins within the mantle peridotite. Bulk-rock REE data from the lower Platta unit display mostly fertile compositions, with $(Ce/Yb)_N > 0·5$ and HREE >2 (Fig. 11e and f). The elements Sr and Eu display random positive or negative anomalies on primitive mantle normalized trace element variation diagrams (Fig. 11f) that are most probably related to serpentinization processes. Surprisingly, many samples from the lower Platta unit display positive Eu anomalies, whereas Sr is consistently negative (or below detection limit). The exceptions to the overall trend are two samples with strongly fractionated MREE–HREE [e.g. $(Sm/Yb)_N < 0·2$] coupled to enriched LREE patterns with $(La/Nd)_N > 1$ (Fig. 11f). One of these samples has an extremely depleted Nd isotope composition (Müntener *et al.*, 2004). The enriched LREE pattern coupled with a positive Eu anomaly could result from post-melting crystallization of plagioclase.

Comparison of U vs Th distributions in primitive mantle normalized trace element patterns of the Malenco rocks (Fig. 11b) suggests no systematic variation for peridotites, whereas most of the Platta samples display systematic positive anomalies for U compared with Th (Fig. 11d and f), a feature that is common for strongly serpentinized peridotites (e.g. Bodinier & Godard, 2003).

DISCUSSION

Rather than discussing mantle melting and refertilization as stand-alone processes the exposures of the Eastern Central Alps offer the opportunity to integrate these in a spatial context. The geochemical trends observed in the Totalp–upper Platta–Malenco (spinel peridotites) and lower Platta peridotites are comparable with the spatial variations observed in drill cores along the Iberia–Newfoundland rifted margins. The similarities seen in datasets from Iberia–Newfoundland and the Alpine ophiolites suggest that the underlying igneous and geodynamic processes are comparable with each other. Given the paucity of spatially controlled compositional data on peridotites from present-day ocean–continent transition zones, the observed spatial variations represent the best-constrained dataset with which to discuss the thermal evolution of extensional, magma-poor systems.

We first evaluate orthopyroxene–clinopyroxene trace element partition coefficients for spinel and plagioclase peridotites. We then discuss the generation of the mineral major and trace element variations by melting and refertilization processes. We consider a combined near-fractional melting model in the garnet and spinel stability fields to explain the chemistry of those peridotites with no signs of syn-rift refertilization. Then, we discuss refertilization models, which might account for the fertile signature of the plagioclase peridotites. Consequently, this study addresses the implications of refertilization on the contrasting thermal histories of different mantle segments during continental break-up and their relationship to the generation of ocean–continent transition zones.

Trace element distribution between clinopyroxene, orthopyroxene and hornblende

Very different orthopyroxene–clinopyroxene trace element partition coefficients may be anticipated for equilibration under different thermal regimes. As illustrated in Fig. 12a, the spinel peridotites show orthopyroxene–clinopyroxene partitioning that is systematically lower than that of the plagioclase peridotites of the lower Platta unit. The

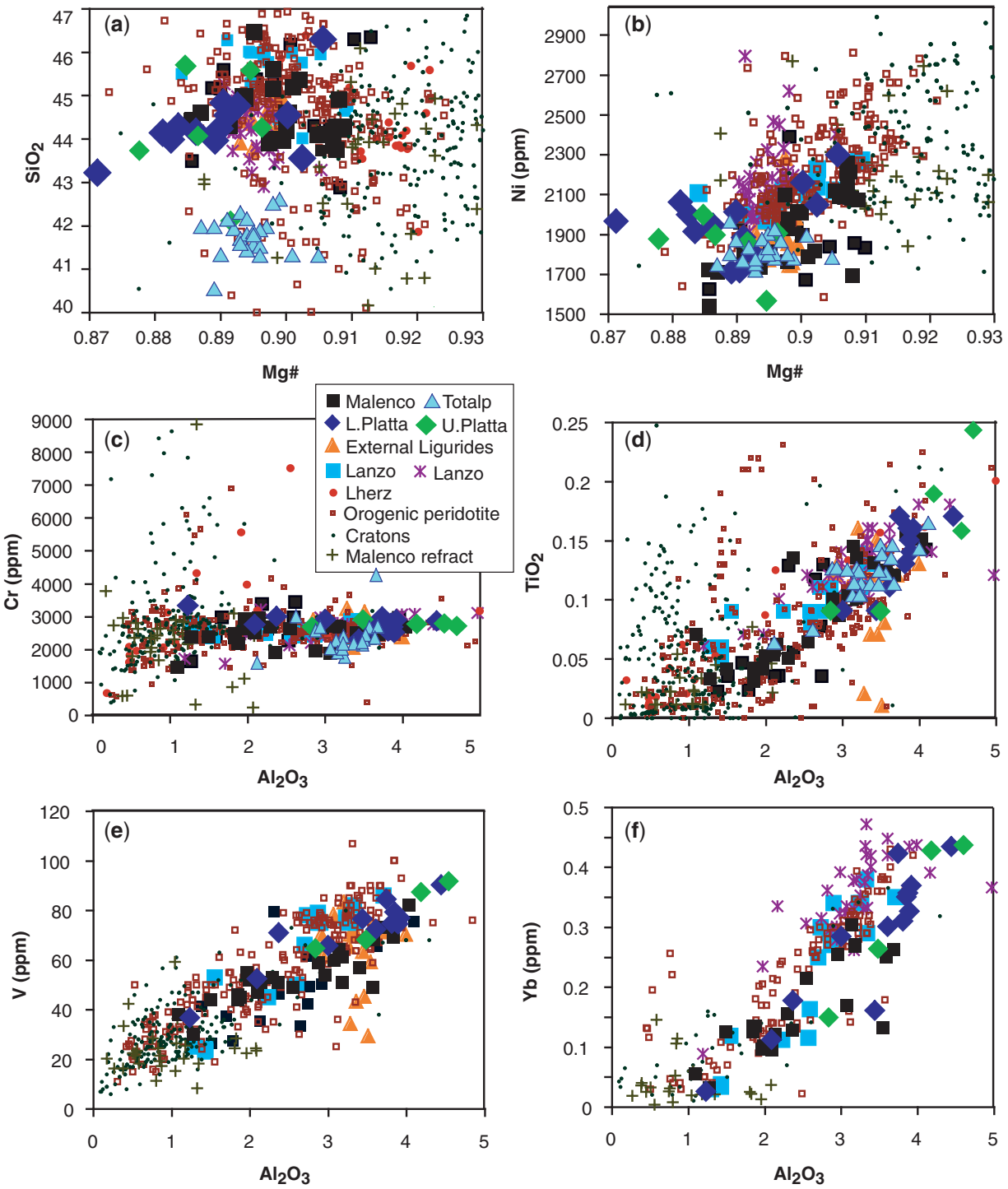

Fig. 10. Bulk-rock compositions of the Malenco and Platta peridotites. (a) Mg-number vs SiO_2, (b) Mg-number vs Ni (ppm), (c) Al_2O_3 (wt %) vs Cr, (d) Al_2O_3 vs TiO_2, (e) Al_2O_3 vs V, (f) Al_2O_3 vs Yb. Data for orogenic peridotites and cratons are from the compilation of Canil (2004), For most trace elements, bulk-rock data are fairly similar to the compiled data for orogenic peridotites. Lanzo data are from Piccardo *et al.* (2007) and Kaczmarek & Müntener (2009); Lherz data from Le Roux *et al.* (2007); Totalp data from van Acken *et al.* (2008).

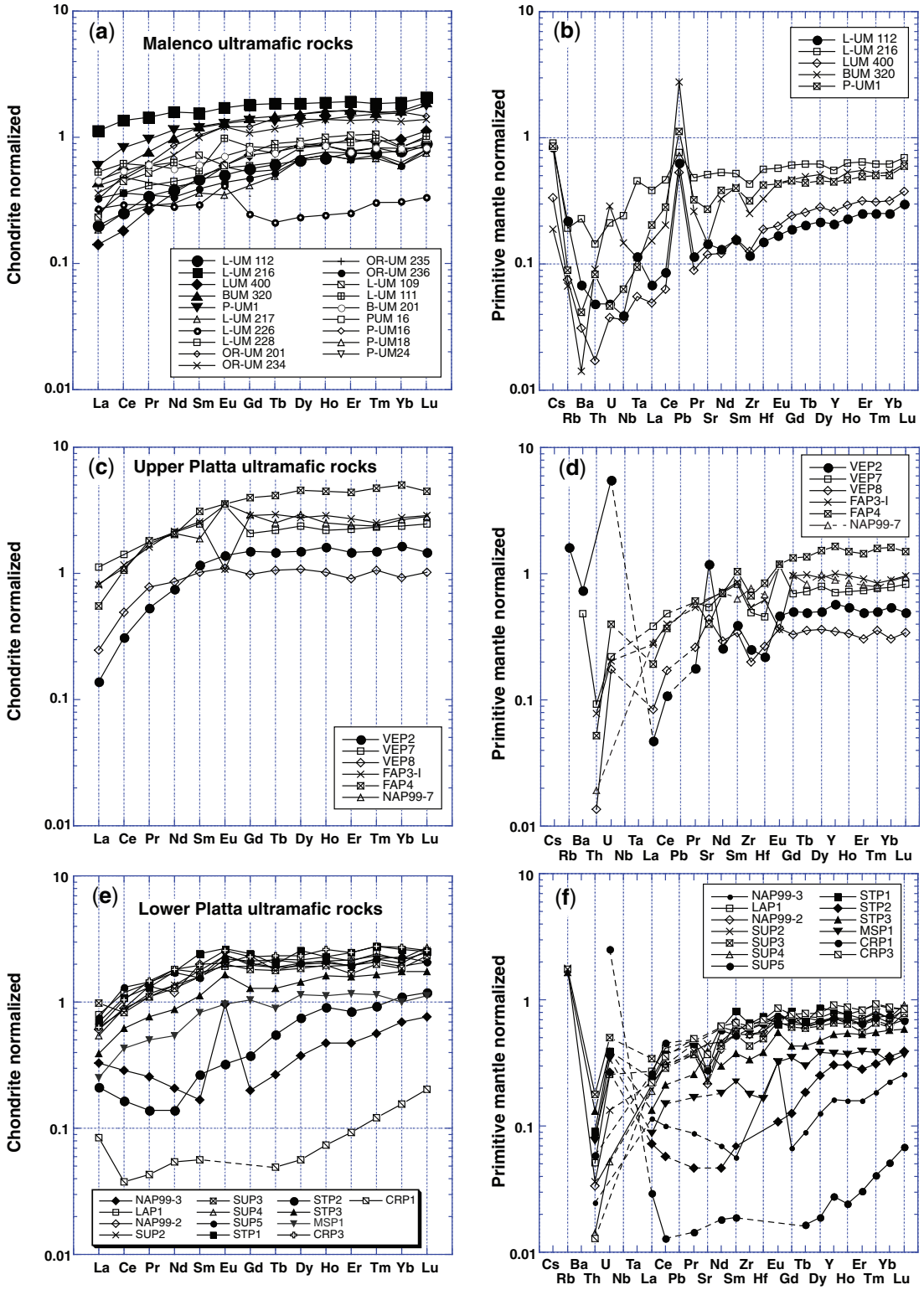

Fig. 11. Trace element compositions of Malenco and Platta ultramafic rocks. (a, b) Malenco, (c, d) upper Platta, (e, f) lower Platta. Chondrite values are from McDonough & Sun (1995); primitive mantle values from Sun & McDonough (1989).

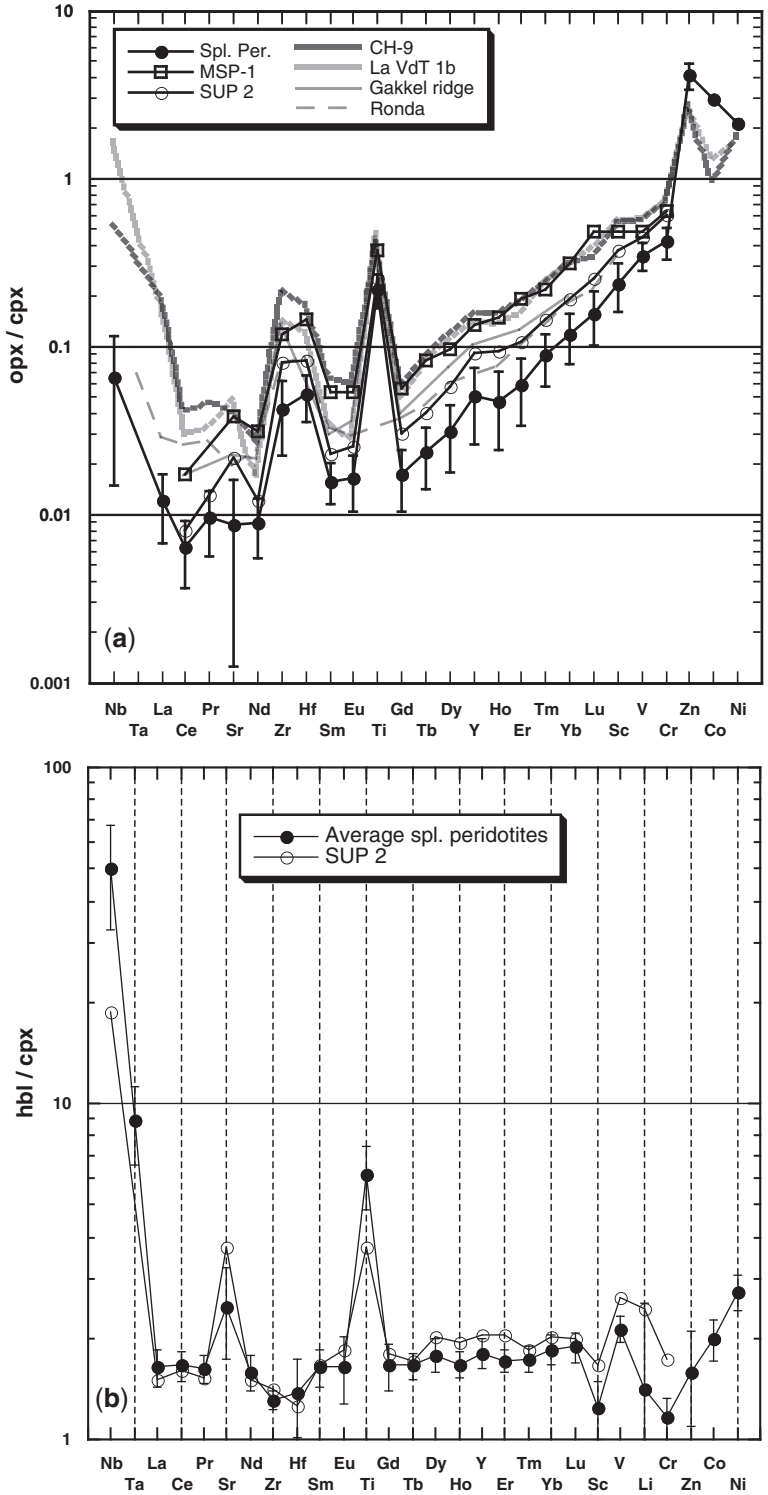

Fig. 12. (a) Orthopyroxene–clinopyroxene trace element partitioning: •, average of five spinel lherzolites from Malenco and Totalp. Error bars represent 1 SD from the average; ○, SUP-2; □, MSP-1, both from the lower Platta unit. Continuous line shows average of spinel lherzolites and spinel harzburgites from Gakkel Ridge (Hellebrand *et al.*, 2005); grey bold lines are data from the Chenaillet ophiolite and the Lanzo peridotites (O. Müntener, unpublished data). (b) Hornblende–clinopyroxene trace element partitioning: •, average of five spinel lherzolites of Malenco and Totalp; ○, SUP-2.

uncertainties for the spinel peridotites are small (as indicated by the error bars), and the consistency of our data and those from Ronda (Garrido *et al.*, 2000) and the Gakkel Ridge (Hellebrand *et al.*, 2005) suggests that these datasets are reliable, even for the highly incompatible elements. There is a first-order difference between the $K_d^{opx/cpx}$ between spinel and plagioclase peridotites in our samples, with the K_d for the plagioclase peridotites being generally higher. This is true not only for the studied samples but also for plagioclase peridotites from the Lanzo and Chenaillet ophiolites (based on our own unpublished data). The consistent slope, but variable absolute values of $K_d^{opx/cpx}$ suggests that orthopyroxene and clinopyroxene crystallized or recrystallized concurrently, close to $K_d^{opx/cpx}$ equilibrium. Pyroxene thermometry, presented above, indicates equilibration temperatures of 920 (±30)°C for the spinel peridotite samples, which are substantially lower than those calculated for the plagioclase peridotites (1050–1170°C). This suggests that trace element $K_d^{opx/cpx}$ values are strongly temperature dependent, as suggested previously (Seitz *et al.*, 1999; Witt-Eickschen & O'Neill, 2005) based on studies of spinel peridotite xenoliths. The potential of trace element partitioning for evaluating thermal regimes beneath ocean–continent transition zones and mid-ocean ridges is further discussed below.

In striking contrast to the temperature-dependent $K_d^{opx/cpx}$, trace element partitioning between hornblende and clinopyroxene is much less variable and most elements have K_d values between one and two, except for Sr and Ti, and especially Nb and Ta (Fig. 12b). Within error, many of the $K_d^{opx/cpx}$ values for spinel peridotite and plagioclase peridotites are similar, indicating no obvious temperature dependence. Vannucci *et al.* (1995) concluded that hornblende is a common mineral in subcontinental peridotites and that, in most cases, trace element equilibrium is reached between hornblende and clinopyroxene.

Degree of melting: garnet involved?

It has previously been shown that spinel Cr-number coupled with HREE abundance can be used as a quantitative melting indicator for plagioclase-free spinel peridotites (Hellebrand *et al.*, 2001). Spinel Cr-number can vary from 0·09 to 0·2, indicating less than about 6% of melting of a fertile spinel peridotite source, consistent with the elevated HREE contents. However, rare relics of strongly LREE-depleted clinopyroxene from the lower Platta unit are similar to those from abyssal peridotite (Fig. 6). The relatively low MREE to HREE ratios coupled with high Yb_N are consistent with a combination of initial melting in the garnet stability field followed by further melting in the spinel peridotite field (Müntener *et al.*, 2004). The authors calculated that about 4% melting in the garnet field followed by an additional 4–6% melting in the spinel field best reproduces the MREE to HREE pattern of sample STP-2. In addition, sample STP-2 has a strongly fractionated $(Zr/Hf)_N$ ratio (<0·2), significantly lower than those of clinopyroxene from the Malenco and Totalp spinel peridotites (Fig. 6d). A strongly fractionated $(Zr/Hf)_N$ ratio combined with fractionated $(Sm/Yb)_N$ and high Yb_N thus seems consistent with a component of fractional melting in the stability field of garnet. A low clinopyroxene $(Zr/Hf)_N$ ratio is also characteristic of a second clinopyroxene sample from the lower Platta unit (NAP 99-6), which has an identical MREE to HREE pattern to STP-2, but with essentially flat LREE pattern and enriched Nb and Ta (Fig. 6d). It is likely that this peridotite represents a refertilized variant of STP-2, as shown by the presence of small phlogopite grains. Similar variations at lherzolite–harzburgite contacts have been described for the Lherz massif (J.-L. Bodinier, personal communication).

The Na contents of clinopyroxene from the Eastern Central Alps peridotites provide important constraints on the partial melting or refertilization conditions of these rocks. Sodium concentrations in clinopyroxene from many spinel peridotite from Malenco and Totalp are higher than for depleted MORB mantle (Workman & Hart, 2005) and close to estimates for the primitive mantle (McDonough & Sun, 1995) (Fig. 4a). Sodium is an element of particular importance, as its abundance in basaltic melts is sensitive to the degree of melting and hence it shows significant variation in MORB (Langmuir *et al.*, 1993). Its incompatibility is considered to be similar to that of Nd at low pressure, but at high pressures sodium is less incompatible (Blundy *et al.*, 1995) whereas Nd is more incompatible (Salters *et al.*, 2002). Partial melting at high pressures in the garnet peridotite stability field should quickly decrease the Nd/Na ratio in residual clinopyroxene, whereas this ratio remains approximately constant during melting in the spinel stability field. It is thus likely that Na-rich, but relatively Nd-poor clinopyroxenes are the residues of high-pressure partial melting, whereas Na-poor clinopyroxenes are the residues of low-pressure melt extraction, as evidenced by abyssal peridotites (e.g. Johnson *et al.* 1990). Alternatively, Na-rich clinopyroxene might be formed by refertilization at higher pressure in the spinel peridotite stability field, as inferred for the Lherz and Ronda peridotites (Le Roux *et al.*, 2007; Bodinier *et al.*, 2008).

We tested these hypotheses by calculating three simple partial melting scenarios, with variable partition coefficients for Na, but a constant one for Nd ($D_{Nd}^{cpx/l}=0·2$). Garnet peridotite melting modes were taken from Walter (1998), spinel peridotite melting modes are from Kinzler (1997), and the source mineralogy for spinel peridotite is from Johnson (1998). For consistency the source mineralogy of the garnet peridotite was calculated from the spinel peridotite mineralogy, using the equations of Johnson

et al. (1990). The most important findings are summarized in Fig. 13a. We evaluated a fractional melting model for spinel peridotite (model A in Fig. 13a) to show that the Na–Nd fractionation is not sufficiently extreme to explain samples that plot to the right of the model curve, even though we adopted a sodium-rich subcontinental clinopyroxene as the starting composition. The Na/Nd_N ratio in the garnet peridotite model quickly leads to low Nd_N concentrations as illustrated by model B in Fig. 13a, which can better explain many of the Na-rich, Nd-poor clinopyroxenes. Our model, however, might be extreme by choosing $D_{Na}^{cpx/l} = 0{\cdot}5$; because of the subcalcic nature of clinopyroxene at pressures exceeding 3·0 GPa (e.g. Walter, 1998), it is likely that $D_{Nd}^{cpx/l}$ values are lower than 0·2 (see Salters *et al.*, 2002). Thus applying lower $D_{Na}^{cpx/l}$ distribution coefficients the residual cpx quickly depletes in Nd_N, if high-pressure $D_{Nd}^{cpx/l}$ values are adopted.

Finally, we performed additional 'polybaric' calculations, with 4% of initial melting in the garnet stability field, conversion of the modes into a spinel peridotite assemblage, and then continuing melting in the spinel stability field. This model equally fits many of the data. The sodium content of sample STP-2 is closely matched by this 'polybaric' fractional melting model, and is thus consistent with the results from REE modelling, which suggest that this sample requires an equal amount of garnet and spinel peridotite melting. The garnet-field signature suggests that the onset of melting occurred at a depth exceeding ~80 km, and the limited spinel peridotite facies melting indicates that the final depth of melting is deep compared with slow-spreading ridges. This is in striking contrast to the other samples from the lower Platta unit. Their relatively constant Na_2O contents, coupled with increasing Nd_N (Fig. 13), MREE to HREE ratios >1 and a consistent negative Sr and Eu anomaly (Fig. 6), indicate the presence of plagioclase. Below we evaluate possible liquids that match the clinopyroxene compositions of the plagioclase peridotites.

Refertilization of peridotites in the plagioclase peridotite stability field

Refertilization of depleted spinel peridotite has been proposed as an explanation for the formation of plagioclase peridotite (Dick, 1989; Rampone *et al.*, 1997; Dijkstra *et al.*, 2001; Müntener & Piccardo, 2003) and for the formation of Na-rich spinel peridotite (Elthon, 1992; Bodinier *et al.*, 2008). Based on textural evidence from the plagioclase peridotites, we tested the refertilization hypothesis by modeling basalt–peridotite mixtures. The model simulates crystallization of small amounts of trapped melt in peridotite, followed by recrystallization and equilibrium trace element distribution in the plagioclase peridotite field. By varying the modes of the plagioclase peridotite and the composition of the infiltrating liquid, we tried to match the Na content, the REE, and the Zr–Sr composition of the clinopyroxene. This simple approach, however, does not account for eventual chromatographic fractionation of small melt fractions.

Figure 13b illustrates the results of the refertilization calculations using three liquids [a 4% fractional melt (1) and a 10% batch melt (2) derived from a spinel peridotite source, and (3) a primitive T-MORB basalt (FAB-1, described by Desmurs *et al.*, 2002)]. The starting mode was a lherzolite derived by 4% near-fractional melting of peridotite in the garnet and spinel stability field, respectively (see above). The entrapment and crystallization leads to a rapid increase in Na and Nd, and the Na/Nd_N ratio is similar for all models. However, the necessary fraction of liquid added for a given Nd_N is different, as indicated in Fig. 13b.

We further tested if the REE pattern of clinopyroxene from the plagioclase peridotites could be reproduced by addition of either batch or fractional melts. The reason for this simple modeling is that the bulk-rock compositions do not indicate any clear 'cumulate signature'. Figure 14 illustrates REE refertilization calculations using the same batch and fractional liquids as above, together with the residual sample STP-2, and 'refertilized' samples MSP-1 and an average of five samples from the lower Platta unit that are similar in their trace element content. The crystallization mode and the clinopyroxene/plagioclase ratio of the crystallizing liquid strongly determine the shape of the REE pattern and the negative Eu anomaly. We evaluated different clinopyroxene/plagioclase ratios and found that a ratio of 9/4 matches our data best. It should be noted that, assuming considerably lower or higher amounts of plagioclase in the crystallizing assemblage, the model fails to reproduce the Eu anomalies and the clinopyroxene trace element abundance of the samples. We conclude that ~10–12% addition of a 4% fractional melt reproduces the clinopyroxene concentrations and slopes of the LREE, similar to most of the Platta samples (Fig. 14). However, sample MSP-1 is more consistent with addition of about 4–6% batch melt produced in the spinel stability field (Fig. 14), to fit both the lower absolute REE content and the significantly less fractionated LREE.

It has been proposed that the Sr–Zr behavior of clinopyroxene in spinel and plagioclase peridotite might be used as a proxy for monitoring the subsolidus spinel to plagioclase transition in mantle peridotites (Rampone *et al.*, 1993). However, based on textural evidence and the observation that plagioclase peridotites are systematically more fertile compared with spinel peridotites in Alpine ophiolites, it has been proposed that melt infiltration and reaction might be the dominant process of plagioclase formation (Müntener & Piccardo, 2003), similar to observations from mid-ocean ridges (Dick, 1989). In an attempt to test the latter hypothesis, we plotted the clinopyroxene Sr and Zr content, together with melting and

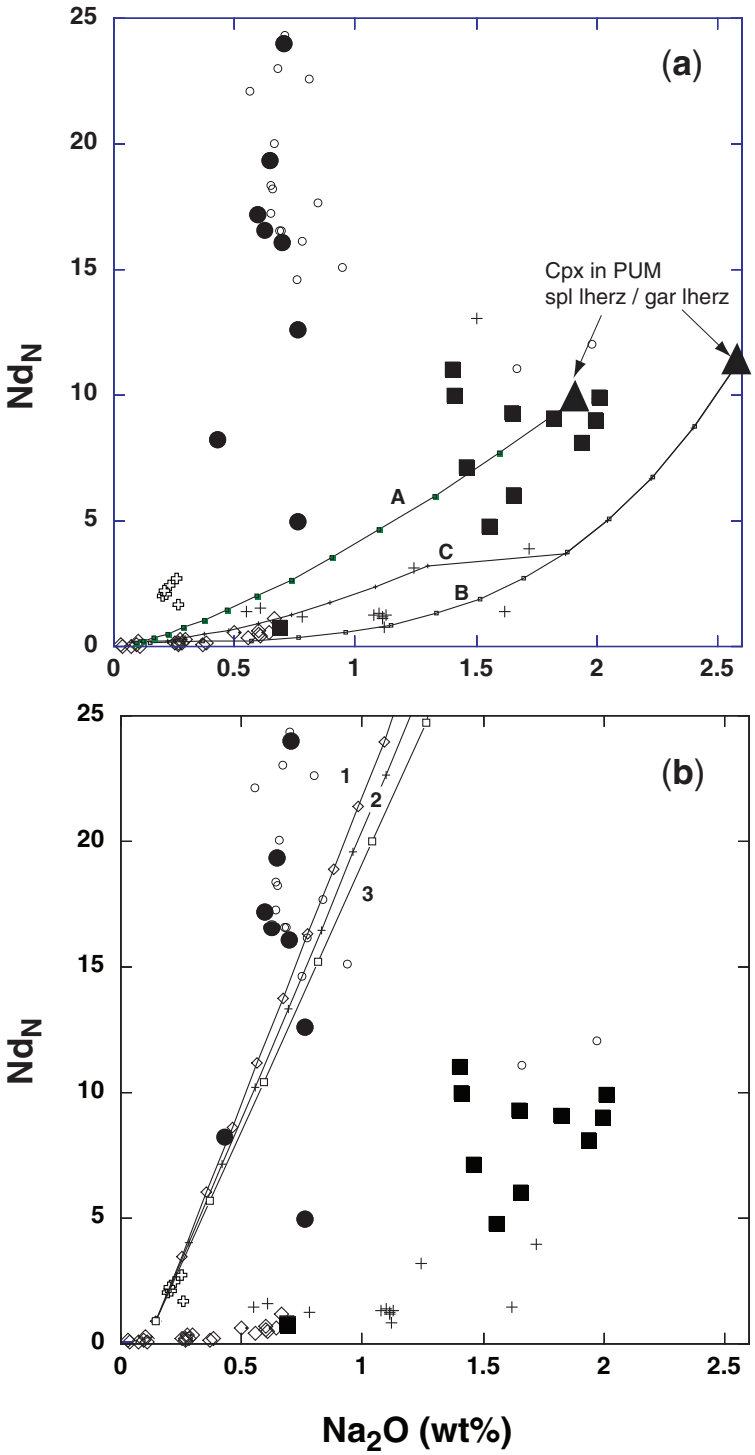

Fig. 13. (a) Na_2O vs Nd_N in clinopyroxene from the Eastern Central Alps peridotites and other peridotites from ocean–continent transitions. (a) Three melting models have been calculated assuming a primitive upper mantle source (PUM) from McDonough & Sun (1995). Model A: fractional melting of a fertile spinel peridotite (PUM) with $D_{Na}^{cpx/l}$ of 0·3; model B: fractional melting of a garnet peridotite with $D^{cpx/l}$ of 0·5; model C: a 'polybaric' melting model with 4% of melting of a garnet peridotite ($D_{Na}^{cpx/l}=0{\cdot}5$) followed by additional melting in the spinel peridotite field ($D_{Na}^{cpx/l}=0{\cdot}3$). It should be noted that the higher initial Na content of the clinopyroxene in garnet peridotite is a consequence of the conversion of spinel peridotite to garnet peridotite mineralogy. Spinel peridotite has higher modal clinopyroxene at a given bulk-rock composition and thus sodium in clinopyroxene is more 'diluted' in spinel peridotite that in garnet peridotite. Additional calculations with residual porosities of 0·1 and 0·5% do not significantly change our results, compared with variations in the partition coefficients. (b) Refertilization models (in steps of 1%) at low pressure in the plagioclase stability field, assuming a LREE-depleted source (4% near-fractional melting in the garnet stability field, followed by an additional 4% melting in the spinel stability field). The refertilizing agent is a 10% batch melt (1), 4% fractional melt (2) and a T-MORB composition (3) from Desmurs *et al.* (2002), respectively. Refertilization model partition coefficients for Na are from Blundy *et al.* (1995), REE partition coefficients are from the compilation of Suhr *et al.* (1998), except for plagioclase, which is from McKenzie & O'Nions (1991). +, Lena trough peridotites (Hellebrand & Snow, 2003); ◇, CIR peridotites (Hellebrand *et al.*, 2002); ○, External Ligurides (Rampone *et al.*, 1995); open crosses: Internal Ligurides (Rampone *et al.*, 1996). ●, plagioclase peridotites; ■, spinel peridototes

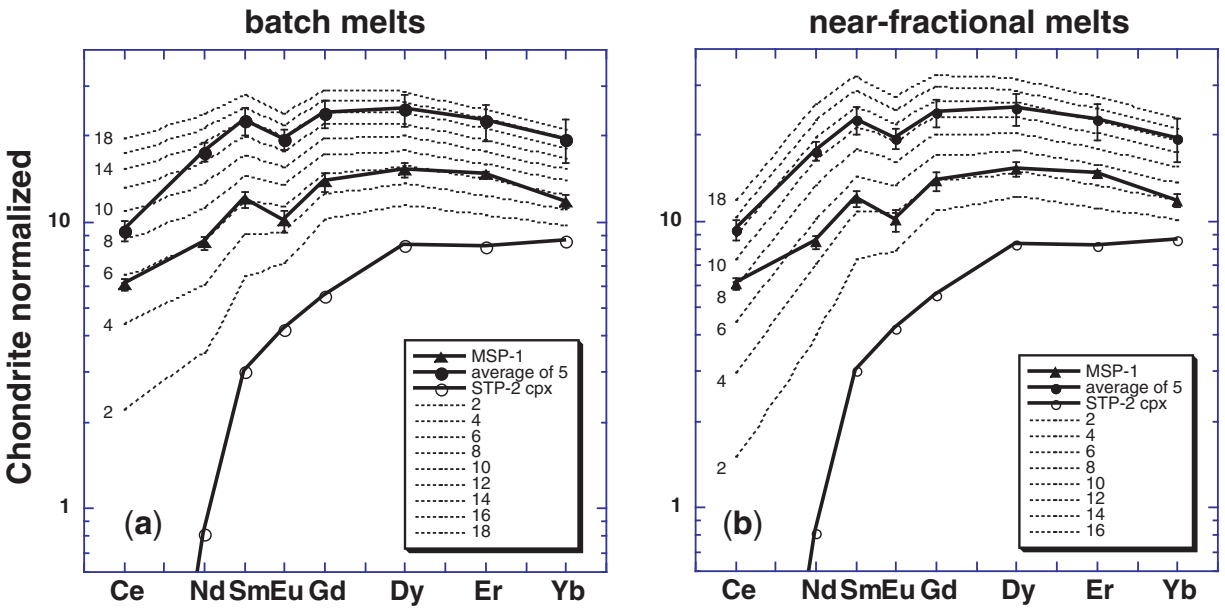

Fig. 14. Simple REE refertilization models with the most depleted clinopyroxene (sample STP-2) as the starting composition for the calculations. Dotted lines indicate addition of 2% increments of liquids followed by equilibrium trace element distribution among the phases. The near-fractional model has been obtained by adding 2% increments of a melt derived from 4% fractional melting of an N-MORB source. The batch melt model was calculated by adding increments of 2% MORB derived from 10% batch melting of peridotite to the depleted peridotite STP-2. This model displays a better fit to the composition of MSP-1. clinopyroxene–melt partition coefficients as in Fig. 13.

refertilization models using the same source composition as in Fig. 14 to test a possible origin by melt infiltration. It is well known that Sr is compatible in plagioclase, but the mineral–liquid K_d strongly depends on the An content (Blundy & Wood, 1991). A further difficulty in choosing an appropriate K_d^{Sr} for clinopyroxene and plagioclase is that none of the available experimental studies simultaneously determined clinopyroxene, plagioclase and liquid. We adopt to the partition coefficients of McKenzie & O'Nions (1991) for Zr and Sr, which result in a $D_{Sr}^{cpx}/D_{Sr}^{plg}$ of 0·0335. Figure 15 demonstrates that Zr and Sr are similarly incompatible during batch or fractional melting in the spinel peridotite field. After less than 10% near-fractional melting, Zr and Sr concentrations approach abyssal peridotite compositions (e.g. Johnson *et al.*, 1990), whereas batch melting models require >20% melting to achieve low Sr and Zr contents. It should be noted that most samples from the Eastern Central Alps peridotites approach or even exceed recent estimates of the depleted MORB mantle (DMM) reservoir of Workman & Hart (2005), supporting the fertile composition of most of the studied peridotites.

Clinopyroxenes from plagioclase peridotites have very high Zr/Sr ratios that cannot be explained by any simple melting model of either spinel or garnet peridotite. For illustration purposes, we used the same input parameters (e.g. source composition, infiltrating agent and crystallizing phase proportions) as in Fig. 14, to model refertilization in the Sr–Zr variation diagram. The refertilization trends critically depend on the crystallization mode, as Sr is compatible in plagioclase. If the crystallization mode is held constant (e.g. as above, clinopyroxene/plagioclase ratio is 9:4), the variability between the models is controlled by the composition of the refertilizing melt. As illustrated in Fig. 15, the results are similar for different refertilization agents, produced by 4% near-fractional melting (curve 2) and 10% batch melting (curve 1).

By combining the different results from REE, Na, Sr and Zr modeling, we conclude that adding between 5 and 12% near-fractional and/or batch melts to a previously depleted peridotite, followed by equilibrium trace element distribution in the plagioclase peridotite field best explains the data from the lower Platta plagioclase peridotites. Addition of even small amounts of melt dramatically changes the trace element ratios in clinopyroxene. We conclude that the typical concave-upward clinopyroxene REE pattern with $Gd/Yb_N > 1$ can be explained by refertilization of peridotites by MORB-type magmas in the plagioclase stability field. Similar results were obtained for the Lanzo and Corsica peridotites (Rampone *et al.*, 1997; Piccardo *et al.*, 2007).

It is important to realize that bulk-rock compositions do not indicate any clear 'cumulate signature' from the process of refertilization. We conclude that the composition of some lower Platta peridotites (coupled with the 'weak

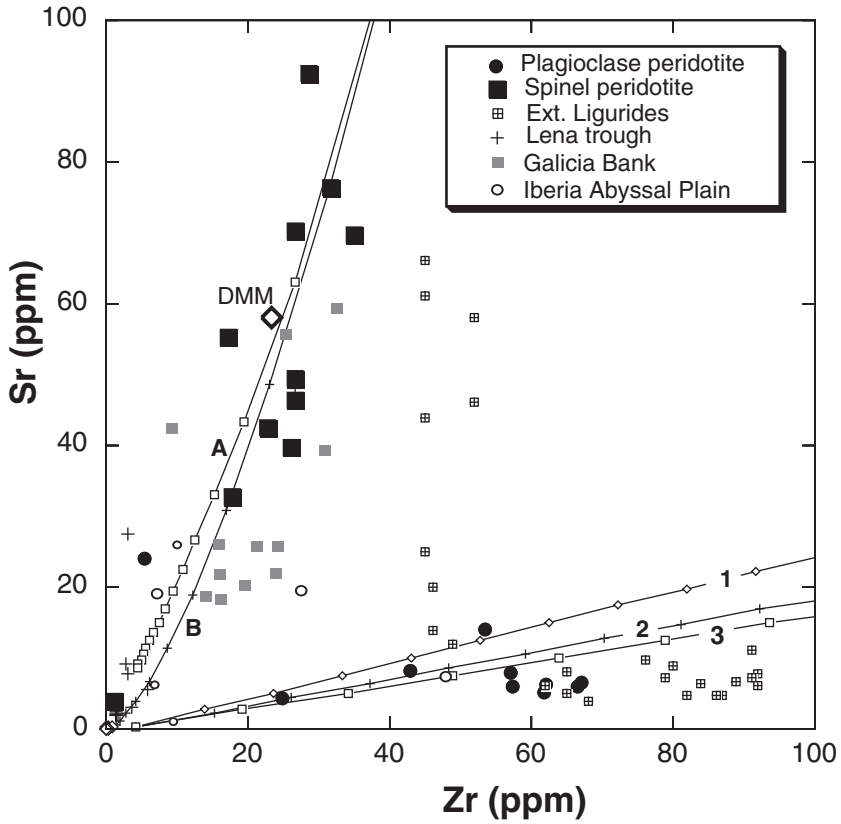

Fig. 15. Sr vs Zr in clinopyroxene from the Eastern Central Alps peridotites. Curves A and B represent the results of batch melting and perfect fractional melting of a spinel peridotite source. It should be noted that batch melting alone cannot reproduce the low Zr and Sr contents of many samples. Refertilization models 1, 2 and 3 are calculated using the same parameters as in Fig. 13.

positive Eu anomaly') requires the addition of a basaltic component (refertilization) to the peridotites. Together with the thermometric calculations that indicate substantially higher temperatures of equilibration (see above), this strongly suggests that the boundary between the refertilized peridotites (the plagioclase peridotites of the lower Platta unit), and the peridotites that are unaffected by refertilization in the plagioclase field (the peridotites of the upper Platta unit, Malenco, and Totalp) represents a boundary separating two units with a fundamentally different thermal history.

Constraints on the origin and thermal evolution of the studied peridotites

Two distinct exhumation mechanisms have been proposed to explain the mineralogy and the thermal history of peridotites in ocean–continent transitions. One option is that the peridotites are passively exhumed and record subsolidus processes (e.g. Rampone *et al.*, 1993; Chazot *et al.*, 2005). In this scenario plagioclase peridotites form essentially by subsolidus processes (e.g. by the generalized reaction: pyroxenes + spinel → olivine + plagioclase; see Fig. 16). An alternative is that the plagioclase crystallized (together with pyroxenes and/or olivine) from melt migrating by porous flow in the thermal boundary layer (Elthon, 1992; Müntener & Piccardo, 2003). Given the contrasting equilibration conditions for the studied spinel peridotites (~920°C, ~1·5 GPa) and plagioclase peridotites (~1050–1170°C, <1·0 GPa) they clearly do not follow one simple geotherm. The plagioclase peridotites display an evolution of increasing temperatures and decreasing pressure, whereas the spinel peridotites record simple cooling and passive exhumation of mantle lithosphere. There are at least two possible interpretations to explain these data. Either the peridotites originated from different mantle domains with different geotherms that were juxtaposed during continental break-up, and/or some parts of the lithospheric mantle were infiltrated by and reacted with migrating melt thus modifying an inherited geotherm. Field relations indicate that at least some of the spinel peridotites are subcontinental (Trommsdorff *et al.*, 1993; Müntener & Hermann, 1996; Desmurs *et al.*, 2001) and that equilibration temperatures derived from pyroxene thermometry represent a cooling history that is unrelated to the geotherm at the beginning of continental break-up (Müntener *et al.*, 2000). These peridotites provide no

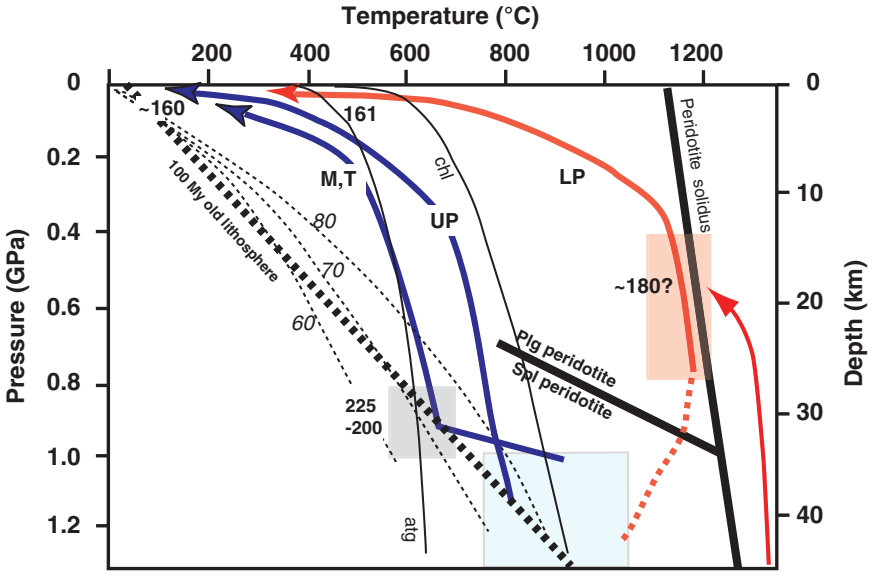

Fig. 16. Schematic illustration of the contrasting pressure–temperature paths of the various peridotites during thinning of the continental crust. Peridotite solidus is from Hirschmann (2000), heat flow data (dashed lines) from Chapman (1986). The 100 Myr lithosphere geotherm is adapted from Van Avendonk *et al.* (2006) and crosses the solidus at ~62 km and 1330°C. Thin red arrow indicates syn-rift melts that were produced during decompression melting and refertilize peridotites during thinning of the continental crust. Thick blue and red arrows indicate the different exhumation paths of the peridotites. Shaded grey field indicates P–T conditions for the Malenco and Totalp peridotites at the beginning of rifting (Peters, 1968; Müntener *et al.*, 2000). Light blue field indicates equilibration conditions of spinel peridotites beneath continental crust prior to extension. Red field indicates conditions of refertilization beneath thinned continental crust. Age determinations (bold numbers) are from Villa *et al.* (2000) and Schaltegger *et al.* (2002). Serpentine (antigorite) and chlorite stability fields are from Ulmer & Trommsdorff (1999). LP, lower Platta; UP, upper Platta; M, Malenco; T, Totalp.

evidence for syn-rift melt migration and have been interpreted to follow a 'cold exhumation' path (Müntener & Piccardo, 2003). Conversely, temperatures calculated for the plagioclase peridotites are much higher and approach near-solidus conditions. It has been shown that many peridotites from the Alps, Iberia and (ultra-)slow-spreading ridges preserve textural and compositional relics of melt–rock reaction (Cannat & Casey, 1995; Müntener & Manatschal, 2006; Seyler *et al.*, 2007). The contrasting ages for crystallization of mafic rocks (~160 Ma: Rampone *et al.*, 1998; Schaltegger *et al.*, 2002; Kaczmarek *et al.*, 2008) and for peridotite partial melting as determined by model ages calculated from Nd-isotopes (Rampone *et al.*, 1998; Müntener *et al.*, 2004) suggests that there are commonly no simple melting–residue relationships. Instead we favor the hypothesis of inherited subcontinental relics that are partially overprinted and/or erased during refertilization and subsequently equilibrated in the plagioclase peridotite field. The idea of ancient mantle relics has recently also become attractive to explain isotopic heterogeneity in the oceanic mantle (e.g. Harvey *et al.*, 2006; Goldstein *et al.*, 2008) and has led to a paradigm shift in studies of mid-ocean ridges, away from a view that basalt formation and mantle depletion are always genetically linked. We conclude that the most common origin of the plagioclase peridotites in Alpine ophiolites is refertilization by migrating magmas and thermal erosion of ancient lithosphere at some time during crustal thinning between the late Triassic and middle Jurassic, but prior to the emplacement of gabbro bodies and dikes, which are dated to 166–158 Ma (see summary by Kaczmarek *et al.*, 2008).

The different pressure–temperature paths conceptually illustrate the contrasting thermal histories of the Malenco–upper Platta–Totalp and the lower Platta peridotites (Fig. 16). It follows that subcontinental peridotites ('cold exhumation') and infiltrated peridotites ('hot exhumation') are juxtaposed within a narrow zone where thermal gradients are high. This is schematically illustrated in Fig. 17, where the most important field relations and the different peridotite types are shown. The infiltrated and subcontinental domains are presumably separated by peridotite mylonites. Such mylonites may act as permeability barriers for migrating magmas, as inferred for a mantle shear zone in the Lanzo peridotite (Kaczmarek & Müntener, 2008). In addition, the high-temperature mylonites are cut by low-temperature brittle detachment faults. These faults are similar to detachments described in oceanic core complexes (e.g. Tucholke *et al.*, 1998; Ildefonse *et al.*, 2007).

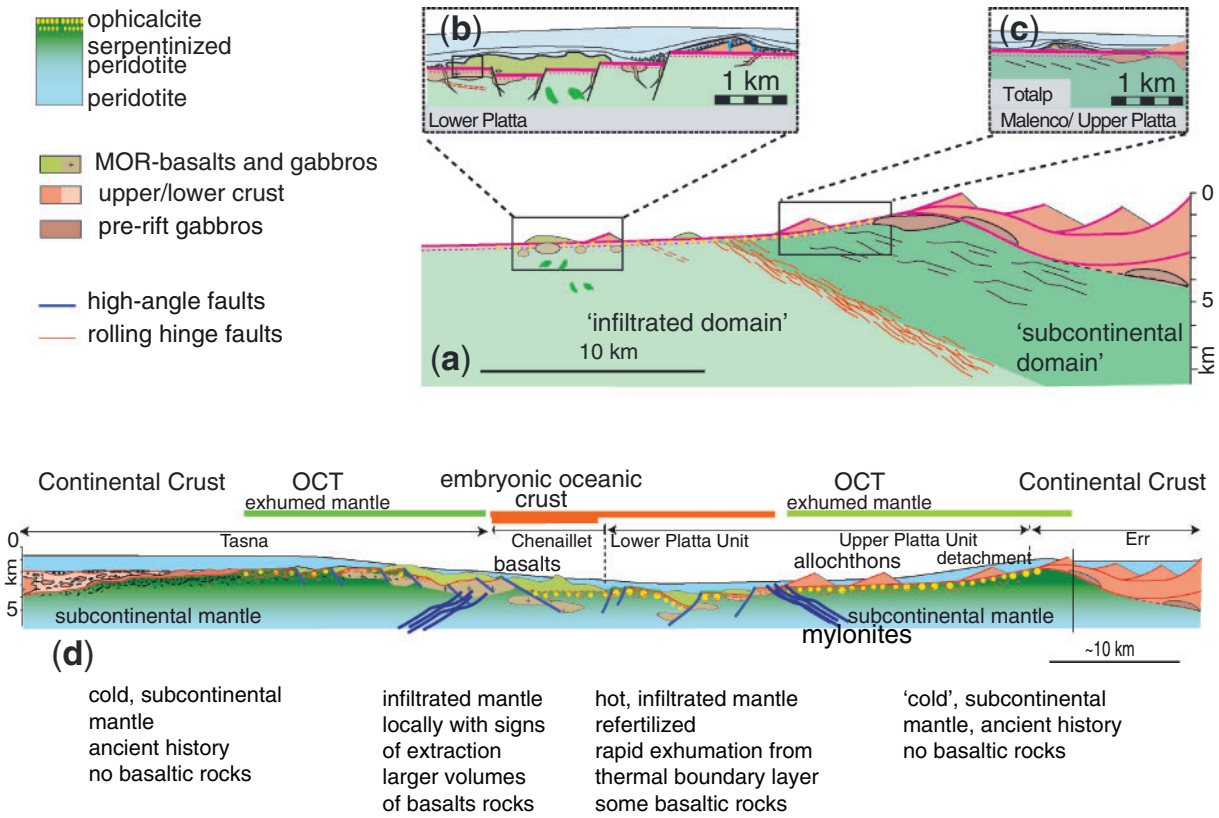

Fig. 17. (a) Distribution of subcontinental and infiltrated domains of mantle peridotite within an ocean–continent transition. It should be noted that the subcontinental domain contains abundant (garnet) pyroxenites, whereas they are scarce in the infiltrated domain. Dunites are found in both peridotite types. (b) Detailed field relationships in the lower Platta unit between basalts, gabbros, detachment faults and normal faults. (c) Detailed relationships between exhumed lower crust, subcontinental mantle and detachment faults. (d) Summary cross-section across a nascent ocean based on the observations made in the Tasna, Chenaillet, Malenco and Platta units (see Fig. 1 for locations). The section shows the observed relationships between detachment structures and exhumed mantle rocks, and the spatial distribution of the mantle types. Mantle rocks exhibiting signs of melt extraction were found in the Western Alps peridotites.

Geophysical consequences of melt infiltration: a 'lithospheric sponge' and inhibited subsidence of thinned continental crust during extension

One of the more surprising results from the numerous tentative reconstructions of the Iberia–Newfoundland margins is that extreme crustal thinning to less than 10 km had to occur before the major episode of detachment faulting became active (Manatschal *et al.*, 2001). Another puzzling result in deep, magma-poor, rifted margins is that extreme thinning does not appear to be associated with normal high-angle faulting, nor strong syn-extensional subsidence. This is not compatible with the 'classic McKenzie model' that is widely used in geodynamic reconstructions that assume a simple temperature-dependent density distribution in the mantle (McKenzie, 1978). This model does not include compositional and pressure-dependent phase changes. The effects of phase changes have been addressed recently (e.g. Simon & Podladchikov, 2008). Given that subsolidus phase transitions, in particular the spinel to plagioclase transition with decreasing temperature, are often incomplete and slow, we propose an alternative mechanism. One possible idea to explain the anomalously shallow depositional environment of syn-rift sedimentary sequences along magma-poor rifted margins is that thinning of the crust is associated with the emplacement of hot and infiltrated lithospheric mantle beneath the future continental margin. Thus we assume that during extreme thinning of the continental crust early syn-rift melts are trapped in the mantle lithosphere above the upwelling asthenosphere. This 'lithospheric sponge' is, compared with an efficient melt extraction system at fast-spreading ridges or at segment centers within slow-spreading ridges, compositionally buoyant and provides an additional driving force for rapid exhumation of impregnated peridotites. Rapid exhumation would inhibit complete reequilibration of the refertilized peridotites and could explain a variety of petrological, tectonic and geophysical observations, as follows. (1) The time required to erase the extreme compositional variations of spinel and pyroxenes in peridotites

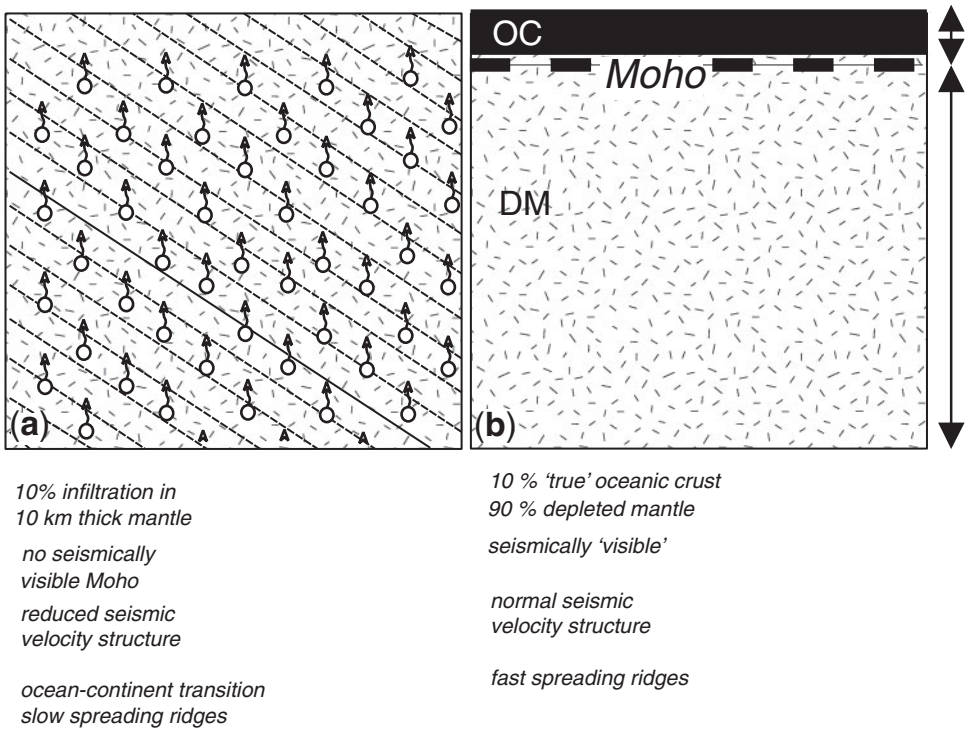

Fig. 18. Conceptual models on the importance of melt infiltration vs melt extraction at the top of the mantle lithosphere, which is largely governed by the thermal structure of the uppermost mantle. Perfect extraction leads to oceanic crust with a well-defined Moho (b), whereas refertilization and stagnation would form a compositionally buoyant piece of mantle without a clear Moho (a). Model (a) might be important for the formation of oceanic core complexes. Later serpentinization effects are neglected. This model could explain the widespread occurrence of refertilized peridotite on the seafloor in ocean–continent transitions (Iberia–Newfoundland, Alps), in (ultra-)slow-spreading ridges and any transitional stages between the two.

(Kaczmarek & Müntener, 2008) is longer than the residence time of the 'lithospheric sponge' above the melting region. (2) The equilibration temperatures of peridotites from the Alps calculated by conventional major element thermometry and more novel trace element thermometers demonstrate that many plagioclase peridotites record much higher temperatures (on average 1150–1200°C) compared with spinel peridotites. We argue that these high equilibration temperatures are a fingerprint of syn-rift refertilization of mantle peridotites. Because many magma-poor rifted margins do not allow direct access to such mantle exposures because of post-rift sedimentation, we speculate that shallow-water syn-rift sediments may be used as an indicator of subsidence retardation in deep-water rifted margins and may be linked to mantle refertilization at depth. Another effect of such refertilization processes at depth might be anomalously high heat flow, which has been observed in the Gulf of Aden (Lucazeau *et al.*, 2008), as an efficient hydrothermal cooling system such as those observed on fast-spreading ridges has not yet been established. (3) Considering a 'normal' intermediate- to fast-spreading ridge that is characterized by efficient melt extraction, formation of robust oceanic crust and a mean extent of melting of ~10% in the asthenosphere, a 10 km thick parcel of mantle rock would separate into 9 km of residual peridotite and 1 km of basaltic crust (Fig. 18). A seismic experiment would detect a clear discontinuity in seismic velocities resulting in a well-defined Moho. In constrast, if the 10% melt is not efficiently extracted but more or less uniformly distributed in the mantle parcel, the average density might still be sufficiently different from residual peridotite to drive exhumation, yet a Moho would be difficult to identify geophysically, and the melt would probably remain undetected by seismic investigations. Whereas a gradational increase of seismic velocities in areas of exposed mantle can be attributed to variable degrees of serpentinization in the upper 3–5 km (Minshull *et al.*, 1998), anomalously low seismic velocities beneath thinned continental crust (e.g. Van Avendonk *et al.*, 2006) might be explained by a 'lithospheric sponge' type of mantle.

CONCLUSIONS

Detailed investigations of spinel and plagioclase peridotites representing a former ocean–continent transition show

that a chemical and thermal boundary between subcontinental and infiltrated mantle is well defined, and is characterized by important changes in lithology and both major and trace element composition of the constituent minerals. The data from the Eastern Central Alps can be used to constrain the processes of syn-rift melt storage in present-day magma-poor rifted margins. The textures and chemistry of the Malenco–Platta–Totalp peridotites are similar to those of the peridotites of the Iberia–Newfoundland margin, and we can use the spatial relationships to infer the distribution of 'cold' subcontinental and 'hot' refertilized peridotites in ocean–continent transitions.

Geochemical models using a variety of major and trace elements demonstrate that the plagioclase peridotites are unlikely to be residual after a low degree of partial melting. Instead, the data are better fitted by refertilization of previously depleted peridotites. Quantitative estimates based on simple trace element models indicate that both batch and fractional melts percolated within the peridotites, from which clinopyroxene and plagioclase precipitated. Assuming a residue of fractional melting as the source rock, the models show that up to 12% of melt might be retained in the plagioclase peridotites. If this process can be generalized, it can explain a variety of geophysical observations from modern ocean–continent transitions, such as high heat flow, subsidence retardation of 'extensional allochthons' and poorly defined Moho reflections. The data from the Eastern Central Alps peridotites indicate that magma-poor rifted margins are not amagmatic, but that most syn-rift melts crystallized at depth before a robust melt extraction system was established.

ACKNOWLEDGEMENTS

This research was supported by the Swiss National Science Foundation (Grants 20-55284.98 and PP002-102809) and the French GDR/Action Marges. Constructive comments by Dante Canil, Veronique LeRoux, Elisabetta Rampone and Jean-Louis Bodinier helped to clarify several points and are highly appreciated.

REFERENCES

Bernoulli, D. & Jenkyns, H. C. (2009). Ancient oceans and continental margins of the Alpine–Mediterranean Tethys: deciphering clues from Mesozoic pelagic sediments and ophiolites. *Sedimentary Geology* **56**, 149–190.

Bernoulli, D., Manatschal, G., Desmurs, L. & Müntener, O. (2003). Where did Gustav Steinmann see the trinity? Back to the roots of an Alpine ophiolite concept. In: Dilek, Y. & Newcomb, S. (eds) *Ophiolite Concept and the Evolution of Geological Thought. Geological Society of America, Special Papers* **373**, 93–110.

Blackman, D. K., Cann, J. R., Janssen, B. & Smith, D. K. (1998). Origin of extensional core complexes: Evidence from the Mid-Atlantic ridge at Atlantis fracture zone. *Journal of Geophysical Research* **103**, 21315–21333.

Blundy, J. D. & Wood, B. J. (1991). Crystal-chemical controls on the partitioning of Sr and Ba between plagioclase feldspar, silicate melts, and hydrothermal solutions. *Geochimica et Cosmochimica Acta* **55**, 193–209.

Blundy, J. D., Falloon, T. J., Wood, B. J. & Dalton, J. A. (1995). Sodium partitioning between clinopyroxene and silicate melts. *Journal of Geophysical Research* **100**, 15501–15515.

Bodinier, J. L. & Godard, M. (2003). Orogenic, ophiolitic, and abyssal peridotites. In: Carlson, R. W. (ed.) *Treatise on Geochemistry, Vol. 2: Mantle and Core*. Amsterdam: Elsevier Science, pp. 103–170.

Bodinier, J. L., Garrido, C. J., Chanefo, I., Bruguier, O. & Gervilla, F. (2008). Origin of pyroxenite–peridotite veined mantle by refertilization reactions: evidence from the Ronda peridotite (Southern Spain). *Journal of Petrology* **49**, 999–1025.

Boillot, G., Recq, M., Winterer, E. L., Meyer, A. W., Applegate, J. *et al.* (1987). Tectonic denudation of the upper mantle along passive margins: a model based on drilling results (ODP Leg 103, western Galicia margin, Spain). *Tectonophysics* **132**, 335–342.

Bonatti, E., Brunelli, D., Fabretti, P., Ligi, M., Portaro, R. A. & Seyler, M. (2001). Steady-state creation of crust-free lithosphere at cold spots in mid-ocean ridges. *Geology* **29**, 979–982.

Boudier, F. (1978). Structure and petrology of the Lanzo peridotite massif (Piedmont Alps). *Geological Society of America Bulletin* **89**, 1574–1591.

Brey, G. P. & Köhler, T. (1990). Geothermobarometry in four-phase lherzolites II. New thermobarometers, and practical assessment of existing thermobarometers. *Journal of Petrology* **31**, 1353–1378.

Brey, G. P., Köhler, T. & Nickel, K. G. (1990). Geothermobarometry in four-phase lherzolites I. Experimental results from 10 to 60 kb. *Journal of Petrology* **31**, 1313–1352.

Canil, D. (2004). Mildly incompatible elements in peridotites and the origins of mantle lithosphere. *Lithos* **77**, 375–393.

Cannat, M. (1993). Emplacement of mantle rocks in the seafloor at mid-ocean ridges. *Journal of Geophysical Research* **98**, 4163–4172.

Cannat, M. (1996). How thick is the magmatic crust at slow spreading oceanic ridges? *Journal of Geophysical Research* **101**, 2847–2857.

Cannat, M. & Casey, J. F. (1995). An ultramafic lift at the Mid-Atlantic Ridge: successive stages of magmatism in serpentinized peridotites from the 15°N region. In: Vissers, R. L. M. & Nicolas, A. (eds) *Mantle and Lower Crust Exposed in Oceanic Ridges and in Ophiolites*. Dordrecht: Kluwer Academic, pp. 5–34.

Cannat, M., Chatin, F., Whitechurch, H. & Ceuleneer, G. (1997). Gabbroic rocks trapped in the upper mantle at the Mid-Atlantic Ridge. In: Karson, J. A., Cannat, M., Miller, D. J. & Elthon, D. (eds) *Proceedings of the Ocean Drilling Program, Scientific Results, 153*. College Station, TX: Ocean Drilling Program, pp. 243–264.

Caroll Webb, S. A. C. & Wood, B. J. (1986). Spinel–pyroxene–garnet relationships and their dependence on Cr/Al ratio. *Contributions to Mineralogy and Petrology* **92**, 471–480.

Chapman, D. S. (1986). Thermal gradients in the continental crust. In: Dawson, J. B., Carswell, D. A., Hall, J. & Wedepohl, K. H. (eds) *The Nature of the Lower Continental Crust. Geological Society, London, Special Publications* **24**, 63–70.

Chazot, G., Charpentier, S., Kornprobst, J., Vannucci, R. & Luais, B. (2005). Lithospheric mantle evolution during continental break-up: the West Iberia non-volcanic passive margin. *Journal of Petrology* **46**, 2569–2592.

Coleman, R. G. (1971). Plate tectonic emplacement of upper mantle peridotites along continental edges. *Journal of Geophysical Research* **76**, 1212–1222.

Coleman, R. G. & Irwin, W. P. (1974). Ophiolites and ancient continental margins. In: Burk, C. A. & Drake, C. L. (eds) *The Geology of Continental Margins*. New York: Springer, pp. 921–931.

Cornen, G., Beslier, M. O. & Girardeau, J. (1996). Petrologic characteristics of the ultramafic rocks from the ocean–continent transition in the Iberia abyssal plain. In: Whitmarsh, R. B., Sawyer, D. S., Klaus, A. & Masson, D. G. (eds) *Proceedings of the Ocean Drilling Program, Scientific Results, 149.* College Station, TX: Ocean Drilling Program, pp. 377–395.

Decandia, F. A. & Elter, P. (1972). La 'zona' ofiolitifera del Bracco nel settore compreso fra Levanto e la Val Graveglia (Appennino ligure). *Memorie della Società Geologica Italiana* **11**, 503–530.

Desmurs, L. (2001). Mantle evolution and magmatism in an evolving ocean–continent transition: The Platta nappe, eastern Switzerland. Zürich: ETH Zürich, 136 pp.

Desmurs, L., Manatschal, G. & Bernoulli, D. (2001). The Steinmann trinity revisited: exhumation and magmatism along an ocean–continent transition: the Platta nappe, eastern Switzerland. In: Wilson, R. C. L., Whitmarsh, R. B., Taylor, B. & Froitzheim, N. (eds) *Non-volcanic Rifting of Continental Margins: A Comparison of Evidence from Land and Sea. Geological Society, London, Special Publications* **187**, 235–266.

Desmurs, L., Müntener, O. & Manatschal, G. (2002). Onset of magmatic accretion within magma-poor passive margins: A case study from the Err–Platta ocean–continent transition, Eastern Switzerland. *Contributions to Mineralogy and Petrology* **144**, 365–382.

Dick, H. J. B. (1989). Abyssal peridotites, very slow spreading ridges and ocean ridge magmatism. In: Saunders, A. D. & Norry, M. J. (eds) *Magmatism in the Ocean Basins. Geological Society, London, Special Publications* **42**, 71–105.

Dick, H. J. B., Fisher, R. L. & Bryan, W. B. (1984). Mineralogic variability of the uppermost mantle along mid-ocean ridges. *Earth and Planetary Science Letters* **69**, 88–106.

Dick, H. J. B., Lin, J. & Schouten, H. (2003). A new class of mid-ocean ridges. *Nature* **426**, 405–412.

Dietrich, V. (1970). Die Stratigraphie der Platta-Decke. *Eclogae Geologicae Helvetiae* **63**, 631–671.

Dijkstra, A. H., Drury, M. R. & Vissers, R. L. M. (2001). Structural petrology of plagioclase peridotites in the West Othris Mountains (Greece): Melt impregnation in mantle lithosphere. *Journal of Petrology* **42**, 5–24.

Elthon, D. (1992). Chemical trends in abyssal peridotites: Refertilization of depleted suboceanic mantle. *Journal of Geophysical Research* **97**, 9015–9025.

Ernst, W. G. (1978). Petrochemical study of lherzolitic rocks from the Western Alps. *Journal of Petrology* **19**, 341–392.

Florineth, D. & Froitzheim, N. (1994). Transition from continental to oceanic basement in the Tasna nappe (Engadine window, Graubünden, Switzerland): evidence for Early Cretaceous opening of the Valais ocean. *Schweizerische Mineralogische und Petrographische Mitteilungen* **74**, 437–448.

Frisch, W., Ring, U., Dürr, S., Borchert, S. & Biehler, D. (1994). The Arosa zone and Platta nappe ophiolites (Eastern Swiss Alps): Geochemical characteristics and their meaning for the evolution of the Pennine ocean. *Jahrbuch der Geologischen Bundesanstalt Wien* **137**, 19–33.

Garrido, C. J., Bodinier, J. L. & Alard, O. (2000). Incompatible trace element partitioning and residence in anhydrous spinel peridotites and websterites from the Ronda orogenic peridotite. *Earth and Planetary Science Letters* **181**, 341–358.

Godard, M., Lagabrielle, Y., Alard, O. & Harvey, J. (2008). Geochemistry of the highly depleted peridotites drilled at ODP Sites 1272 and 1274 (Fifteen–Twenty Fracture Zone, Mid-Atlantic Ridge): Implications for mantle dynamics beneath a slow spreading ridge. *Earth and Planetary Science Letters* **267**, 410–425.

Goldstein, S. L., Soffer, G., Langmuir, C. H., Lehnert, K. A., Graham, D. W. & Michael, P. J. (2008). Origin of a 'southern hemisphere' geochemical signature in the Arctic upper mantle. *Nature* **453**, 89–93.

Günther, D., Frischknecht, R., Heinrich, C. A. & Kahlert, H. J. (1997). Capabilities of an Argon Fluoride 193 nm excimer laser for laser ablation inductively coupled plasma mass spectrometry microanalysis of geological materials. *Journal of Analytical Atomic Spectrometry* **12**, 939–944.

Hansmann, W., Müntener, O. & Hermann, J. (2001). U–Pb zircon geochronology of a tholeiitic intrusion and associated migmatites at a continental crust–mantle transition, Val Malenco, Italy. *Schweizerische Mineralogische und Petrographische Mitteilungen* **81**, 239–255.

Harvey, J., Gannoun, A., Burton, K. W., Rogers, N. W., Alard, O. & Parkinson, I. J. (2006). Ancient melt extraction from the oceanic upper mantle revealed by Re–Os isotopes in abyssal peridotites from the Mid-Atlantic ridge. *Earth and Planetary Science Letters* **244**, 606–621.

Hébert, R., Gueddari, K., Laflèche, M. R., Beslier, M. O. & Gardien, V. (2001). Petrology and geochemistry of exhumed peridotites and gabbros from non-volcanic margins: ODP Leg 173 West Iberia ocean–continent transition zone. In: Wilson, R. C. L., Whitmarsh, R. B., Taylor, B. & Froitzheim, N. (eds) *Non-volcanic Rifting of Continental Margins: A Comparison of Evidence from Land and Sea. Geological Society, London, Special Publications* **187**, 161–189.

Hellebrand, E. & Snow, J. E. (2003). Deep melting and sodic metasomatism underneath the highly oblique-spreading Lena Trough (Arctic Ocean). *Earth and Planetary Science Letters* **216**, 283–299.

Hellebrand, E., Snow, J. E., Dick, H. J. B. & Hofmann, A. W. (2001). Coupled major and trace elements as indicators of the extent of melting in mid-ocean-ridge peridotites. *Nature* **410**, 677–681.

Hellebrand, E., Snow, J. E., Hoppe, P. & Hofmann, A. W. (2002). Garnet-field melting and late-stage refertilisation in 'residual' abyssal peridotites from the Central Indian Ridge. *Journal of Petrology* **43**, 2305–2338.

Hellebrand, E., Snow, J. E., Mostefaoui, S. & Hoppe, P. (2005). Trace element distribution between orthopyroxene and clinopyroxene in peridotites from the Gakkel Ridge: a SIMS and NanoSIMS study. *Contributions to Mineralogy and Petrology* **150**, 486–504.

Hermann, J., Müntener, O., Trommsdorff, V., Hansmann, W. & Piccardo, G. P. (1997). Fossil crust-to-mantle transition, Val Malenco (Italian Alps). *Journal of Geophysical Research* **102**, 20123–20132.

Hirschmann, M. M. (2000). Mantle solidus: Experimental constraints and the effects of peridotite composition. *Geochemistry, Geophysics, Geosystems* **1**, doi:2000GC000070.

Ildefonse, B., Blackman, D. K., John, B. E., Ohara, Y., Miller, D. J., MacLeod, C. J. & Expedition 304/305 Scientists, (2007). Oceanic core complexes and crustal accretion at slow-spreading ridges. Geology 35, 623–626.

Ionov, D. A., Savoyant, L. & Dupuy, C. (1992). Application of the ICP-MS technique to trace-element analysis of peridotites and their minerals. *Geostandards Newsletter* **16**, 311–315.

Jackson, S. (2008). LAMTRACE data reduction software for LA-ICP-MS. In: Sylvester, P. (ed.) *Laser Ablation ICP-MS in the Earth Sciences: Current Practices and Outstanding Issues. Mineralogical Association of Canada, Short Course Series* **40**, 305–307.

Johnson, K. T. M. (1998). Experimental determination of partition coefficients for rare earth and high-field-strength elements between clinopyroxene, garnet and basaltic melt at high pressures. *Contributions to Mineralogy and Petrology* **133**, 60–68.

Johnson, K. T. M., Dick, H. J. B. & Shimizu, N. (1990). Melting in the oceanic upper mantle: An ion microprobe study of diopsides in abyssal peridotites. *Journal of Geophysical Research* **95**, 2661–2678.

Kaczmarek, M.-A. & Müntener, O. (2008). Juxtaposition of melt impregnation and high-temperature shear zones in the upper mantle; field and petrological constraints from the Lanzo Peridotite (Northern Italy). *Journal of Petrology* **49**, 2187–2220.

Kaczmarek, M.-A. & Müntener, O. (2009). The variability of peridotite composition across a mantle shear zone (Lanzo massif, Italy): interplay of melt focusing and deformation. *Contributions to Mineralogy and Petrology* (accepted).

Kaczmarek, M.-A., Müntener, O. & Rubatto, D. (2008). Trace element chemistry and U–Pb dating of zircons in oceanic gabbros and their relationship with whole rock composition (Lanzo, Italian Alps). *Contributions to Mineralogy and Petrology* **155**, 295–312.

Kinzler, R. (1997). Melting of mantle peridotite at pressures approaching the spinel to garnet transition: application to mid-ocean-ridge basalt petrogenesis. *Journal of Geophysical Research* **102**, 853–874.

Kornprobst, J. & Tabit, A. (1988). Plagioclase bearing ultramafic tectonites from the Galicia margin (Leg 103 Site 637): comparison of their origin and evolution with low-pressure ultramafic bodies in Western Europe. In: Boillot, G., Winterer, E.L. *et al.* (eds) *Proceedings of the Ocean Drilling Program, Scientific Results, 103.* College Station, TX: Ocean Drilling Program pp. 252–268.

Langmuir, C. H., Klein, E. M. & Plank, T. (1993). Petrological systematics of mid-ocean ridge basalts: constraints on melt generation beneath ocean ridges. In: Phipps Morgan, J., Blackman, D. K. & Sinton, J. M. (eds) *Mantle Flow and Melt Generation at Mid-Ocean Ridges. Geophysical Monograph, American Geophysical Union* **71**, 183–280.

Lemoine, M., Tricart, P. & Boillot, G. (1987). Ultramafic and gabbroic ocean floor of the Ligurian Tethys (Alps, Corsica, Apennines). In search of a genetic model. *Geology* **15**, 622–625.

Le Roux, V., Bodinier, J. L., Tommasi, A., Alard, O., Dautria, J. M., Vauchez, A. & Riches, A. J. V. (2007). The Lherz spinel lherzolite: Refertilized rather than pristine mantle. *Earth and Planetary Science Letters* **259**, 599–612.

Lucazeau, F., Leroy, S., Bonneville, A., Goutorbe, B., Rolandone, F., D'Acremont, E., Watremez, L., Düsünur, D., Tuchais, P., Huchon, P., Bellahsen, N. & Al-Toubi, K. (2008). Persistent thermal activity at the Eastern Gulf of Aden after continental break-up. *Nature Geosciences* **1**, 854–858.

Manatschal, G. & Müntener, O. (2009). A type sequence across an ancient magma-poor ocean–continent transition: the example of the western Alpine Tethys ophiolites. *Tectonophysics* **473**, 4–19.

Manatschal, G. & Nievergelt, P. (1997). A continent–ocean transition recorded in the Err and Platta nappes (eastern Switzerland). *Eclogae Geologicae Helvetiae* **90**, 3–27.

Manatschal, G., Froitzheim, N., Turrin, B. & Rubenach, M. (2001). The role of detachment faulting in the formation of an ocean–continent transition: insights from the Iberia abyssal plain. In: Wilson, R. C. L., Whitmarsh, R. B., Taylor, B. & Froitzheim, N. (eds) *Non-volcanic Rifting of Continental Margins: A Comparison of Evidence from Land and Sea. Geological Society, London, Special Publications* **187**, 405–428.

Manatschal, G., Müntener, O., Lavier, L. L., Minshull, T. A. & Péron-Pinvidic, G. (2007). Observations from the Alpine Tethys and Iberia–Newfoundland margins pertinent to the interpretation of continental breakup. In: Karner, G. D., Manatschal, G. & Pinheiro, L. M. (eds) *Imaging, Mapping and Modelling Continental Lithosphere Extension and Breakup. Geological Society, London, Special Publications* **282**, 291–324.

McDonough, W. F. & Sun, S.-S. (1995). The composition of the Earth. *Chemical Geology* **120**, 223–253.

McKenzie, D. (1978). Some remarks on the development of sedimentary basins. *Earth and Planetary Science Letters* **40**, 25–32.

McKenzie, D. & O'Nions, R. K. (1991). Partial melt distribution from inversion of rare earth element concentrations. *Journal of Petrology* **32**, 1021–1091.

Michael, P. J., Langmuir, C. H., Dick, H. J. B., Snow, J. E., Goldstein, S. L., Graham, D. W., Lehnert, K., Kurras, G., Jokat, W., Muhe, R. & Edmonds, H. N. (2003). Magmatic and amagmatic seafloor generation at the ultraslow-spreading Gakkel Ridge, Arctic Ocean. *Nature* **423**, 956–961.

Minshull, T. A., Muller, M. R., Robinson, C. J., White, R. S. & Bickle, M. J. (1998). Is the oceanic Moho a serpentinization front?. In: Mills, R. A. & Harrison, K. (eds) *Modern Ocean Floor Processes and the Geological Record. Geological Society, London, Special Publications* **148**, 71–80.

Montanini, A., Tribuzio, R. & Anczkiewicz, R. (2006). Exhumation history of a garnet pyroxenite-bearing mantle section from a continent–ocean transition (Northern Apennine ophiolites, Italy). *Journal of Petrology* **47**, 1943–1971.

Müntener, O. (1997). The Malenco peridotites (Alps): Petrology and geochemisty of subcontinental mantle and Jurassic exhumation during rifting. ETH Zürich, 205 pp.

Müntener, O. & Hermann, J. (1996). The Val Malenco lower crust–upper mantle complex and its field relations (Italian Alps). *Schweizerische Mineralogische und Petrographische Mitteilungen* **76**, 475–500.

Müntener, O. & Hermann, J. (2001). The role of lower crust and continental upper mantle during formation of non-volcanic passive margins: Evidence from the Alps. In: Wilson, R. C. L., Whitmarsh, R. B., Taylor, B. & Froitzheim, N. (eds) *Non-volcanic Rifting of Continental Margins: A Comparison of Evidence from Land and Sea. Geological Society, London, Special Publications* **187**, 267–288.

Müntener, O. & Manatschal, G. (2006). High degrees of melting recorded by spinel harzburgites of the Newfoundland margin: The role of inheritance and consequences for the evolution of the southern North Atlantic. *Earth and Planetary Science Letters* **252**, 437–452.

Müntener, O. & Piccardo, G. B. (2003). Melt migration in ophiolitic peridotites: the message from Alpine–Apennine peridotites and implications for embryonic ocean basins. In: Dilek, Y. & Robinson, P. T. (eds) *Ophiolites in Earth History. Geological Society, London, Special Publications* **218**, 69–89.

Müntener, O., Hermann, J. & Trommsdorff, V. (2000). Cooling history and exhumation of lower crustal granulites and upper mantle (Malenco, Eastern Central Alps). *Journal of Petrology* **41**, 175–200.

Müntener, O., Pettke, T., Desmurs, L., Meier, M. & Schaltegger, U. (2004). Refertilization of mantle peridotite in embryonic ocean basins: Trace element and Nd-isotopic evidence and implications for crust–mantle relationships. *Earth and Planetary Science Letters* **221**, 293–308.

Nisbet, E. G., Dietrich, V. J. & Esenwein, A. (1976). Routine trace element determination in silicate minerals and rocks by X-ray fluorescence. *Fortschritte der Mineralogie* **57**, 264–279.

Paglia, C. (1996). Ricerche strutturali e petrografiche lungo il margine meridionale del corpo ultramafico del Malenco. Parte I: Zona Cassandra. Unpublished Diploma thesis ETH Zürich.

Peretti, A. & Köppel, V. (1986). Geochemical and lead isotope evidence for a mid-ocean ridge type mineralization within a polymetamorphic ophiolite complex (Mte del Forno, North Italy, Switzerland). *Earth and Planetary Science Letters* **80**, 252–264.

Péron-Pinvidic, G. & Manatschal, G. (2009). The final rifting evolution at deep magma-poor passive margins from Iberia–Newfoundland: a new point of view. *International Journal of Earth Sciences* **98**, 1581–1597.

Peters, T. (1963). Mineralogie und Petrographie des Totalpserpentins bei Davos. *Schweizerische Mineralogische und Petrographische Mitteilungen* **43**, 527–686.

Peters, T. (1968). Distribution of Mg, Fe, Al, Ca and Na in coexisting olivine, orthopyroxene and clinopyroxene in the Totalp serpentinite (Davos, Switzerland) and in the Alpine metamorphosed Malenco Serpentinite (N. Italy). *Contributions to Mineralogy and Petrology* **18**, 65–75.

Peters, T. & Dietrich, V. J. (2008). Blatt 1256 Bivio. Geologischer Atlas der Schweiz 1:25 000, Erläuterungen 124. Wabern: Bundesamt für Landestopographie swisstopo.

Pettke, T., Halter, W. E., Webster, J. D., Aigner-Torres, M. & Heinrich, C. A. (2004). Accurate quantification of melt inclusion chemistry by LA-ICPMS: a comparison with EMP and SIMS and advantages and possible limitations of these methods. *Lithos* **78**, 333–361.

Piccardo, G. B., Rampone, E. & Vannucci, R. (1990). Upper mantle evolution during continental rifting and ocean formation: evidence from peridotite bodies of the Western Alpine–Northern Apennine system. *Mémoires de la Société Géologique de la France* **156**, 323–333.

Piccardo, G. B., Zanetti, A. & Müntener, O. (2007). Melt/peridotite interaction in the Lanzo South peridotite: field, textural and geochemical evidence. *Lithos* **94**, 181–209.

Pognante, U., Rösli, U. & Toscani, L. (1985). Petrology of ultramafic and mafic rocks from the Lanzo peridotite body (Western Alps). *Lithos* **18**, 201–214.

Pouchou, J. L. & Pichoir, F. (1984). Un nouveau modèle de calcul pour la microanalyse quantitative par spectrométrie de rayons X. I: Application à analyse d'échantillons homogènes. *Recherche Aerospatiale* **3**, 167–192.

Puschnig, A. R. (2000). The oceanic Forno unit (Rhetic Alps): geochemistry and paleogeographic setting. *Eclogae Geologicae Helvetiae* **93**, 103–124.

Rampone, E. & Piccardo, G. B. (2000). The ophiolite–oceanic lithosphere analogue: new insights from the Northern Apennines (Italy). In: Dilek, Y., Moores, E. M., Elthon, D. & Nicolas, A. (eds) *Ophiolites and Oceanic Crust: New Insights from Field Studies and the Ocean Drilling Program. Geological Society of America, Special Papers* **349**, 21–34.

Rampone, E., Piccardo, G. B., Vannucci, R., Bottazzi, P. & Ottolini, L. (1993). Subsolidus reactions monitored by trace element partitioning: the spinel- to plagioclase-facies transition in mantle peridotites. *Contributions to Mineralogy and Petrology* **115**, 1–17.

Rampone, E., Hofmann, A. W., Piccardo, G. B., Vannucci, R., Bottazzi, P. & Ottolini, L. (1995). Petrology, mineral and isotope geochemistry of the External Liguride peridotites (Northern Apennines, Italy). *Journal of Petrology* **36**, 81–105.

Rampone, E., Hofmann, A. W., Piccardo, G. B., Vannucci, R., Bottazzi, P. & Ottolini, L. (1996). Trace element and isotope geochemistry of depleted peridotites from an N-MORB type ophiolite (Internal Liguride, N Italy). *Contributions to Mineralogy and Petrology* **123**, 61–76.

Rampone, E., Piccardo, G. B., Vannucci, R. & Bottazzi, P. (1997). Chemistry and origin of trapped melts in ophiolitic peridotites. *Geochimica et Cosmochimica Acta* **61**, 4557–4569.

Rampone, E., Hofmann, A. W. & Raczek, I. (1998). Isotopic contrasts within the Internal Liguride ophiolite (N. Italy): the lack of a genetic mantle–crust link. *Earth and Planetary Science Letters* **163**, 175–189.

Reber, D. (1995). Strukturelle und petrographische Untersuchungen im oberen Val Malenco (Val Ventina, Provinz Sondrio, N-Italien). Teil 3. Unpublished Diploma thesis University of Zürich.

Salters, V. J. M., Longhi, J. E. & Bizimis, M. (2002). Near mantle solidus trace element partitioning at pressures up to 3·4 GPa. *Geochemistry, Geophysics, Geosystems* **3**, doi:2001GC000148.

Schaltegger, U., Desmurs, L., Manatschal, G., Müntener, O., Meier, M., Frank, M. & Bernoulli, D. (2002). The transition from rifting to seafloor spreading within a magma-poor rifted margin: field and isotopic constraints. *Terra Nova* **14**, 156–162.

Seitz, H. M., Altherr, R. & Ludwig, T. (1999). Partitioning of transition elements between orthopyroxene and clinopyroxene in peridotitic and websteritic xenoliths: New empirical geothermometers. *Geochimica et Cosmochimica Acta* **63**, 3967–3982.

Seyler, M., Lorand, J.-P., Dick, H. J. B. & Drouin, M. (2007). Pervasive melt percolation reactions in ultra-depleted refractory harzburgites at the Mid-Atlantic Ridge, 15°20'N: ODP Hole 1274A. *Contributions to Mineralogy and Petrology* **153**, 303–319.

Simon, N. S. C. & Podladchikov, Y. Y. (2008). The effect of mantle composition on density in the extending lithosphere. *Earth and Planetary Science Letters* **272**, 148–157.

Suhr, G., Seck, H. A., Shimizu, N., Günther, D. & Jenner, G. (1998). Infiltration of refractory melts into the lowermost oceanic crust: evidence from dunite- and gabbro-hosted clinopyroxenes in the Bay of Islands ophiolite. *Contributions to Mineralogy and Petrology* **131**, 136–154.

Sun, S.-S. & McDonough, W. F. (1989). Chemical and isotopic systematics of oceanic basalts: Implications for mantle composition and processes. In: Saunders, A. D. & Norry, M. J. (eds) *Magmatism in the Ocean Basins. Geological Society, London, Special Publications* **42**, 313–345.

Trommsdorff, V., Piccardo, G. B. & Montrasio, A. (1993). From magmatism, through metamorphism to sea-floor emplacement of subcontinental Adria lithosphere during pre-Alpine rifting (Malenco, Italy). *Schweizerische Mineralogische und Petrographische Mitteilungen* **73**, 191–203.

Tucholke, B. E. & Sibuet, J.-C. (2007). Leg 210 synthesis: tectonic, magmatic, and sedimentary evolution of the Newfoundland–Iberia Rift. In: Tucholke, B. E. & Sibuet, J.-C. (eds) *Proceedings of the Ocean Drilling Program, Scientific Results, 210.* College Station, TX: Ocean Drilling Program, pp. 1–56.

Tucholke, B. E., Lin, J. & Kleinrock, M. C. (1998). Megamullions and mullion structure defining oceanic metamorphic core complexes on the Mid-Atlantic ridge. *Journal of Geophysical Research* **103**, 9857–9866.

Ulmer, P. & Trommsdorff, V. (1999). Phase relations of hydrous mantle subducting to 300 km. In: Fei, Y., Bertka, C. M. & Mysen, B. O. (eds) *Mantle Petrology: Field Observations and High Pressure Experimentation: A Tribute to Francis R. (Joe) Boyd. Geochemical Society, Special Publication* **6**, 259–281.

Ulrich, T. & Borsien, G. R. (1996). Chemische Untersuchungen am Fedozer Gabbro und ein Vergleich mit dem Forno Metabasalt (Val Malenco, Norditalien). *Schweizerische Mineralogische und Petrographische Mitteilungen* **76**, 521–535.

van Acken, D., Becker, H. & Walker, R. J. (2008). Refertilization of Jurassic oceanic peridotites from the Tethys Ocean—Implications for the Re–Os systematics of the upper mantle. *Earth and Planetary Science Letters* **268**, 171–181.

Van Avendonk, H. J. A., Holbrook, W. S., Nunes, G. T., Shillington, D. J., Tucholke, B., Louden, K. E., Larsen, H. C. & Hopper, J. R. (2006). Seismic velocity structure of the rifted margin of the eastern Grand Banks of Newfoundland, Canada. *Journal of Geophysical Research* **111**, B11404, doi:11410.11029/12005JB004156.

Vannucci, R., Rampone, E., Piccardo, G. B., Ottolini, L. & Bottazzi, P. (1993*a*). Ophiolitic magmatism in the Ligurian Tethys:

An ion microprobe study of basaltic clinopyroxenes. *Contributions to Mineralogy and Petrology* **115**, 123–137.

Vannucci, R., Shimizu, N., Piccardo, G. B., Ottolini, L. & Bottazzi, P. (1993*b*). Distribution of trace elements during breakdown of mantle garnet: an example from Zabargad. *Contributions to Mineralogy and Petrology* **113**, 437–449.

Vannucci, R., Piccardo, G. B., Rivalenti, G., Zanetti, A., Rampone, E., Ottolini, L., Oberti, R., Mazzucchelli, M. & Bottazzi, P. (1995). Origin of LREE-depleted amphiboles in the subcontinental mantle. *Geochimica et Cosmochimica Acta* **59**, 1763–1771.

Villa, I. M., Hermann, J., Müntener, O. & Trommsdorff, V. (2000). ^{39}Ar–^{40}Ar dating of multiply zoned amphibole generations (Malenco, Italian Alps). *Contributions to Mineralogy and Petrology* **140**, 363–381.

Walter, M. J. (1998). Melting of garnet peridotite and the origin of komatiite and the depleted lithosphere. *Journal of Petrology* **39**, 29–60.

Whitmarsh, R. B., Manatschal, G. & Minshull, T. A. (2001). Evolution of magma-poor continental margins from rifting to sea-floor spreading. *Nature* **413**, 150–154.

Witt-Eickschen, G. & O'Neill, H. S. C. (2005). The effect of temperature on the equilibrium distribution of trace elements between clinopyroxene, orthopyroxene, olivine and spinel in upper mantle peridotite. *Chemical Geology* **221**, 65–101.

Witt-Eickschen, G. & Seck, H. A. (1991). Solubility of Ca and Al in orthopyroxene from spinel peridotite: an improved version of an empirical geothermometer. *Contributions to Mineralogy and Petrology* **106**, 431–439.

Workman, R. K. & Hart, S. R. (2005). Major and trace element composition of the depleted MORB mantle (DMM). *Earth and Planetary Science Letters* **231**, 53–72.